

# Iterative Reconstruction Methods for Inverse Problems in Tomography with Hybrid Data

**Sherina, Ekaterina**

*Publication date:*
2018

*Document Version*
Publisher's PDF, also known as Version of record

# Iterative Reconstruction Methods for Inverse Problems in Tomography with Hybrid Data

Ekaterina Sherina


Kongens Lyngby 2017

Technical University of Denmark
Department of Applied Mathematics and Computer Science
Richard Petersens Plads, building 324,
2800 Kongens Lyngby, Denmark
Phone +45 4525 3031
compute@compute.dtu.dk
www.compute.dtu.dk

PHD-2018-468
ISSN: 0909-3192

# Preface

This thesis was prepared in partial fulfilment of the requirements for acquiring the PhD degree at the Technical University of Denmark. The main part of the research work for this thesis was done between 1 January 2015 and 31 December 2017 in the Section for Scientific Computing at the Department of Applied Mathematics and Computer Science, Technical University of Denmark, under the supervision of Associate Professor Kim Knudsen. Furthermore, another part of the research work was done during an external stay from 1 October 2016 to 31 January 2017 at the Computational Science Center, University of Vienna, under the supervision of Professor Otmar Scherzer.

The aim of this thesis is to present and document my work on parameter identification in two nonlinear inverse problems emerging in coupled physics imaging for Electrical Impedance Tomography with Hybrid Data and Quantitative Elastography, and consists of an introductory part followed by mathematical preliminaries and two main parts based on the scientific publications:

(A) S. Hubmer, K. Knudsen, C. Li and E. Sherina. Limited Angle Electrical Impedance Tomography with Power Density Data. Submitted manuscript (2017). Available from: https://arxiv.org/abs/1712.08009

(B) S. Hubmer, E. Sherina, A. Neubauer and O. Scherzer. Lamé Parameter Estimation from Static Displacement Field Measurements in the Framework of Nonlinear Inverse Problems. Submitted manuscript (2017). Available from: https://arxiv.org/abs/1710.10446

which are attached to this thesis after a conclusion section and appendices.

## Acknowledgements

First and foremost, I would like to thank my supervisor Associate Professor Kim Knudsen for offering me a chance to work in an interesting research field and be a part of the Hybrid Data project, for his support during my PhD and always positive attitude in dealing with any scientific questions.

During four months starting from October 2016, I was on an external research stay in Austria, visiting Professor Otmar Scherzer at the University of Vienna. I would like to thank him for offering me an interesting problem to solve and a chance to collaborate on an application of theoretical and medical significance. My thanks also go to my Austrian collaborators: Simon Hubmer, Julian Schmidt and Professor Andreas Neubauer.

Moreover, I would like to thank all members of the Hybrid Data and HD-Tomo research groups in the section for Scientific Computing at the Technical University of Vienna and the research group of the Computational Science Center at the University of Vienna for interesting discussions and a positive working environment.

Also, I would like to express my deep gratitude to my family, and my Austrian and Danish friends.

Finally, I would like to acknowledge the Otto Mønsted Foundation for partly funding my external research stay and a trip to one conference. Furthermore, I would like to acknowledge the Danish Council for Independent Research | Natural Sciences, grant no. 4002-00123 of the project 'Improved Impedance Tomography with Hybrid Data', for funding my PhD.

Kongens Lyngby
December 31, 2017

Ekaterina Sherina

# Summary (English)

This thesis provides a theoretical and numerical investigation of two important problems in the field of tomography based on *hybrid data* from *coupled physics* phenomena. The first problem is related to *Acousto-Electrical Tomography*, while the second problem deals with *Quantitative Elastography*. The goal of these modalities is to *quantify physical parameters* of materials or tissues inside an object from given *interior data*, which is measured everywhere inside the object. The advantage of these modalities is that large variations in physical parameters can be resolved and therefore, they have important applications in both medical and industrial imaging.

Mathematically, we face a *nonlinear Inverse Problem* of *parameter identification* type in both modalities. The applied physical phenomena are typically chosen in such a way that they interact with and complement each other, and most often they are described by models based on coupled partial differential equations. In contrast to common methods, e.g., Electrical Impedance Tomography, where the reconstruction is solely based on boundary measurements, methods based on coupled phenomena lead to *internal measurements*. Availability of this so-called *hybrid data* is precisely the reason why reconstructions with a high contrast and a high resolution can be expected.

The main contributions of this thesis consist in formulating the underlying mathematical problems with interior data as nonlinear operator equations, theoretically analysing them within the framework of nonlinear Inverse Problems and designing computational methods for identifying the unknown parameters. Furthermore, the theoretical investigations are supported by a number of numerical examples from both simulated and experimental data. Iterative regularization methods based on Landweber iteration and the Levenberg-Marquardt method are employed for solving the problems.

The first problem considered in this thesis is a problem of *conductivity estimation*

from interior measurements of the *power density*, known as Acousto-Electrical Tomography. A special case of limited angle tomography is studied for this problem, where only a part of the boundary is accessible to electrostatic measurements. Numerical examples support the intuition that stably reconstructing the conductivity becomes difficult far away from the accessible part of the measurement boundary. This is also supported by a quantitative numerical study of the ill-posedness of the problem in dependence on the completeness of the data. The second problem deals with Quantitative Elastography, where *Lamé parameters* are estimated from full internal *static displacement field* measurements obtained using both Photo-Acoustic Tomography and Optical Coherence Tomography. The developed computational method is successfully applied to both numerically simulated and experimental data.

# Summary (Danish)

Denne afhandling giver en teoretisk og numerisk undersøgelse af to vigtige problemstillinger inden for tomografi baseret på hybride data fra koblede fysiske fænomener. Det ene problem relaterer til Akustisk-Elektrisk tomografi, mens det andet omhandler kvantitativ elastografi. Målet med disse modaliteter er at kvantificere fysiske parametre i et område fra data, som er målt i samme område. Fordelen ved denne tilgang er, at store variationer i de fysiske parametre kan håndteres, og metoden har derfor vigtige anvendelser i både medicinsk og industriel billeddannelse.

Matematisk set står man i begge modaliteter med et ikke-lineært inverst problem for parameteridentifikationen. De anvendte fysiske fænomener er typisk valgt sådan, at de vekselvirker og komplementerer hinanden, og de beskrives oftest ved brug af modeller af koblede partielle differentielligninger. I modsætning til almindelige metoder indenfor fx elektrisk impedanstomografi, hvor rekonstruktion baseres udelukkende på randmålinger, så leder de koblede fænomener til indre målinger. Tilgængeligheden af disse såkaldte hybride data er netop årsagen til, at rekonstruktioner med høj kontrast og høj opløsning kan forventes.

Denne afhandlings væsentligste videnskabelige bidrag er formuleringen af de nævnte problemer som ligninger, som er givet ved ikke-lineære funktionaler, den teoretiske analyse af ligningerne indenfor rammerne af ikke-lineære inverse problemer, og udviklingen og implementationen af iterative algoritmer til beregning af ligningernes løsning. Algoritmerne, som er variationer af Landweber og Levenberg-Marquardt iteration, testes på både simulerede og eksperimentelle data.

I det første problem er der tale om rekonstruktion af den elektriske ledningsevne i et område via indre målinger af energitætheden. Dette problem er kendt som Akustisk-Elektrisk tomografi. Særligt undersøges et problem, hvor kun dele af randen er tilgængeligt for de elektrostatiske målinger. Numeriske un-

dersøgelser understøtter intuitionen, at fjernt fra den tilgængelige rand er stabil rekonstruktion særdeles vanskeligt. Dette underbygges endvidere med kvantitative, numeriske aspekter baseret på en linearisering af det ikke-lineære problem. Det andet problem omhandler kvantitativ elastografi, hvor de såkaldte Lamé-parametre estimeres ud fra kendskab til det interne statiske forskydningsfelt målt fx via foto-akustisk tomografi eller optisk-kohærens tomografi.

# Contents

# Chapter 1

# Introduction

## 1.1 Motivation

*Tomography* is an important field in imaging science occurring in various biomedical and industrial applications. The term 'tomos' means 'slice' or 'cut' in Greek, while the suffix 'graphia' stands for 'writing' or 'recording'. Tomography is concerned with producing images of the internal structure of an object without destroying the object itself. The information obtained by means of tomography has greatly advanced diagnostic medicine and non-destructive testing of materials over the last century. Although various tomographic techniques employ different scanning agents, the underlying mathematics is rather similar and can be expressed in the framework of Inverse Problems discussed in Chapter 2.

In order to learn about the internal structure of an object, it is essential for tomographic images to have both a high contrast and a high resolution. Unfortunately, this is not the case in many classical tomographic methods. *Hybrid* or *coupled physics imaging* is a recent trend in scientific and industrial mathematics and emerged as an attempt of solving conventional tomographic problems by relying on more than one imaging modality [AS12, Amm08, Bal13b, Kuc12, WS15, WS12]. These problems are called hybrid, because frequently the excitations and measurements belong to different modalities. Typically, the coupled technique plays a complementary role and compensates the downside of the main modality, which is generally known for being ill-posed and nonlinear. In many of the proposed techniques the interest lies in *quantifying* various physical parameters. The advantage of combining different physics in one problem usually consists in a significant improvement of the parameter reconstructions

exhibiting both a high contrast and a high resolution, which is not the case for the original modality. Frequently, this is due to the fact that the imaging problems of coupled physics are much better posed than the conventional problems, because in many of them helpful *hybrid data*, which is often given by *interior data*, can be obtained from the coupled technique. However, these problems require establishing new mathematical models, which can describe the underlying coupled physics phenomena. Furthermore, there are many open mathematical questions regarding existence, uniqueness and stability of coupled physics imaging problems. Finally, they require developing novel reconstruction algorithms for solving them.

## 1.2 Problem Descriptions

In this thesis, we study two important problems in the field of tomography based on hybrid data from coupled physics phenomena. The first problem is an inverse problem of conductivity estimation from interior measurements of the power density arising, for example, in coupled physics modalities such as Acousto-Electrical or Impedance-Acoustic Tomography. The forward model is given by

$$\begin{aligned} \operatorname{div}(\sigma \nabla u_i) &= 0\,, \qquad \text{in } \Omega\,, \\ (\sigma \nabla u_i) \cdot \vec{n}|_{\partial\Omega} &= g_i\,. \end{aligned} \tag{1.1}$$

The problem is to reconstruct the conductivity $\sigma$ given different boundary currents $g_i$ and the resulting interior power density measurements, defined by

$$E_i(\sigma) := \sigma \left|\nabla u_i(\sigma)\right|^2\,. \tag{1.2}$$

Hereby, we especially focus on the case when the boundary $\partial\Omega$ is only partly available for measurements, i.e., $g_i = 0$ on $\Gamma_0 \subset \partial\Omega$ and $g_i \neq 0$ on the remaining part $\Gamma_1 = \partial\Omega \setminus \Gamma_0$ almost everywhere. Additionally, the goal is to quantify the ill-posedness of this problem depending on the accessible area $\Gamma_1$.

For the second problem, we focus on Lamé parameter estimation from full static displacement field measurements emerging in Quantitative Elastography. The forward model is given by

$$\begin{aligned} -\operatorname{div}\left(\lambda\ \operatorname{div}(u)\, I + \mu\ \left(\nabla u + \nabla u^T\right)\right) &= f\,, \qquad \text{in } \Omega\,, \\ u\,|_{\Gamma_D} &= g_D\,, \\ \left(\lambda\ \operatorname{div}(u)\, I + \mu\ \left(\nabla u + \nabla u^T\right)\right) \vec{n}\,|_{\Gamma_T} &= g_T\,, \end{aligned} \tag{1.3}$$

where $\partial\Omega = \overline{\Gamma_T \cup \Gamma_D}$. The problem is to reconstruct the Lamé parameters $(\lambda, \mu)$ given $g_D$, $g_T$, and full interior measurements of the displacement field $u$.

## 1.3 Summary of Main Results

In this thesis we focus on deriving the necessary theoretical results and designing suitable computational methods for the solution of the two inverse problems mentioned above in the framework of nonlinear Inverse Problems. Both problems are treated in an infinite dimensional setting. After discussing solvability of the model PDEs and regularity of their solutions, we formulate the problems as nonlinear operator equations and derive the Fréchet derivatives and their adjoints of the respective operators, necessary for applying most of the available methods for solving nonlinear inverse problems. In our case, we employ iterative regularization methods based on Landwerber iteration and the Levenberg-Marquardt method. For the first problem, we present reconstructions for both full and limited angle cases from simulated measurements of the power densities, see for example Figures 3.3 and 3.6, respectively. We study how the limited angle case affects the solution and the identifiability of the conductivity and numerically analyse the ill-posedness of the problem using the singular value decomposition (SVD) of the Fréchet derivative of the underlying operator. The effect can be seen in the values of the condition numbers, Table 3.8, and the plot of the singular values, Figure 3.7. The transfer matrix becomes more an more ill-conditioned and the decay of the corresponding singular values becomes faster with decreasing available boundary and number of measurements. For the second problem, we prove a tangential cone condition (Theorem 4.3.3, Corollary 4.3.4 in Chapter 4 and Theorem 3.7 in Paper B) for compactly supported elasticity parameters and present numerical examples from both simulated and experimental data, see for example Figures 4.8 and 4.10, respectively.

## 1.4 Review of Relevant Literature

Many typical hybrid imaging problems evolved from different physical backgrounds such as magnetic resonance, ultrasound, elastography, microwaves, electrical impedance, etc. In general, according to [Kuc12], coupled physics imaging problems may roughly be classified in two groups by the interaction level between the coupled techniques. In the first group, modalities with no visible physical effect on each other are included, i.e., when combining two modalities, independent measurement data can be collected from both of them and then used for reconstructing the desired physical parameters. Providing this additional information in the problem usually ensures a much higher quality of the reconstructions compared to a single modality. It should be mentioned that this type of coupled physics problems do not require introducing new physical

models, but rather demand new reconstruction algorithms and data processing. Other authors refer to this class of modalities as *passive* coupled physics problems [WS12].

One of such coupled physics problems, as well as the first coupled physics problem to be considered in the literature, is a problem of conductivity imaging in Electrical Impedance Tomography (EIT) equipped with internal measurements of the current density, which was obtained using Magnetic Resonance Imaging (MRI) [AS12, WS12], and which gave rise to a technique called Magnetic Resonance Electrical Impedance Tomography (MREIT). Afterwards, such modalities as Current Density Impedance Imaging (CDII), Magnetic Resonance Electrical Property Tomography (MREPT), and Impediography were proposed [AS12, Amm08, Bal13b, Kuc12, WS12]. The injected electric currents generate an additional magnetic field inside the body which is measurable by MRI. From this, measurements of the current density are obtained which are then used for reconstructing the conductivity.

Another example of passive coupled physics problems originates from elastography, which is interested in recovering biomechanical properties of tissues. Combining elastography with ultrasound from Photoacoustic Tomography (PAT), light waves from Optical Coherence Tomography (OCT), or magnetic resonance from MRI made it possible to measure the internal displacement field. This approach developed into modalities called PAT Elastography, OCT Elastography and MR Elastography, respectively [WS15, MOD$^+$01].

In contrast, the second group covers coupled physics problems where two modalities are deeply interacting in such a way that a physical phenomenon underlying one modality typically triggers or modulates another physical phenomenon detectable by the other technique [Kuc12]. Those modalities are also known in the literature as *active* coupled physics problems [WS12]. Similarly to passive techniques, the acquired internal measurements are expected to improve the reconstruction quality.

Using acoustic detection in EIT was a starting point for developing Acousto-Electrical Tomography (AET) and Impedance-Acoustic Tomography (IAT) [ZW04, AS12, Amm08, Bal13b, Kuc12, WS12], which also belong to the group of active coupled physics problems. Both modalities make use of internal measurements of the power density for recovering the conductivity. In an AET experiment, an object is probed by ultrasound waves while making electric measurements on its boundary. A wave sent through the object causes a small change in the conductivity due to thermal expansion of the tissue, which is detectable in the electric measurements. Using a special asymptotic formula for the measured boundary voltages with and without perturbation gives the power density in the interior [ABC$^+$08, KK10]. In comparison, in IAT an electric current in-

jected into the body causes a Joule heating, which results in the emittance of an ultrasound wave by the tissue. Transducers placed around the body record the pressure wave at the surface and the interior power density is obtained by solving the wave equation [GS08, WS12].

A description of other prominent examples of active coupled physics imaging problems such as Quantitative Thermoacoustic Tomography (qTAT) and Quantitative Photoacoustic Tomography (qPAT), exploiting the Joule heating due to microwave excitation or non-ionising laser pulses, respectively, for producing an ultrasound wave, can be found in the surveys [WS12, Kuc12].

Furthermore, we should mention that the high resolution achieved in many coupled physics imaging problems by incorporating internal data can be explained in terms of a general framework proposed in [Bal14]. The basic idea in this method is to linearize a nonlinear inverse problem, i.e., the model equations and the interior data (referred to as a redundant PDE system [Bal14]), and analyse uniqueness and stability of the problem with linear PDE theory, the theory of pseudo-differential operators and ellipticity conditions. In case when the considered problem is non-elliptic, multiple interior measurements are assumed to be available to make the problem more redundant, and thus, closer to elliptic [Bal14]. This analysis was performed for the IAT/AET problem [Bal14], PAT [KS12] and Quantitative Elastography [WS15].

## 1.5 Outline of the Thesis

The structure of this thesis is as follows: in Chapter 2 we provide some mathematical background in the theory of Inverse Problems necessary for this thesis. Hereby, the focus lies especially on iterative regularization methods for the solution of nonlinear ill-posed problems. In Chapter 3 we first consider the forward model of Acousto-Electrical Tomography and then provide an analysis and numerical reconstructions for both the full data and the limited data case. Afterwards, we present an ill-posedness quantification of the problem. In Chapter 4 we consider the forward model of linearized elasticity and then treat the inverse problem of quantitative elastography. We prove a nonlinearity condition and provide numerical reconstructions on both simulated and experimental data. After some conclusions and an outlook in Chapter 5 as well as some appendices summarizing relevant PDE results, the two publications on which this thesis is based are attached.

# Chapter 2

# Mathematical Preliminaries

---

Due to its great practical importance in many scientific and industrial applications, the field of *Inverse Problems* has been actively studied in the last decades. Typical examples of inverse problems include various tomographic techniques for examining the human body and non-destructive testing of materials, geodesic and atmospheric exploration, signal and imaging processing, and inverse scattering. In these problems, described by some known models, one is frequently interested in studying the unknown *cause* for an observed or a desired *effect*. Hence, in the context of real world problems one calls the problem *direct* or *forward*, if one wants to determine the effect given the cause. In turn an *inverse problem* consists in determining the cause given the effect.

Commonly, inverse problems are also ill-posed, which typically manifests itself as an instability of the solution to perturbations in the data, meaning that even a small noise in the data may lead to arbitrarily large errors in the reconstruction of solutions. Hence, a special class of methods has developed to cope with this instability called *regularization methods*. The theory of regularization is well established for linear inverse problems [EHN96] and actively developing for nonlinear problems [KNS08, SKHK12]. In this chapter, we provide an overview of important theoretical results for nonlinear Inverse Problems and regularization theory, as well as an overview of iterative regularization methods, where only methods relevant to this thesis are presented.

## 2.1 Nonlinear Inverse Problems and Regularization

Many inverse problems of practical significance are nonlinear. Therefore, in this chapter we focus on general operator equation of the form

$$F(x) = y\,, \tag{2.1}$$

with a nonlinear operator $F : \mathcal{D}(F) \subset \mathcal{X} \to \mathcal{Y}$, where $\mathcal{D}(F)$ denotes the domain of $F$, and $\mathcal{X}$, $\mathcal{Y}$ are Hilbert spaces with corresponding inner products and norms, respectively. Moreover, we consider measured noisy data $y^\delta \in \mathcal{Y}$ satisfying the error estimate

$$\left\|y - y^\delta\right\| \leq \delta\,, \tag{2.2}$$

where $\delta$ is the noise level, since in practice the exact data $y \in \mathcal{Y}$ are never available due to, e.g., measurement errors.

The well-known Hadamard *well-posedness* criterion [Had23] for problem (2.1) can be mathematically rigorously stated as follows [Kir96]:

**Definition 2.1.1.** *Equation* (2.1) *is called well-posed in the sense of Hadamard, if the following conditions are satisfied:*

- *Existence ($F$ is surjective): $R(F) = \mathcal{Y}$, i.e., for every $y \in \mathcal{Y}$ there exists an $x \in \mathcal{D}(F)$ satisfying* (2.1).
- *Uniqueness ($F$ is injective): For every $y \in \mathcal{Y}$ there exists at most one $x \in \mathcal{D}(F)$ satisfying* (2.1).
- *Stability ($F$ is continuously invertible): The solution $x$ depends continuously on $y$, i.e., for every sequence $\{x_n\} \subset \mathcal{D}(F)$ with $F(x_n) \to F(x)$ for $n \to \infty$, it follows that $x_n \to x$ for $n \to \infty$.*

Unfortunately, in many inverse problems one or more of the above conditions are usually not fulfilled, and in fact they are often ill-posed in the sense of instability of the solution with respect to noise in the data. This instability leads to difficulties in obtaining reliable numerical solutions of these problems and therefore, they have to be *stabilized/regularized* by using available a-priory information or appropriate numerical methods.

Many different regularization methods exist [EHN96, KNS08], two of the most prominent of which are *Tikhonov regularization* and *Landweber iteration*. Typically, regularization methods seek for a solution which is located at a minimal distance from the initial guess. Hence, we make the following

**Definition 2.1.2.** *Let $F : D(F) \subset \mathcal{X} \to \mathcal{Y}$ be a nonlinear operator between the Hilbert spaces $\mathcal{X}$ and $\mathcal{Y}$. Given $x_0 \in \mathcal{X}$, an element $x^\dagger \in \mathcal{X}$ is called an $x_0$-minimum-norm solution of $F(x) = y$ if there holds*

$$F\left(x^\dagger\right) = y\,,$$

*and*

$$\left\|x^\dagger - x_0\right\| = \min_{x \in D(F)} \left\{\|x - x_0\| \mid F(x) = y\right\},$$

*provided that the above minimum exists.*

*Tikhonov regularization* for linear and nonlinear inverse problems has started with two publications by A.N. Tikhonov in 1963 [Tik63a, Tik63b] and has been intensively investigated since then [EHN96, Kir96]. The basic idea of this regularization method lies in the approximation of the solution $x^\dagger$ of equation (2.1) by minimizing the functional

$$\mathcal{T}_\alpha^\delta(x) := \left\|F(x) - y^\delta\right\|^2 + \alpha \left\|x - x_0\right\|^2 , \tag{2.3}$$

where $\alpha > 0$ is a suitable regularization parameter. The initial guess $x_0$ typically includes all known information about the solution. Importantly, under mild assumptions on the operator $F$ one can prove existence of a unique global minimizer $x_\alpha^\delta$ of the Tikhonov functional $\mathcal{T}_\alpha^\delta$ given a properly coupled parameter $\alpha$ and noise level $\delta$ [EHN96]. However, minimizing $\mathcal{T}_\alpha^\delta$ becomes difficult if $F$ is nonlinear, since then the nonlinear functional $\mathcal{T}_\alpha^\delta$ usually has to be minimized using various iterative optimization methods, which may possibly stop at some local minimum only.

## 2.2 Iterative Regularization Methods

As an attractive alternative to Tikhonov regularization, especially for large scale nonlinear inverse problems, *iterative regularization methods* were intensively investigated [EHN96, KNS08], where in general iterative algorithms are directly applied for solving (2.1).

Iterative regularization methods for nonlinear inverse problems were motivated by the consideration of linear problems of the form $Kx = y$, where $K$ is a linear operator between Hilbert spaces. Most iterations are derived by transforming the normal equation

$$K^*Kx = K^*y\,,$$

into the fixed point equation

$$x = x + K^* (y - Kx) \ .$$

It was noticed that $K^* (y - Kx)$ corresponds to the negative gradient direction of the functional

$$\frac{1}{2} \|y - Kx\|^2 \ ,$$

which was then also transferred to the nonlinear case

$$\frac{1}{2} \|y - F(x)\|^2 \ .$$

Assuming that the operator $F$ has a continuous Fréchet derivative $F'(\cdot)$, the direction of negative gradient is given by

$$F'(x)^* (y - F(x)) \ ,$$

which yields the final form of the fixed point equation for nonlinear problems

$$x = x + F'(x)^* (y - F(x)) \ . \tag{2.4}$$

### 2.2.1 Nonlinear Landweber Iteration

Applying fixed point iteration to (2.4) yields *nonlinear Landweber iteration* for the problem (2.1), which, for noisy data $y^\delta \in \mathcal{Y}$, is given by

$$x_{k+1}^\delta = x_k^\delta + F'\left(x_k^\delta\right)^* \left(y^\delta - F\left(x_k^\delta\right)\right) \ , \tag{2.5}$$

and starts with a given initial guess $x_0^\delta = x_0$, $x_0 \in D(F)$. For exact data the iteration is defined analogously, i.e., with $y$ instead of $y^\delta$ and $x_k$ instead of $x_k^\delta$. In the context of classical optimization algorithms, Landweber iteration (2.5) is nothing else than the gradient descent method applied to the functional

$$\Phi^\delta(x) := \frac{1}{2} \left\|y^\delta - F(x)\right\|^2 \ ,$$

and therefore, iteration (2.5) has to be combined with a stopping rule in order to act as a regularization method. Frequently, *Morozov's discrepancy principle* is employed [EHN96], which terminates the iteration early enough with the smallest index $k_* = k_*(\delta, y^\delta)$ satisfying

$$\left\|y^\delta - F\left(x_{k_*}^\delta\right)\right\| \leq \tau\delta < \left\|y^\delta - F\left(x_k^\delta\right)\right\| \ , \qquad 0 \leq k < k_* \ , \tag{2.6}$$

for an appropriately chosen positive number $\tau$ ($\tau \in [1, 2]$ being common practice, see references in [KNS08]).

### 2.2.2 Basic Conditions and Convergence Theorems

For linear inverse problems, Landweber iteration gives rise to a convergent regularization method if stopped by the discrepancy principle, i.e., $x_{k_*}^{\delta} \to x^{\dagger}$ as $\delta \to 0$. However, in the nonlinear case all iterative methods, including Landweber iteration, do not converge globally in general. Nevertheless, one can prove local convergence under some additional assumptions, which we discuss in this section.

First, the problem (2.1) should be scaled properly, i.e., it should satisfy

**Assumption 2.2.1** (Scaling condition)**.** *Let $x_0 \in \mathcal{D}(F)$ and there exists a positive $\rho$ defining a closed ball $\mathcal{B}_{2\rho}(x_0)$ around $x_0$ such that the scaling condition*

$$\|F'(x)\| \leq 1\,, \qquad \forall\, x \in \mathcal{B}_{2\rho}(x_0) \subset \mathcal{D}(F)\,, \tag{2.7}$$

*holds.*

In practice, scaling is usually achieved by estimating the norm of the Fréchet derivative $F'(\cdot)$ at the solution $x^{\dagger}$ (if it is available, e.g., in a simulated problem) through estimating the supremum

$$\left\|F'\left(x^{\dagger}\right)\right\| = \sup_{\|h\|=1} \left\|F'\left(x^{\dagger}\right) h\right\|\,,$$

through $n$ randomly generated functions $\{h_1, \ldots, h_n\}$ as

$$\sup_{i=1,\ldots,n} \frac{\left\|F'\left(x^{\dagger}\right) h_i\right\|}{\|h_i\|}\,, \tag{2.8}$$

and dividing the problem (2.1) by the value found from (2.8).

The next assumptions, the so-called *tangential cone conditions* or *nonlinearity conditions* [HNS95, KNS08] restrict the allowed nonlinearity of the operator $F$ and form the basis of the convergence analysis of iterative regularization methods for nonlinear ill-posed problems. (Note that these conditions are always satisfied for linear problems, although they are not required for proving their convergence.)

**Assumption 2.2.2** ((Strong) tangential cone condition)**.** *The following local condition*

$$\|F(x) - F(\tilde{x}) - F'(x)(x - \tilde{x})\| \leq \eta \|F(x) - F(\tilde{x})\|\,, \tag{2.9}$$

*holds for all $x, \tilde{x} \in \mathcal{B}_{2\rho}(x_0) \subset \mathcal{D}(F)$ for some $\eta < \frac{1}{2}$.*

Both condition (2.7) and (2.9) are strong enough to guarantee local convergence to a solution of the problem (2.1) if it is solvable in $\mathcal{B}_\rho(x_0)$. Additionally, they ensure that all iterates $x_k^\delta$ remain in $\mathcal{D}(F)$ for $0 \leq k \leq k_*$ and thus, Landweber iteration is well defined.

By the triangle inequality, condition (2.9) yields [HNS95]

$$\frac{1}{1+\eta} \|F'(x)(\tilde{x}-x)\| \leq \|F(\tilde{x}) - F(x)\| \leq \frac{1}{1-\eta} \|F'(x)(\tilde{x}-x)\| , \quad (2.10)$$

for all $x, \tilde{x} \in \mathcal{B}_{2\rho}(x_0)$, which implies closedness and convexity of the set of solutions in $\mathcal{B}_\rho(x_0)$. Thus, if the problem (2.1) is solvable in $\mathcal{B}_\rho(x_0)$, inequality (2.10) guarantees the existence of a unique solution of minimal distance to the initial guess $x_0$ by

**Proposition 2.2.1** ( [KNS08], Proposition 2.1)**.** *Let $\rho, \varepsilon > 0$ be such that*

$$\|F(x) - F(\tilde{x}) - F'(x)(x-\tilde{x})\| \leq c(x,\tilde{x}) \|F(x) - F(\tilde{x})\| , \quad (2.11)$$

*with $x, \tilde{x} \in \mathcal{B}_{2\rho}(x_0) \subset \mathcal{D}(F)$ for some $c(x,\tilde{x}) \geq 0$, where $c(x,\tilde{x}) < 1$ if $\|x - \tilde{x}\| \leq \varepsilon$. If $F(x) = y$ is solvable in $\mathcal{B}_\rho(x_0)$, then a unique $x_0$-minimum-norm solution exists. It is characterized as the solution $x^\dagger$ of $F(x) = y$ in $\mathcal{B}_\rho(x_0)$ satisfying the condition*

$$x^\dagger - x_0 \in \mathcal{N}\left(F'\left(x^\dagger\right)\right)^\perp ,$$

*where $\mathcal{N}\left(F'\left(x^\dagger\right)\right)$ denotes the nullspace of $F'\left(x^\dagger\right)$.*

Condition (2.9) is restrictive and as one may notice, Lipschitz continuity of $F'(\cdot)$ is not enough to ensure it, but only the following error bound for the Taylor approximation of the operator $F$

$$\|F(x) - F(\tilde{x}) - F'(x)(x-\tilde{x})\| \leq c \|x - \tilde{x}\|^2 .$$

However, in some occasions one can even show a stronger condition than (2.9), namely

$$\|F(x) - F(\tilde{x}) - F'(x)(x-\tilde{x})\| \leq c \|x - \tilde{x}\| \|F(x) - F(\tilde{x})\| , \quad (2.12)$$

for all $x, \tilde{x} \in \mathcal{B}_{2\rho}(x_0)$ and some constant $c > 0$. Condition (2.12) implies (2.9) but possibly on a smaller ball $\mathcal{B}_{2\rho}(x_0)$. Furthermore, we should mention that the tangential cone conditions appears in the literature in different variants and all of them are used for proving convergence in the strong sense, i.e., a sequence $(x_n) \in \mathcal{X}$ converges to $x \in \mathcal{X}$ if $\|x_n - x\| \to 0$ for $n \to \infty$. It is worth mentioning another variant of the nonlinearity condition, namely

$$\left\|F(x) - F\left(x^\dagger\right) - F'\left(x^\dagger\right)\left(x - x^\dagger\right)\right\| \leq c \left\|x - x^\dagger\right\| \left\|F(x) - F\left(x^\dagger\right)\right\| , \quad (2.13)$$

for all $x \in \mathcal{B}_\rho\left(x^\dagger\right)$, which is a bit weaker than (2.12) and (2.9). However, it is still sufficient for obtaining local convergence. Since the above mentioned tangential cone conditions impose strong restrictions on the operator $F$, they are often difficult to verify for specific problems. However, for example for the problem treated in Paper B we were able to show that condition (2.13) is satisfied.

For exact data $y$ we have the following convergence result:

**Theorem 2.2.2** ( [KNS08], Theorem 2.4)**.** *Assume that conditions* (2.7) *and* (2.9) *hold and that $F(x) = y$ is solvable in $\mathcal{B}_\rho(x_0)$. Then nonlinear Landweber iteration applied to exact data $y$ converges to a solution of $F(x) = y$. If $\mathcal{N}\left(F'\left(x^\dagger\right)\right) \subset \mathcal{N}\left(F'(x)\right)$ for all $x \in \mathcal{B}_\rho\left(x^\dagger\right)$, then $x_k$ converges to $x^\dagger$ as $k \to \infty$.*

As mentioned above, the regularization property of iterative methods is linked to the employed stopping rule. For example, when using (2.6) for terminating the iteration, the number $\tau$ should be chosen appropriately depending on $\eta$ from condition (2.9), for example (due to [KNS08], Proposition 2.2):

$$\tau > 2\frac{1+\eta}{1-2\eta} > 2\,. \tag{2.14}$$

Hence, for noisy data $y^\delta$ convergence of Landweber iteration is provided by the following

**Theorem 2.2.3** ( [KNS08], Theorem 2.6)**.** *Assume that conditions* (2.7) *and* (2.9) *hold and that $F(x) = y$ is solvable in $\mathcal{B}_\rho(x_0)$. Let $k_* = k_*\left(\delta, y^\delta\right)$ be chosen according to the stopping rule* (2.6), (2.14)*. Then the Landweber iterates $x_{k_*}^\delta$ converge to a solution of $F(x) = y$. If $\mathcal{N}\left(F'\left(x^\dagger\right)\right) \subset \mathcal{N}\left(F'(x)\right)$ for all $x \in \mathcal{B}_\rho\left(x^\dagger\right)$, then $x_{k_*}^\delta$ converges to $x^\dagger$ as $\delta \to 0$.*

To obtain convergence rates for Landweber iteration, $x^\dagger$ has to satisfy *source conditions*, for example

$$x^\dagger - x_0 = \left(F'\left(x^\dagger\right)^* F'\left(x^\dagger\right)\right)^\mu v\,, \qquad v \in \mathcal{N}\left(F'\left(x^\dagger\right)\right)^\perp\,. \tag{2.15}$$

For nonlinear Landweber iteration the additional condition

$$F'(x) = R_x F'\left(x^\dagger\right) \qquad \text{and} \qquad \|R_x - I\| \le \left\|x - x^\dagger\right\|\,,$$

for $x \in \mathcal{B}_{2\rho}(x_0)$, is required, where $\{R_x : x \in \mathcal{B}_{2\rho}(x_0)\}$ is a family of bounded linear operators $R_x : \mathcal{Y} \to \mathcal{Y}$ and $c > 0$ is a constant. Under those conditions it is possible to prove [KNS08] the optimal convergence rate

$$\left\|x_{k_*}^\delta - x^\dagger\right\| = \mathcal{O}(\delta^{\frac{2\mu}{2\mu+1}})\,.$$

### 2.2.3 Landweber-type gradient methods

Alternatively to scaling problem (2.1), one could introduce a relaxation parameter $\omega$ in front of $F'\left(x_k^\delta\right)^*\left(y^\delta - F\left(x_k^\delta\right)\right)$, which gives the iteration

$$x_{k+1}^\delta = x_k^\delta + \omega F'\left(x_k^\delta\right)^*\left(y^\delta - F\left(x_k^\delta\right)\right) . \tag{2.16}$$

However, then a necessary assumption in the convergence analysis of Landweber iteration is

$$\omega \left\|F'\left(x^\dagger\right)\right\|^2 \leq 1 ,$$

instead of (2.7), which implies a restriction on $\omega$.

Furthermore, we can generalize nonlinear Landweber iteration (2.16) to the following family of *Landweber-type gradient methods*:

$$\begin{aligned} x_{k+1}^\delta &= x_k^\delta + \omega_k^\delta\left(x_k^\delta\right) s_k^\delta\left(x_k^\delta\right) , \\ s_k^\delta(x) &:= F'(x)^*\left(y^\delta - F(x)\right) , \end{aligned} \tag{2.17}$$

where for the stepsize $\omega_k^\delta$ we can for example either use a constant stepsize $\omega$, which corresponds to classical Landweber iteration (2.16) [EHN96] and acts as a scaling, or the steepest descent stepsize [EHN96, Sch96]

$$\omega_k^\delta(x) := \frac{\left\|s_k^\delta(x)\right\|^2}{\left\|F'(x)\, s_k^\delta(x)\right\|^2} , \tag{2.18}$$

the minimal error stepsize [EHN96, KNS08]

$$\omega_k^\delta(x) := \frac{\left\|y^\delta - F(x)\right\|^2}{\left\|s_k^\delta(x)\right\|^2} , \tag{2.19}$$

or the recently introduced [Neu17a] stepsize

$$\omega_k^\delta(x) := \frac{(1-\eta)\left\|y^\delta - F(x)\right\|^2 - \delta\left\|y^\delta - F(x)\right\|(1+\eta)}{\left\|s_k^\delta(x)\right\|^2} , \tag{2.20}$$

where $\eta$ is the nonlinearity parameter introduced above.

The gradient method (2.17) with stepsize either given by (2.18),(2.19) or (2.20) has been shown to be well-defined, with monotonically decreasing errors, i.e.,

$$\left\|x_{k+1}^\delta - x_*\right\| \leq \left\|x_k^\delta - x_*\right\| ,$$

for a solution $x_* \in \mathcal{B}_\rho(x_0)$, and convergent [KNS08, Neu17a] provided that the operator $F$ has a continuous Fréchet derivative $F'(\cdot)$, the stopping rule (2.6),

(2.14) is used, any of the above tangential cone conditions holds and the chosen stepsize is bounded from below by $\omega^{-2}$, where $\omega$ is defined by

$$\omega := \sup_{x \in \mathcal{B}_{2\rho}(x_0)} \|F'(x)\| < \infty \,.$$

### 2.2.4 Nesterov's acceleration strategy

As is well known, gradient-type methods are easy to realize numerically. However, they are quite slow, requiring a rather large number of iterations. In order to speed up the iteration, we employ *Nesterov's acceleration strategy* [Nes83], i.e., we use the modified iteration

$$\begin{aligned} z_k^\delta &= x_k^\delta + \tfrac{k-1}{k+2} \left( x_k^\delta - x_{k-1}^\delta \right) , \\ x_{k+1}^\delta &= z_k^\delta + \omega_k^\delta \left( z_k^\delta \right) s_k^\delta \left( z_k^\delta \right) , \end{aligned} \tag{2.21}$$

starting with $x_0^\delta = x_{-1}^\delta = x_0$. For linear inverse problems it was shown in [Neu17b] that the above algorithm converges. Furthermore, in [HR17] it was shown that convergence is also guaranteed for nonlinear inverse problems under a tangential cone condition if instead of the choice $(k-1)/(k+2)$ suitable parameters $\lambda_k^\delta$ are used. Even though the choice $\lambda_k^\delta = (k-1)/(k+2)$ is not covered by the theory developed in [HR17], the numerical examples presented there show its usefulness in practical situations, see also [Jin16].

### 2.2.5 Landweber-Kaczmarz Iteration

An interesting alternative to Landweber iteration for solving the equation (2.1), where the operator $F$ is given by

$$F := (F_1, \ldots, F_M) : \bigcap_{i=1}^{M} \mathcal{D}\left(F_i\right) \subset \mathcal{X} \to \mathcal{Y}^M \,, \tag{2.22}$$

and the measured noisy data $y^\delta = \left(y_1^\delta, \ldots, y_M^\delta\right)$, $M > 1$, of the exact data $y = (y_1, \ldots, y_M)$, $M > 1$, satisfy

$$\left\| y_i - y_i^\delta \right\| \leq \delta_i \,, \tag{2.23}$$

with the noise level $\delta := (\delta_1, \ldots, \delta_M)$, was motivated by considering the problem as a system of equations and using the principle idea of Kazcmarz's method.

Landweber iteration applied to (2.1) involves a summation over all operator components as follows

$$x_{k+1}^{\delta} = x_k^{\delta} + \omega \sum_{i=1}^{M} F_i'\left(x_k^{\delta}\right)^* \left(y_i^{\delta} - F_i\left(x_k^{\delta}\right)\right) .$$

However, this does not exploit the underlying structure of the problem. Hence, instead of going through all operator components in each iteration, the *Landweber-Kaczmarz method* [KS02, HLS07] employs Landweber iteration steps cyclically, which defines

$$x_{k+1}^{\delta} = x_k^{\delta} + \omega\, F_{r(k)}'\left(x_k^{\delta}\right)^* \left(y_{r(k)}^{\delta} - F_{r(k)}\left(x_k^{\delta}\right)\right) , \tag{2.24}$$

where $r(k) := \mathrm{mod}\,(k, M)+1$. The main advantage of this iteration procedure is that in each iteration step only $1/M$ of the amount of work of Landweber iteration has to be carried out, which makes it more efficient compared to Landweber iteration, especially if $M$ is large or the evaluations of $F_i$ and $F_i'$ are expensive.

For stopping the iteration, it was proposed in [HLS07, KNS08] to modify (2.24) as follows

$$x_{k+1}^{\delta} = x_k^{\delta} + \omega_k^{\delta}\, F_{r(k)}'(x_k^{\delta})^*(y_{r(k)}^{\delta} - F_{r(k)}(x_k^{\delta}))\,, \tag{2.25}$$

where

$$\omega_k^{\delta} := \begin{cases} \omega\,, & \tau\delta_{r(k)} < \left\| y_{r(k)}^{\delta} - F_{r(k)}(x_k^{\delta}) \right\| , \\ 0\,, & \text{else}\,, \end{cases} \tag{2.26}$$

and to stop the iteration when for the first time $\omega_k^{\delta} = 0$ over a full cycle of iterations, i.e., an update is omitted within one cycle if the corresponding $i$-th residual is sufficiently small. This idea can also be generalized to the steepest descent stepsize (2.18) [CHLS08] and is usually referred to in the literature as the *loping Kaczmarz-type method*.

It is worth mentioning that in case of noise free data, the classical and the loping version of the Landweber-Kaczmarz iteration, i.e., (2.24) and (2.25), (2.26), are identical. However, for noisy data the loping version (2.25), (2.26) makes sure that all components of the residual vector $\left\|y_i^{\delta} - F_i\left(x_k^{\delta}\right)\right\|$ fall below a certain threshold, while the classical version compares only the Euclidean norms of the residual components $\sqrt{\sum_{i=1}^{M} \left\|y_i^{\delta} - F_i\left(x_k^{\delta}\right)\right\|^2}$ to a threshold. Thus, the convergence of the residual in the maximum norm better exploits the pointwise noise-estimates (2.23) than standard methods. Additionally, the evaluation of $F_{r(k)}'$ might be loped, making computations fast in the loping version.

In order to prove convergence and stability of the Landweber-Kaczmarz method, the same conditions on the operators $F_i$ are required as for the operator $F$ in

proving convergence and stability of Landweber iteration, i.e., each operator component should satisfy the scaling condition (2.7) and the tangential cone condition (2.9). If so, convergence of the Landweber-Kaczmarz method is guaranteed by Theorem 2.3, [HLS07], in the case of noisy data. A similar analysis applied to the method with the steepest descent stepsize can be found in [CHLS08]. Note that the convergence conditions for the Landweber-Kaczmarz method are stronger than for Landweber iteration, since the tangential cone condition has to hold component wise.

An important note for the loping Kaczmarz-type iterations is that the stopping index $k_*$ does not play the role of the regularization parameter like in standard iterative regularization methods, because the iterates $x_k^\delta$ do not depend continuously on the data $y_i^\delta$ for fixed $k$. However, the sequence of parameters $(\omega_k)$ fulfils this role, for which the iterates depend continuously on the data [HLS07,KNS08].

Convergence rate results can be found in [KL14] and the references therein.

### 2.2.6 Levenberg-Marquardt Iteration

As an alternative to Landweber-type gradient methods for solving the operator equation $F(x) = y$, one can use second order iterative methods, such as *Newton-type methods*, which consist in repeated linearization of the equation around some approximate solution $x_k^\delta$, and then solving the linearized problem

$$F'\left(x_k^\delta\right)\left(x_{k+1}^\delta - x_k^\delta\right) = y^\delta - F\left(x_k^\delta\right) , \tag{2.27}$$

to find $x_{k+1}^\delta$. Unluckily, if the problem (2.1) is ill-posed then the linearized problems are usually also ill-posed and require regularization. A well-known example of such methods is the *Levenberg-Marquardt method* [Han97, Jin10], derived by applying Tikhonov regularization to (2.27), which can be seen as minimizing the functional

$$\Phi^\delta(z) := \left\|y^\delta - F\left(x_k^\delta\right) - F'\left(x_k^\delta\right) z\right\|^2 + \alpha_k \|z\|^2 ,$$

with the penalty term $\alpha_k \|z\|^2$, and which yields the iteration

$$x_{k+1}^\delta = x_k^\delta + \left(F'\left(x_k^\delta\right)^* F'\left(x_k^\delta\right) + \alpha_k I\right)^{-1} F'\left(x_k^\delta\right)^* \left(y^\delta - F'\left(x_k^\delta\right)\right) , \tag{2.28}$$

where $\alpha_k$ is an appropriately chosen sequence of regularization parameters. [Han97] gives some suggestions on how to a-posteriori determine $\alpha_k$ by a discrepancy principle and proves a convergence result under the assumptions of uniform boundedness of $F'(\cdot)$ in $\mathcal{B}_\rho\left(x^\dagger\right)$ and the tangential cone condition (2.12), using a discrepancy principle as a stopping rule.

Alternatively, one can use the a-priori rule

$$\alpha_k = \alpha_0 q^k \,, \tag{2.29}$$

for some $\alpha_0 > 0$ and $q \in (0,1)$, for which even convergence rates can be obtained under additional assumptions including a source condition ( [KNS08], Theorem 4.7).

The advantage of Newton-type methods [KNS08] is that they meet their stopping criteria in much less iterations than Landweber-type gradient methods. However, each iteration might take considerably longer than one step of Landweber iteration due to assembling and solving a linear system with the operator

$$F'\left(x_k^\delta\right)^* F'\left(x_k^\delta\right) + \alpha_k I \,.$$

In practice this frequently results in solving a huge dense linear system of equations each iteration, which can be computationally costly.

### 2.2.7 Levenberg-Marquardt-Kaczmarz Iteration

Kaczmarz's strategy can be used in connection with many iterative methods for solving ill-posed problem, e.g., as we saw in Section 2.2.5 for Landweber-type gradient methods, and this idea can be exploited for Netwon-type methods as well.

The Levenberg-Marquardt iteration applied for solving the problem (2.1) with the operator $F$ defined by (2.22) is given by [BKA10] as follows

$$x_{k+1}^\delta = x_k^\delta + \left(\sum_{i=1}^M F_i'\left(x_k^\delta\right)^* F_i'\left(x_k^\delta\right) + \alpha_k I\right)^{-1} \sum_{i=1}^M F_i'\left(x_k^\delta\right)^* \left(y_i^\delta - F_i'\left(x_k^\delta\right)\right) \,. \tag{2.30}$$

As can be noticed, this approach deals with big system matrices at each iteration step and does not exploit the structure of the problem. Motivated by Kaczmarz's idea, the Levenberg-Marquardt method can be employed cyclically at each iteration step, which motivates the *Levenberg-Marquardt-Kaczmarz approach*

$$x_{k+1}^\delta = x_k^\delta + \left(F_{r(k)}'\left(x_k^\delta\right)^* F_{r(k)}'\left(x_k^\delta\right) + \alpha_k I\right)^{-1} F_{r(k)}'\left(x_k^\delta\right)^* \left(y_{r(k)}^\delta - F_{r(k)}'\left(x_k^\delta\right)\right) \,, \tag{2.31}$$

where $r(k) := \mathrm{mod}\,(k, M) + 1$. Analogously to [HLS07, CHLS08, KS02], a *loping* version of the *Levenberg-Marquardt-Kaczmarz method* was proposed in [BKA10]

by equipping the iteration

$$x_{k+1}^{\delta} = x_k^{\delta} + \omega_k^{\delta} \left( F'_{r(k)} \left( x_k^{\delta} \right)^* F'_{r(k)} \left( x_k^{\delta} \right) + \alpha_k I \right)^{-1} F'_{r(k)} \left( x_k^{\delta} \right)^* \left( y_{r(k)}^{\delta} - F'_{r(k)} \left( x_k^{\delta} \right) \right) , \tag{2.32}$$

with the stopping rule

$$\omega_k^{\delta} := \begin{cases} 1 , & \tau \delta_{r(k)} < \left\| y_{r(k)}^{\delta} - F_{r(k)}(x_k^{\delta}) \right\| , \\ 0 , & \text{else} . \end{cases} \tag{2.33}$$

According to this rule, the iteration is terminated when all iterates $x_k^{\delta}$ are equal for the first time within a cycle of $M$ subsequent steps.

Similar observations discussed in Section 2.2.5 on the residual vector and the problem structure also hold for the Levenberg-Marquardt-Kaczmarz iteration. Under basic assumptions, a convergence result for the iteration (2.31) and a semi-convergence result for the iteration (2.32) were established in [BKA10].

# Chapter 3

# Acousto-Electrical Tomography

---

In this chapter, we present the main results of Paper A, which treats the inverse problem of estimating the conductivity distribution of an object from internal measurements of the power density. First, we present some background information on EIT and AET, followed by a concise treatment of the considered forward problem, which serves as a starting point for this investigation. For the inverse problem, which is stated as a nonlinear operator equation in Hilbert spaces, we generalize the derivation of essential theoretical results in an infinite dimensional setting, deriving the Fréchet derivative and its adjoint of the nonlinear operator. Afterwards, analogously to [BNSS13, GS08], we look at the inverse problem where the underlying PDE model is equipped with Dirichlet boundary conditions and solve it using the Levenberg-Marquardt method. Then, we experiment with speeding up the method by implementing the Kaczmarz idea, which takes advantage of the multiple measurement structure of the problem. For both methods, numerical results on simulated power density data are presented. Afterwards, motivated by a potential application of AET for the detection of breast cancer, where accessibility of the measurement boundary is limited, we investigate the limited angle case for our problem. This leads to the same setting as before but with the Dirichlet boundary conditions replaced by certain Neumann boundary conditions, corresponding to a current density application on the boundary. We show how this limited angle setting influences the reconstruction quality based on numerical experiments. Furthermore, we present results on an ill-posedness quantification of the problem based on the Fréchet derivative of the underlying nonlinear operator.

## 3.1 From EIT to AET

*Electrical Impedance Tomography* (EIT) is an imaging modality for mapping the *conductivity* of materials based on electric boundary measurements, which are acquired using electrodes placed on the surface of a body [Hol05, Bor02, CIN99]. Usually, a low-frequency current is applied on the electrodes and the resulting voltage is measured. The measurement data are used for recovering quantitative and structural information about the conductivity of the body and can potentially be valuable for medical and industrial applications. Attention to this imaging modality was drawn when it was noticed that, for example in medicine, a malignant tissue exhibits a much higher conductivity value than a healthy tissue, and in general, materials and tissues have a high contrast. However, due to ill-posedness, EIT faces difficulties in resolving this contrast.

Furthermore, in examples of EIT for the detection of breast cancer it has the potential to become a safe and low-cost alternative to conventional Computerized Tomography. Other applications of EIT include pulmonary and cardiac imaging, monitoring of brain functions for medicine, non-destructive testing and process tomography in industry. A comprehensive survey of applications can be found for example in [Hol05, MS12] and the references therein.

However, the underlying mathematical problem, which goes back to a paper by A. Calderón from 1980 [Cal80], is known for being nonlinear and (severely) ill-posed [Ale88, Bor02], i.e., strongly unstable with respect to measurement noise. The inverse problem of EIT is based on different mathematical models (see for example [CIN99, MS12]), all of which are based on the conductivity equation

$$\operatorname{div}(\sigma \nabla u) = 0\,, \qquad \text{in } \Omega\,,$$

where $u$ is the electric potential, and it is interested in identifying the conductivity $\sigma$ inside a body from electric boundary measurements performed on the surface of the body. For example, in the original formulation from [Cal80], a continuous boundary potential

$$u|_{\partial\Omega} = f\,,$$

is applied on the boundary and the resulting current density

$$(\sigma \nabla u) \cdot \vec{n}|_{\partial\Omega}\,,$$

is measured. The conductivity $\sigma$ is reconstructed from the Dirichlet-to-Neumann map

$$\Lambda_\sigma : u|_{\partial\Omega} \to (\sigma \nabla u) \cdot \vec{n}|_{\partial\Omega}\,.$$

The nonlinearity and severe ill-posedness of the problem leads to a poor image resolution and a low sensitivity to inclusions located far from the boundary. For

certain applications, for example the detection of breast cancer, the measurement boundary is confined only to a part of the body surface, which makes the problem even more difficult to solve.

There exists a vast amount of literature on identifiability of the conductivity, stability and different reconstruction methods. See for example [Bor02, Hol05, AGL15, MS12] and the references therein. Standard approaches to the EIT problem are either based on minimizing a cost functional for the measured data or on applying a direct method. Existence and uniqueness of the inverse problem in EIT was investigated in [SU87, SCI92, AP06, Nac96].

To overcome the ill-posedness of the classical EIT problem, coupling with different physical phenomena, e.g., based on magnetic resonance or ultrasound, was promoted in recent decades, which resulted in a class of tomography problems with *hybrid data* (see [WS12] for a comprehensive overview). In many cases, using additional interior information leads to a significant improvement of the conductivity reconstructions exhibiting both a high contrast and a high resolution. In this thesis, we focus on coupled physics imaging problems in EIT with interior data based on ultrasound, such as Acousto-Electrical Tomography (AET) [ZW04, ABC+08, KK10] and Impedance-Acoustic Tomography (IAT) [GS08], where one aims at reconstructing the spatially varying *conductivity* $\sigma$ inside a body from various measurements of the *power density*. Those two modalities may potentially become useful in medical applications as an improved alternative to classical EIT.

A number of iterative reconstruction techniques was developed for determining the conductivity from the power density, such as methods based on minimization of a functional [ABC+08, CFdGK09, HK14], solution of the transport equation or the 0-Laplacian elliptic equations [KK10, KK11, GS08], or complex geometric optics solutions [Koc12, Bal13a]. Questions of uniqueness and stability in two dimensions were addressed in [CFdGK09] for three power densities originating from two boundary measurements, which was generalized to three dimensions in [BBMT13] with multiple power densities, and in [Koc12] for one boundary measurement. Furthermore, a stability result for two and more power densities is presented in [KS12].

## 3.2 Mathematical Model of AET

In this section, we introduce the basic notations and recall some basic results on PDEs required. Throughout this section, we make the following

**Assumption 3.2.1.** *Let $\Omega$ denote a non-empty, bounded, open and connected*

*set in* $\mathbb{R}^N$, $N = 2, 3$, *with boundary* $\Gamma = \partial\Omega \in C^{1,1}$. *Furthermore, let* $g_D \in H^{\frac{1}{2}}(\Gamma)$ *and* $g_N \in H^{\frac{1}{2}}(\Gamma)$ *be given such that*

$$\int_{\partial\Omega} g_N \, dS = 0 \,. \tag{3.1}$$

Maxwell's equations serve as a starting point for deriving the electrostatic equation of EIT [Bor02, Hol05]. The governing equation describes the connection between the electric potential $u$ and the conductivity $\sigma$ by

$$\operatorname{div}(\sigma \nabla u) = 0 \,, \qquad \text{in } \Omega \,, \tag{3.2}$$

supplied with suitable boundary conditions. As mentioned above, in this thesis we consider both Dirichlet boundary conditions of the form

$$u|_{\partial\Omega} = g_D \,, \tag{3.3}$$

corresponding to different prescribed boundary potentials $g_D$, and Neumann boundary conditions

$$(\sigma \nabla u) \cdot \vec{n}|_{\partial\Omega} = g_N \,, \tag{3.4}$$

where $g_N$ is the prescribed boundary current, which are often used in AET and IAT [BNSS13, CFdGK09, ABC+08].

Since we want to consider weak solutions of (3.2), we define the spaces

$$V_0 := H_0^1(\Omega) \,, \qquad \text{where} \qquad H_0^1(\Omega) := \{u \in H^1(\Omega) \,|\, u|_\Gamma = 0\} \,,$$

and

$$V_g := H_{g_D}^1(\Omega) \,, \qquad \text{where} \qquad H_{g_D}^1(\Omega) := \{u \in H^1(\Omega) \,|\, u|_\Gamma = g_D\} \,,$$

and

$$V := H_\diamond^1(\Omega) \,, \qquad \text{where} \qquad H_\diamond^1(\Omega) := \left\{ u \in H^1(\Omega) \,\middle|\, \int_\Omega u \, dx = 0 \right\} \,,$$

and the bilinear and linear forms

$$a_\sigma(u, v) := \int_\Omega \sigma \, \nabla u \cdot \nabla v \, dx \,, \qquad \text{and} \qquad l(v) := \int_{\partial\Omega} g_N \, v \, dS \,.$$

Note that both $a_\sigma(u, v)$ and $l(v)$ are well-defined for $u, v \in H^1(\Omega)$.

In order to be able to guarantee existence and uniqueness of weak solutions of (3.2), (3.3) or (3.2), (3.4), some restrictions on the conductivity parameter $\sigma$ need to be enforced. Hence, we define the following set of admissible conductivity parameters

$$\mathcal{M}(\underline{\sigma}) := \{\sigma \in L^\infty(\Omega) \,|\, \sigma \geq \underline{\sigma}/2 > 0\} \,.$$

### 3.2.1 Dirichlet Boundary Value Problem

Given a prescribed boundary voltage $g_D$ and a conductivity parameter $\sigma$, the forward problem of AET with pure Dirichlet boundary conditions consists in finding $u$ satisfying (3.2), (3.3).

**Definition 3.2.1.** *A function $u \in V_g$ satisfying the variational problem*

$$a_\sigma(u, v) = 0\,, \qquad \forall\, v \in V_0\,, \tag{3.5}$$

*is called a weak solution of the AET problem (3.2) with Dirichlet boundary conditions.*

Furthermore, in the following we always assume that there exists a $\Phi \in H^1(\Omega)$ such that $\Phi|_\Gamma = g_D$, and that there exists a constant $c_D > 0$ such that

$$\|\Phi\|_{H^1(\Omega)} \leq c_D \|g_D\|_{H^{\frac{1}{2}}(\Gamma)}\,. \tag{3.6}$$

This is necessary for proving existence and uniqueness of the forward problem (3.2), (3.3). The inequality (3.6) follows immediately [McL00] from the assumption that $g_D \in H^{\frac{1}{2}}(\Gamma)$. The existence and uniqueness of a weak solutions follows from the Lax-Milgram Lemma, which results in the following:

**Theorem 3.2.1.** *Let Assumption 3.2.1 hold and assume that the conductivity $\sigma \in \mathcal{M}(\underline{\sigma})$ for some $\underline{\sigma} > 0$. Furthermore, let $g_D \in H^{\frac{1}{2}}(\Gamma)$ and $\Phi \in H^1(\Omega)$ with $\Phi|_\Gamma = g_D$ such that (3.6) holds. Then there exists a unique weak solution $u \in V_g$ of (3.2), (3.3) in the sense of Definition 3.2.1. Moreover, there exists a constant $c_{LM} > 0$ such that*

$$\|u\|_{H^1(\Omega)} \leq c_{LM} \left( c_D \|\sigma\|_{L^\infty(\Omega)} \|g_D\|_{H^{\frac{1}{2}}(\Gamma)} \right) + c_D \|g_D\|_{H^{\frac{1}{2}}(\Gamma)}\,.$$

*Proof.* This standard result can for example be found in [GT98]. □

Since the solution $u$ of (3.5) depends essentially on $\sigma$, we often write $u(\sigma)$ instead of $u$ in the remainder of this chapter. The following proposition shows that $u(\sigma)$ depends continuously on $\sigma$.

**Proposition 3.2.2.** *Let $\sigma, \bar{\sigma} \in \mathcal{M}(\underline{\sigma})$. Then for the functions $u(\sigma)$ and $u(\bar{\sigma})$ there holds*

$$\|u(\sigma) - u(\bar{\sigma})\|_{H^1(\Omega)} \leq c_{LM} \|\sigma - \bar{\sigma}\|_{L^\infty(\Omega)} \|u(\bar{\sigma})\|_{H^1(\Omega)}\,.$$

*Proof.* By their definition, $u(\sigma) \in V_g$ and $u(\bar{\sigma}) \in V_g$ satisfy the variational problems

$$a_\sigma(u(\sigma), v) = 0\,, \qquad \forall\, v \in V_0\,,$$

and

$$a_{\bar{\sigma}}(u(\bar{\sigma}), v) = 0\,, \qquad \forall\, v \in V_0\,.$$

Subtracting the above equations, we get

$$a_\sigma(u(\sigma), v) - a_{\bar{\sigma}}(u(\bar{\sigma}), v) = 0\,, \qquad \forall\, v \in V_0\,,$$

which can be rewritten into

$$a_\sigma(u(\sigma) - u(\bar{\sigma}), v) = -a_{\sigma-\bar{\sigma}}(u(\bar{\sigma}), v)\,, \qquad \forall\, v \in V_0\,.$$

Hence, since $u(\sigma) - u(\bar{\sigma}) \in V_0$, by the Lax-Milgram Lemma, there follows

$$\|u(\sigma) - u(\bar{\sigma})\|_{H^1(\Omega)} \leq c_{LM} \|\sigma - \bar{\sigma}\|_{L^\infty(\Omega)} \|u(\bar{\sigma})\|_{H^1(\Omega)}\,,$$

which shows the assertion. □

Note also that in this case one has the following regularity result:

**Theorem 3.2.3.** *Assume that $\Gamma \in C^{1,1}$, $\sigma \in C^{0,1}(\Omega)$, and $g_D \in H^{\frac{3}{2}}(\Gamma)$. Then the unique weak solution $u \in V_g$ of (3.7) satisfies the additional regularity $u \in H^2(\Omega)$ with*

$$\|u\|_{H^2(\Omega)} \leq C \|u\|_{H^1(\Omega)} + C \|g_D\|_{H^{\frac{3}{2}}(\Gamma)}\,.$$

*Furthermore, $u$ solves (3.2), (3.3) pointwise almost everywhere.*

*Proof.* This standard result can for example be found in [GT98]. □

### 3.2.2 Neumann Boundary Value Problem

Given a prescribed boundary current $g_N$ and a conductivity parameter $\sigma$, the forward problem of AET with pure Neumann boundary conditions consists in finding $u$ satisfying (3.2), (3.4), where $\vec{n}$ is an outward unit normal vector of $\partial\Omega$.

**Definition 3.2.2.** *A function $u \in V$ satisfying the variational problem*

$$a_\sigma(u, v) = l(v)\,, \qquad \forall\, v \in V\,, \tag{3.7}$$

*is called a weak solution of the AET problem (3.2) with pure Neumann boundary conditions. We sometimes write $u(\sigma)$ instead of $u$.*

Concerning the existence and uniqueness of weak solutions, we get the following

**Theorem 3.2.4.** *Let Assumption 3.2.1 hold and assume that the conductivity $\sigma \in \mathcal{M}(\underline{\sigma})$ for some $\underline{\sigma} > 0$. Then there exists a unique weak solution $u \in V$ of (3.2), (3.4) in the sense of Definition 3.2.2. Moreover, there exists a constant $c_{LM} > 0$ such that*

$$\|u\|_{H^1(\Omega)} \leq c_{LM} \left( c_T \|g_N\|_{H^{\frac{1}{2}}(\Gamma)} \right) .$$

*Proof.* This standard result follows immediately from the Lax-Milgram Lemma by the Poincaré inequality [Eva98]. □

Concerning the dependence of $u(\sigma)$ on $\sigma$, we have

**Proposition 3.2.5.** *For $\sigma, \bar{\sigma} \in \mathcal{M}(\underline{\sigma})$ there holds*

$$\|u(\sigma) - u(\bar{\sigma})\|_{H^1(\Omega)} \leq c_{LM} \|\sigma - \bar{\sigma}\|_{L^\infty(\Omega)} \|u(\bar{\sigma})\|_{H^1(\Omega)} .$$

*Proof.* By their definition, $u(\sigma) \in V$ and $u(\bar{\sigma}) \in V$ satisfy the variational problems

$$a_\sigma(u(\sigma), v) = l(v) , \qquad \forall\, v \in V ,$$

and

$$a_{\bar{\sigma}}(u(\bar{\sigma}), v) = l(v) , \qquad \forall\, v \in V .$$

Subtracting the above equations, we get

$$a_\sigma(u(\sigma), v) - a_{\bar{\sigma}}(u(\bar{\sigma}), v) = 0 , \qquad \forall\, v \in V ,$$

which can be rewritten into

$$a_\sigma(u(\sigma) - u(\bar{\sigma}), v) = -a_{\sigma - \bar{\sigma}}(u(\bar{\sigma}), v) , \qquad \forall\, v \in V .$$

Since $u(\sigma) - u(\bar{\sigma}) \in V$, there follows by the Lax-Milgram Lemma

$$\|u(\sigma) - u(\bar{\sigma})\|_{H^1(\Omega)} \leq c_{LM} \|\sigma - \bar{\sigma}\|_{L^\infty(\Omega)} \|u(\bar{\sigma})\|_{H^1(\Omega)} ,$$

which shows the assertion. □

In addition to continuous dependence on $\sigma$, $u(\sigma)$ is even Fréchet differentiable with respect to $\sigma$, which is the main result of the following

**Proposition 3.2.6.** *The function $u(\sigma)$ defined by (3.7) and considered as an operator from $\mathcal{M}(\underline{\sigma}) \to L^2(\Omega)$ for some $\underline{\sigma} > 0$ is Fréchet differentiable for all $\sigma \in \mathcal{M}(2\underline{\sigma})$. The Fréchet derivative $u'(\sigma)h \in V$ is given as the unique solution of the variational problem*

$$a_\sigma(u'(\sigma)h, v) = -a_h(u(\sigma), v)\,, \qquad \forall\, v \in V\,. \tag{3.8}$$

*Proof.* We start by taking $\sigma, h \in \mathcal{M}(2\underline{\sigma})$ with $h$ small enough such that $\sigma + h \in \mathcal{M}(\underline{\sigma})$ and define $z \in V$ as the weak solution of the variational problem

$$a_\sigma(z, v) = -a_h(u(\sigma), v)\,, \qquad \forall\, v \in V\,, \tag{3.9}$$

which, by the Lax-Milgram Lemma exists, is unique and satisfies

$$\|z\|_{H^1(\Omega)} \leq c_{LM} \|h\|_{L^\infty(\Omega)} \|u(\sigma)\|_{H^1(\Omega)}\,.$$

Next, we look at $u(\sigma + h) \in V$, which is well defined since $\sigma + h \in \mathcal{M}(\underline{\sigma})$. By its definition, $u(\sigma + h)$ is the unique solution of

$$a_{\sigma+h}(u(\sigma + h), v) = l(v)\,, \qquad \forall\, v \in V\,.$$

Together with (3.9) and the fact that $u(\sigma)$ solves the variational problem (3.7) we get

$$a_{\sigma+h}(u(\sigma + h), v) - a_\sigma(u(\sigma), v) - a_\sigma(z, v) = a_h(u(\sigma), v)\,, \qquad \forall\, v \in V\,,$$

which simplifies to

$$a_\sigma(u(\sigma + h) - u(\sigma) - z, v) = a_h(u(\sigma), v) - a_h(u(\sigma + h), v)\,, \qquad \forall\, v \in V\,.$$

Hence, it follows from the Lax-Milgram Lemma that

$$\|u(\sigma + h) - u(\sigma) - z\|_{H^1(\Omega)} \leq c_{LM} \|h\|_{L^\infty(\Omega)} \|u(\sigma) - u(\sigma + h)\|_{H^1(\Omega)}\,,$$

from which, by Proposition 3.2.5 the assertion immediately follows. □

Analogously, this result can also be established for the pure Dirichlet case, i.e., for $u(\sigma)$ defined by (3.5), see for example [BNSS13].

Furthermore, we also have a regularity result:

**Theorem 3.2.7.** *Let Assumption 3.2.1 be satisfied and let $\sigma \in C^{0,1}(\Omega)$ with $\sigma \geq \underline{\sigma} > 0$. Then the unique weak solution $u \in V$ of (3.7) satisfies the additional regularity $u \in H^2(\Omega)$ with*

$$\|u\|_{H^2(\Omega)} \leq C \|u\|_{H^1(\Omega)} + C \|g_N\|_{H^{\frac{1}{2}}(\Gamma)}\,.$$

*Furthermore, $u$ solves (3.2) pointwise almost everywhere.*

*Proof.* This result can for example be found in [McL00]. □

*Remark.* Note that the regularity result above is also valid if instead of (3.2) one considers $\operatorname{div}(\sigma\nabla u) = f$, where $f \in L^2(\Omega)$ is such that

$$\int_\Omega f\,dx + \int_{\partial\Omega} g_N\,dS = 0\,.$$

This implies that if $h \in C^{0,1}(\Omega)$, then due to (3.1), $u'(\sigma)h$ satisfies

$$\begin{aligned} \operatorname{div}(\sigma\nabla(u'(\sigma)h)) &= -\operatorname{div}(h\nabla u(\sigma))\,, \qquad \text{in } \Omega\,,\\ (\sigma\nabla(u'(\sigma)h))\cdot\vec{n}|_{\partial\Omega} &= 0\,. \end{aligned}$$

## 3.3 The Inverse Problem

In this section we provide essential theoretical results for constructing computational methods below. After considering the forward problem of AET, we now turn to the inverse problem of interest to us, which is to estimate the conductivity parameter $\sigma$ via measurements of the so-called *power density* inside the domain. If $u(\sigma)$ is a solution of (3.5) or (3.7), then the power density $E = E(\sigma)$ is defined as follows

$$E(\sigma) := \sigma\,|\nabla u(\sigma)|^2\,. \tag{3.10}$$

It is known that one measurement of the power density is not enough for the unique reconstruction of the conductivity. However, according to [CFdGK09] this is possible for measurements of the form

$$\left(\sigma\,|\nabla u_1(\sigma)|^2\,, \sigma\,|\nabla u_2(\sigma)|^2\,, \sigma\,\nabla u_1(\sigma)\cdot\nabla u_2(\sigma)\right)\,,$$

with

$$\det(\nabla u_1(\sigma), \nabla u_2(\sigma)) \geq c > 0\,,$$

where $u_1$, $u_2$ are two solutions of (3.2), (3.3) with different boundary data $g_{D,1}$, $g_{D,2}$. Based on this knowledge, we consider multiple measurements in the numerical section below. However, for ease of derivation, basic theoretical results are given for the single measurement case and then briefly generalized to the multiple measurements case.

More precisely, the problem in the single measurement case reads as follows:

**Problem.** *Let Assumption 3.2.1 hold and let $E^\delta \in L^2(\Omega)$ be a measurement of the true power density $E$ satisfying*

$$\left\|E - E^\delta\right\|_{L^2(\Omega)} \leq \delta\,, \tag{3.11}$$

*where $\delta \geq 0$ is the noise level. Given the model (3.2), (3.3) or (3.2), (3.4) in the weak form (3.5) or (3.7), respectively, the problem is to find the conductivity $\sigma$.*

This problem can be formulated as the solution of the nonlinear operator equation

$$F(\sigma) = E\,, \tag{3.12}$$

with the operator

$$\begin{aligned} F : \mathcal{D}_s(F) := \{\sigma \in H^s(\Omega) \,|\, \sigma \geq \underline{\sigma} > 0\} &\to L^2(\Omega)\,, \\ \sigma &\mapsto E(\sigma)\,, \end{aligned} \tag{3.13}$$

where $E(\sigma)$ is defined as in (3.10) and $s > N/2 + 1$. In the context of optimization, equation (3.12) can be expressed as the minimization of the functional

$$\frac{1}{2}\left\|E - F(\sigma)\right\|^2 .$$

Initially, the conductivity was assumed to belong to $L^\infty(\Omega)$. However, since this space is not reflexive and the resulting power density then only belongs to $L^1(\Omega)$, the treatment of the problem in this setting is not straightforward. Due to Sobolev's embedding theorem [AF03], the Sobolev space $H^s(\Omega)$ embeds compactly into $L^\infty(\Omega)$ for $s > N/2$ and therefore, assuming that $\sigma \in H^s(\Omega)$ for $s > N/2 + 1$, we can apply the regularity results discussed above to transfer the problem into a classical Hilbert space setting.

Analogously to [BNSS13, GS08], the Fréchet derivative of the operator $F$ can be found using the following theorem.

**Theorem 3.3.1** (Paper A, Proposition 3.1)**.** *The operator $F : \mathcal{D}_s(F) \to L^2(\Omega)$ defined by (3.13) is Fréchet differentiable for $s > N/2 + 1$ with*

$$F'(\sigma)h = h\,|\nabla u(\sigma)|^2 + 2\,\sigma \nabla u(\sigma) \cdot \nabla(u'(\sigma)h)\,, \tag{3.14}$$

*where $u'(\sigma)h$ is defined as in Proposition 3.2.6.*

To compute the adjoint of the Fréchet derivative of the operator $F$, we introduce an additional variational problem acting as the embedding adjoint.

**Lemma 3.3.2** (Paper A, Proposition 3.2)**.** *Denote by $E_s : H^s(\Omega) \to L^2(\Omega)$ the embedding operator for $s \geq 0$, i.e., $E_s v = v$ for all $v \in H^s(\Omega)$. Then, for any element $w \in L^2(\Omega)$ the adjoint $E_s^* w$ is given as the unique solution of the variational problem*

$$\langle E_s^* w, v \rangle_{H^s(\Omega)} = \langle w, v \rangle_{L^2(\Omega)} , \qquad \forall\, v \in H^s(\Omega) . \tag{3.15}$$

Finally, the expression for the adjoint is given by the next theorem for $u(\sigma)$ being given as the solution of (3.7), i.e., in the Neumann case.

**Theorem 3.3.3** (Paper A, Theorem 3.3)**.** *Let $F : \mathcal{D}_s(F) \to L^2(\Omega)$ be defined by* (3.13) *with $s > N/2 + 1$. Then for the adjoint of the Fréchet derivative of $F$ there holds*

$$F'(\sigma)^* w = E_s^* \left( w \left| \nabla u(\sigma) \right|^2 + 2 \nabla u(\sigma) \cdot \nabla (Aw) \right) , \tag{3.16}$$

*where $Aw \in V$ is given as the unique solution of the variational problem*

$$\int_\Omega \sigma \nabla (Aw) \cdot \nabla v \, dx = - \int_\Omega \sigma w \nabla u(\sigma) \cdot \nabla v \, dx , \qquad \forall\, v \in V . \tag{3.17}$$

Similarly, for $u(\sigma)$ being given as the solution of (3.5), i.e., in the Dirichlet case, the adjoint of the Fréchet derivative of $F$ is also given by (3.16), where $Aw \in V_0$ is again defined by (3.17), but now for all $v \in V_0$.

Generalizing to the multiple measurement case (for details see Paper A, Section 3.2), the Fréchet derivative is given by

$$F'(\sigma) h := \left\{ h \left| \nabla u_i(\sigma) \right|^2 + 2 \, \sigma \nabla u_i(\sigma) \cdot \nabla (u_i'(\sigma) h) \right\}_{i=1}^{M} , \tag{3.18}$$

and its adjoint is given by

$$F'(\sigma)^* w := \sum_{i=1}^{M} E_s^* \left( w_i \left| \nabla u_i(\sigma) \right|^2 + 2 \, \sigma \nabla u_i(\sigma) \cdot \nabla (A w_i) \right) , \tag{3.19}$$

for $M \in \mathbb{N}$ measurements of the power density denoted by $E_i(\sigma) := \sigma \left| \nabla u_i(\sigma) \right|^2$.

One can also consider the following inner product on $H^s(\Omega)$

$$\langle u, v \rangle_{s,\beta} := \sum_{|\alpha| \leq s} \beta_\alpha \langle \partial^\alpha u, \partial^\alpha v \rangle_{L^2(\Omega)} ,$$

for integers $s$ and a family of positive weights $\{\beta_\alpha\}$, and compute the adjoint of the Fréchet derivative of $F$ with respect to this inner product, which leads

to ${E_s}^*$ being replaced by $E^*_{s,\beta}$, where $E^*_{s,\beta} w \in H^s(\Omega)$ is given as the unique solution of the variational problem

$$\left\langle E^*_{s,\beta} w, v \right\rangle_{s,\beta} = \left\langle w, v \right\rangle_{L^2(\Omega)} , \qquad \forall\, v \in H^s(\Omega) . \tag{3.20}$$

Using this weighted inner product gives us more flexibility in the reconstruction process, as we can put emphasis on different derivatives of the solution.

## 3.4 Full Data Tomography

After providing all necessary theoretical investigations of the problem (3.12), we first reproduce results presented in [BNSS13] using the Levenberg-Marquardt method (2.28). The implementation of the iteration requires a number of steps including assembling and solving a multi-equation variational problem for (2.28), due to the implicit dependence of the Fréchet derivative on the operators $u$ and $F$, and the adjoint of the Fréchet derivative of $F$ on the update $h_k := \sigma^\delta_{k+1} - \sigma^\delta_k$. We denote

$$\begin{aligned}
y_i &:= u_i'(\sigma_k^\delta) h_k , && i = 1, \dots, M , \\
p_i &:= A\, |\nabla u_i(\sigma_k^\delta)|^2\, h_k , && i = 1, \dots, M , \\
q_i &:= A\, \sigma_k^\delta \nabla u_i(\sigma_k^\delta) \cdot \nabla \left( u_i'(\sigma_k^\delta) h_k \right) , && i = 1, \dots, M , \\
z &:= F'(\sigma_k^\delta)^* F'(\sigma_k^\delta) h_k ,
\end{aligned}$$

where $y_i, p_i, q_i \in V_0$, $i = 1, \dots, M$, and $z \in H^s(\Omega)$. Remember that $M$ denotes the number of measurements. The resulting system of $3M + 2$ variational problems, which has to be solved in every iteration step, is given by

$$\begin{aligned}
&\int_\Omega \sigma_k^\delta\, \nabla y_i \cdot \nabla v + h_k \nabla u_i(\sigma_k^\delta) \cdot \nabla v \; dx = 0 , && i = 1, \dots, M , \\
&\int_\Omega \sigma_k^\delta\, \nabla p_i \cdot \nabla v + \sigma_k^\delta\, |\nabla u_i(\sigma_k^\delta)|^2\, h_k \nabla u_i(\sigma_k^\delta) \cdot \nabla v \; dx = 0 , && i = 1, \dots, M , \\
&\int_\Omega \sigma_k^\delta\, \nabla q_i \cdot \nabla v + (\sigma_k^\delta)^2\, (\nabla u_i(\sigma_k^\delta) \cdot \nabla y) \nabla u_i(\sigma_k^\delta) \cdot \nabla v \; dx = 0 , && i = 1, \dots, M , \\
&\sum_{|\alpha| \le s} \beta_\alpha \int_\Omega \partial^\alpha z \cdot \partial^\alpha \tilde{v} \; dx - \sum_{i=1}^M \int_\Omega (h_k |\nabla u_i(\sigma_k^\delta)|^4 + 2\sigma_k^\delta \nabla u_i(\sigma_k^\delta) \cdot \nabla y |\nabla u_i(\sigma_k^\delta)|^2 \\
&+ 2 \nabla u_i(\sigma_k^\delta) \cdot \nabla (p_i + q_i)) \; \tilde{v} \; dx = 0 , \\
&\int_\Omega (z + \alpha h_k) \hat{v} \; dx = \sum_{i=1}^M \int_\Omega F_i'(\sigma_k^\delta)^* (E_i^\delta - F_i(\sigma_k^\delta)) \hat{v} \; dx ,
\end{aligned} \tag{3.21}$$

for all $v \in V_0$ and $\tilde{v}, \hat{v} \in H^s(\Omega)$.

### 3.4.1 Numerical Results

We consider a unit disk domain for the numerical example problem. For the true conductivity we use the phantom depicted in Figure 3.1. It has a uniform background of value 1 as well as three inclusions: a circular inclusion of magnitude 1.2, a crescent shaped inclusion of magnitude 0.5 and a rectangular inclusion of magnitude 1.5.

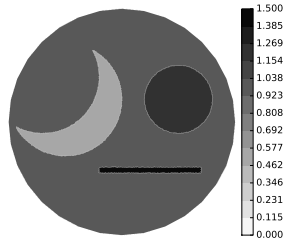


Figure 3.1: Exact conductivity $\sigma^\dagger$.

The discretization, implementation and computation of the involved variational problems was done using Python and the library FEniCS [ABH+15]. Two triangulations, coarse and fine, for discretizing the domain were used. The power density data $E(\sigma^\dagger)$ was created by applying the forward model to $\sigma^\dagger$ using a finer discretization to avoid an inverse crime. The resulting power densities from the boundary potentials

$$g_{D,1} = \sin(\theta)\,, \qquad g_{D,2} = \cos(\theta)\,, \qquad g_{D,3} = (\sin(\theta) - \cos(\theta))/\sqrt{2}\,, \tag{3.22}$$

assigned to the entire boundary are depicted in Figure 3.2.

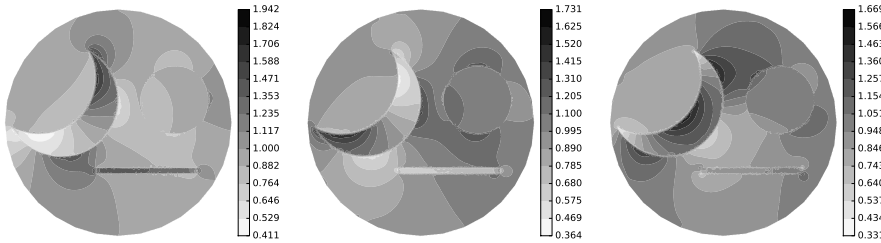


Figure 3.2: Power density derived from the exact conductivity $\sigma^\dagger$ depicted in Figure 3.1 and the boundary potentials $g_{D,i}$, $i = 1, 2, 3$ defined in (3.22).

With an increasing number of measurements, the Levenberg-Marquardt iteration (2.28) slows down due to assembling and solving a larger system of variational problems (3.21), which also becomes computationally costly with a finer discretization. To speed up the computations, we turned our attention to the Kaczmarz idea, which takes advantage of the multi-measurements structure of the problem, and is known as the Levenberg-Marquardt-Kaczmarz method (2.32). The loping version of the iteration requires solving the problem only with one measurement at each iteration step, and thus is expected to be more efficient. Our numerical experiments support this conjecture. Even though it takes more iterations to reach the stopping criteria, method (2.32) requires 1.6 times less computational time than (2.28). For the chosen regularization parameter $\alpha = 1 - \frac{k-1}{k+50}$, the weights $\beta_\alpha = 1, 10^{-3}, 10^{-6}$ for $|\alpha| = 0, 1, 2$, and a random relative noise of 5% in the data, the resulting reconstructions using the iterations (2.28) and (2.32), which terminated after 48 and 116 iterations, respectively, are depicted in Figure 3.3. The iterations are terminated by their

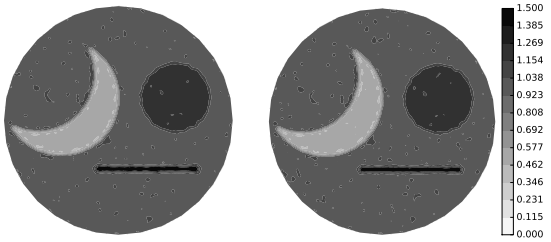


Figure 3.3: Reconstructions of the exact conductivity $\sigma^\dagger$ depicted in Figure 3.1, derived from the three boundary potentials $g_{D,i}$, $i = 1, 2, 3$ defined in (3.22) and 5% relative noise. From left to right: using (2.28), 58 iterations; using (2.32), 116 iterations.

respective stopping rules given by (2.6) and (2.33). The slightly more restrictive rule for (2.32) ensures that all components of the residual vector fall below a predefined level, which is not necessarily the case for (2.28). However, note that if (2.33) is satisfied then (2.6) is satisfied too. The quality of the resulting reconstructions are similar, see Figure 3.4. The Levenberg-Marquardt-Kaczmarz iteration (2.32) is an interesting approach for solving coupled physics problems with multiple measurements since the structure of the problem is exploited there, and it performs numerically faster than the Levenberg-Marquardt iteration (2.28).

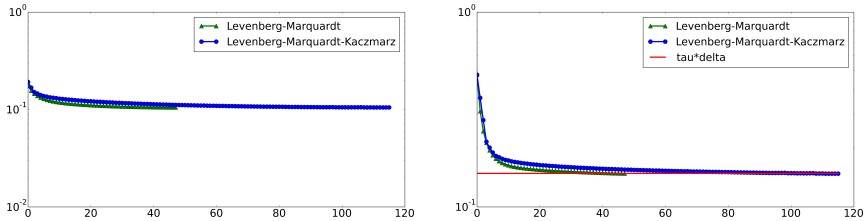


Figure 3.4: From left to right: relative error $\left\|\sigma^\dagger - \sigma_k^\delta\right\| / \left\|\sigma^\dagger\right\|$ and residual $\left\|E^\delta - F(\sigma_k^\delta)\right\|$ of the iterations (2.28) and (2.32).

## 3.5 Limited Angle Tomography

Motivated by the possible application of AET in the detection of breast cancer, we turn our attention to the inverse problem of identifying the conductivity inside a body from internal measurements of the power density acquired using only a part of the boundary for electric acquisition. As in the previous section, we consider the inverse problem (3.12) based on the mathematical model (3.2), but supplied with Neumann boundary conditions (3.4). Here, we focus on the limited angle case, i.e., when measurements are confined to a part of the boundary, which results in incomplete datasets. For this problem, our interest lies in the investigation of qualitative and quantitative aspects of the solution and less in the numerical efficiency of the chosen iterative algorithm. For more details on the topics discussed in this section see Paper A.

### 3.5.1 Numerical Results

Once again we consider a unit disk domain for the numerical example problems. For the true conductivity we use the phantom depicted in Figure 3.5. It has a uniform background of value 1 as well as three inclusions: two circular inclusions of magnitude 1.3 and 2, respectively, and a crescent shaped inclusion of magnitude 1.7, which are slightly smoothed towards their edges with a $C^2$ smooth polynomial. The boundary conditions applied in this case depend on the choice of angle $\alpha$, indicating the available boundary $\Gamma(\alpha)$, which is defined by

$$\Gamma(\alpha) := \{(r,\theta) \in \{1\} \times [0,\alpha]\}\,, \tag{3.23}$$

and satisfy the compatibility condition (3.1), namely

$$g_{N,j}(r,\theta) := \sin\left(\frac{2j\pi\theta}{\alpha}\right)\,, \qquad \forall\,(r,\theta) \in \Gamma(\alpha)\,. \tag{3.24}$$

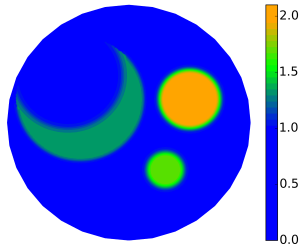


Figure 3.5: Exact conductivity $\sigma^\dagger$.

Reconstructions from simulated data are obtained using a simple Landweber-type gradient method (2.17) with the steepest descent stepsize (2.18). We consider the cases of 25%, 50%, 75%, and 100% available boundary corresponding to the angles $\pi/2$, $\pi$, $3\pi/2$, and $2\pi$, respectively. A decrease of the boundary accessible for measurements directly affects the reconstructions, see Figure 3.6. The smaller the available boundary, the smaller the area in which the conductivity is well reconstructed, the reconstruction being best close to this boundary.

Even though speed is not a consideration for choosing an iterative method for this numerical investigation, we tried the Kaczmarz idea to see how it performs in the limited angle case. As it turns out, iteration (2.25) did not perform well due to its rather restrictive stopping rule (2.26), which checks the residual error measurement-wise, and due to which it takes more iterations and computational work to converge.

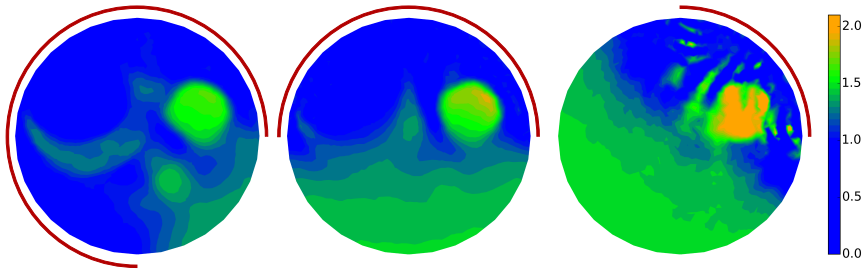


Figure 3.6: Reconstruction of the conductivity $\sigma^\dagger$, Figure 3.5, derived from the boundary data $g_{N,j}$, $j = 1, 2, 3$ defined in (3.24) and various angles in $\Gamma(\alpha)$, and 5% relative noise. From left to right: $\alpha = 3\pi/2$, i.e., 75% available boundary, $H^2_\beta$ adjoint, 10 iterations; $\alpha = \pi$, i.e., 50% available boundary, $H^2_\beta$ adjoint, 38 iterations; $\alpha = \pi/2$, i.e., 25% available boundary, $H^2_\beta$ adjoint, 1000 iterations.

It is well known that for linear problems, the degree of ill-posedness of a problem is directly connected to the SVD of the linear operator [EHN96], a fast decrease of the singular values indicating a strong ill-posedness. In the nonlinear case, the connection between the ill-posedness of $F(x) = y$ and the Fréchet derivative $F'(x)$ is not as strong as one might expect it to be (see for example [Sch02, EKN89]). However, in many cases the connection is strong, as can for example be seen from the assumption

$$\left\|F'(x^\dagger)h\right\|_Y \geq c\,\|h\|_{-a}\,, \qquad \forall\, h \in X\,, \tag{3.25}$$

commonly used for analyzing iterative methods in Hilbert scales [Neu00], where the parameter $a$ effectively measures the degree of ill-posedness of the problem. Furthermore, since almost all methods for solving ill-posed problems rely on the Fréchet derivative of $F$, information about the expectable quality of the reconstruction may be obtained from this Fréchet derivative.

We compute the transfer matrix corresponding to the Fréchet derivative $F'(\sigma^\dagger)$ and its SVD for different limited angle cases and numbers of power density measurements (for more details, see Paper A). First, we look at the singular values and condition numbers of the transfer matrix, which are given in Figure 3.7 and Table 3.8, respectively. In Figure 3.9 we see that different singular vectors carry information about the true conductivity $\sigma^\dagger$ in different areas of the domain.

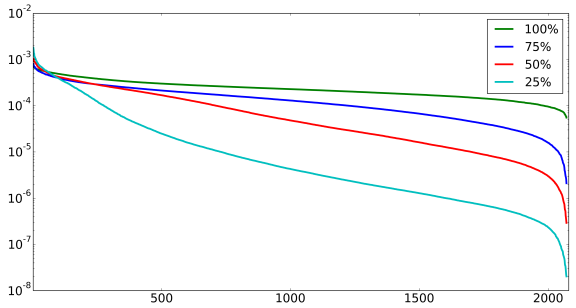


Figure 3.7: Singular values for 100%, 75%, 50% and 25% available boundary with three measurements of the power density.

| Number of measurements | Limited angle, % | | | |
|---|---|---|---|---|
| | 100 | 75 | 50 | 25 |
| 3 | $1.5 \cdot 10^1$ | $3.8 \cdot 10^2$ | $3.6 \cdot 10^3$ | $8.8 \cdot 10^4$ |
| 2 | $1.5 \cdot 10^1$ | $3.7 \cdot 10^2$ | $3.4 \cdot 10^3$ | $8.1 \cdot 10^4$ |
| 1 | $4.6 \cdot 10^3$ | $6.4 \cdot 10^3$ | $1.8 \cdot 10^5$ | $4.5 \cdot 10^6$ |

Table 3.8: Condition numbers of the transfer matrix corresponding to the Fréchet derivative $F'(\sigma^\dagger)$.

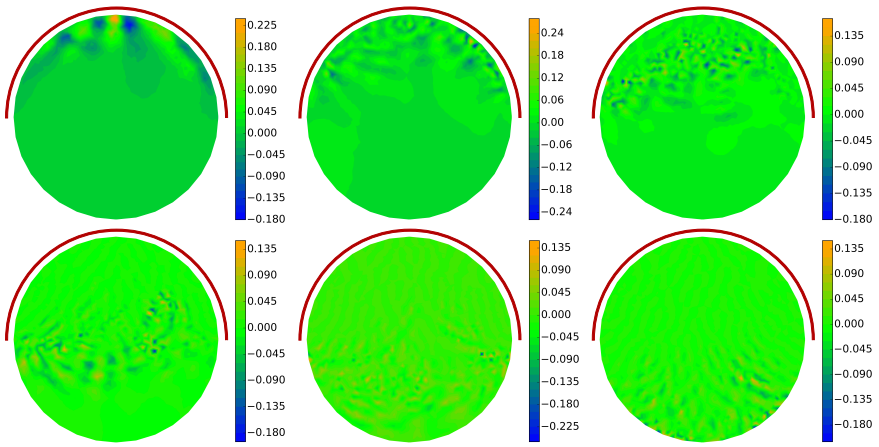


Figure 3.9: Singular vectors of the transfer matrix of $F'(\sigma^\dagger)$, with $\sigma^\dagger$ as in Figure 3.5, and with the boundary functions $g_{N,j}$, $j = 1, 2, 3$ defined in (3.24), and $\alpha = \pi$ in $\Gamma(\alpha)$, i.e., 50% available boundary. From left to right: $v_{10}$, $v_{100}$, $v_{500}$, $v_{1000}$, $v_{1500}$, $v_{2000}$.

From the singular values, Figure 3.7, and the condition numbers, Table 3.8, we observe that the transfer matrix becomes more and more ill-conditioned with decreasing angle and number of measurements, and therefore, we should not expect good reconstructions, especially further away from the accessible boundary. Additionally, we can see that using two measurements instead of one reduces the condition number drastically. However, the third measurement does not reduce the condition number significantly. Therefore, one can expect obtaining reasonable reconstructions with two measurements as well, and with a shorter computational time.

Unfortunately for the reconstruction, the singular vectors in Figure 3.9 containing information about the area close to the inaccessible boundary correspond to small singular values. Since regularization methods have to rely on the singular vectors corresponding to larger singular values for a stable reconstruction, this adds to the explanation of the fact that close to the inaccessible boundary, the conductivity $\sigma^\dagger$ cannot be reconstructed.

Physically, this can be explained by the active interaction of electric and acoustic phenomena inside the tissue or material, i.e., any acoustic phenomenon happens only in presence of an electromagnetic field inside. Thus, if the current is not able to penetrate certain areas of the body, then one cannot expect recording additional internal information there. This can be observed in the reconstructions of the conductivity from different limited angle settings, depicted in Figure 3.6.

# Chapter 4

# Quantitative Elastography

In this chapter, we summarize the main results of Paper B, in which the problem of estimating the Lamé parameters from full internal static displacement field measurements is considered. The main contributions of this paper consist in formulating the problem as a nonlinear operator equation, proving a nonlinearity condition and designing a computational method for solving it. Among the basic steps, the Fréchet derivative and the adjoint of the underlying nonlinear operator are derived for applying iterative regularization methods. The verification of a tangential cone condition guarantees convergence of the iterative regularization methods used for obtaining reconstructions. Finally, some sample reconstructions from numerically simulated displacement field data are presented. All theoretical derivations and proofs were obtained in an infinite dimensional context. In addition to these results from Paper B, this chapter features additional background information on Quantitative Elastography as well as some results of the application of the developed method to an experimental dataset from a physical experiment, for which the resulting reconstructions of the Lamé parameters and other elastic moduli are presented.

## 4.1 Background on Elastography

*Quantitative Elastography* is an imaging modality mapping *biomechanical parameters* of tissues [Doy12]. It goes back to the palpation technique used by doctors and is motivated by the *various stiffnesses* of tissues, which is employed for diagnostics. A physical examination can be an effective method for detecting tumours, where it is accessible to doctors' hands.

Quantitative Elastography may be potentially employed for the detection of breast and prostate cancer, liver cirrhosis, characterization of atherosclerotic plague in hardened coronary vessels and dermatology [MOD+01, WS15]. Distinguishing cancerous anomalies is possible by looking at the biomechanical parameters called *elastic moduli*. It was noticed that a malignant tissue shows a much higher modulus value than a healthy tissue [Doy12]. None of the classical modalities, such as MRI or CT, provide quantitative information about elastic parameters of tissues, which widely vary in magnitude depending on the types of tissues. Although the elastic moduli are well known and classified in material science, along with experimental procedures for acquiring them, which consists in applying a known stress to a sample and measuring the resulting strain, this was not done for biological tissues until recently due to difficulties in measuring. Much of the pioneering work in this area since the 1990s has lead to establishing Quantitative Elastography as a technique allowing to quantify the elastic parameters of tissues [MOD+01, Doy12]. It was proposed to perform Elastography on top of other medical imaging techniques, for example Ultrasound, Optical Coherence Tomography (OCT) and Magnetic Resonance Imaging (MRI), which can provide measurements of *interior data* like the *displacement field* $u$ of the tissue, and then use them to identify the unknown elastic parameters. In this sense, elastography is an example of a coupled physics imaging modality.

The main principles of elastography can be summarized as follows [Doy12, WS15]:

1. Perturb the tissue using some mechanical source.
2. Measure the internal tissue displacements using a suitable ultrasound, magnetic resonance, or optical displacement estimation method.
3. Infer the mechanical properties from the measured mechanical response, using either a simplified or a continuum mechanical model.

Depending on how a boundary excitation is imposed on the sample, three different experimental approaches exist nowadays - quasi-static, harmonic, and transient [Doy12, JM04], see Figure 4.1. We only mention that in the static experiment, the sample is deformed by a slowly varying boundary force. After the experiment is made, the coupled modality provides interior data in the form of the displacement field $u$, which can be space or space-time dependent [WS15]. In order to find the biomechanical parameters, an inverse problem has to be posed and solved, based on one of the proposed models in Quantitative Elastography such as linear elasticity, viscoelasticity or hyperelasticity [Doy12]. In various formulations, such parameters as the Lamé parameters $\lambda$ and $\mu$, the density $\rho$, or the shear wave speed $\frac{\mu}{\rho}$ are sought, given the interior displacement $u$ [Doy12, WS15].

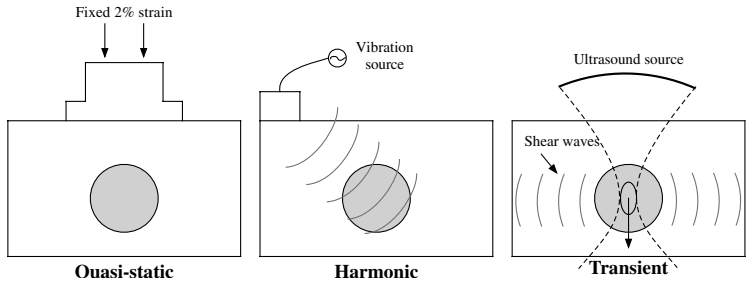


Figure 4.1: Schematic representation of elastography imaging with different excitation types (taken from Doyley, [Doy12]).

There exists a vast amount of literature on identifiability of the Lamé parameters, stability, and different reconstruction methods. See for example [BBIM14, BU12,BU13,BG04,BO07,Doy12,DMB00,FMST06,GBO08,HS97,JKR08,KR16, JMRY03,MR06,OGDB04,OGF03,WS15,LS17] and the references therein. Many of the above works deal with the time-dependent equations of linearized elasticity, since the resulting inverse problem is arguably more stable and better to solve. However, in many applications, including the ones we have in mind in this thesis, no dynamic, i.e., time-dependent displacement field data is available and hence, one has to work with the static elasticity equations. Existence and uniqueness of some inverse problems in Quantitative Elastography were addressed mostly for simple models, for example in [JM04, MY04, BBIM14] for time-dependent interior data. The results obtained there might also be true for problems with static interior data, but to the best of our knowledge no publications are available on this question yet. The stability issue of several problems in Quantitative Elastography was discussed in [WS15], where a stability analysis was done using the general framework for coupled physics problems developed in [Bal14]. The results show stability of separate reconstruction of the shear modulus, the pressure, and the density.

Before introducing a PDE model characterizing the physical phenomenon of Quantitative Elastography, we describe a possible real-world problem which we have in mind. We consider a cylinder shaped object made out of agar with a symmetric, ball shaped inclusion of a different type of agar with different material properties and hence, different Lamé parameters. The object is placed on a surface and a constant downward displacement is applied from the top, while the outer boundary of the object is allowed to move freely. Due to a marker substance being injected into the object beforehand, the resulting displacement field can be measured inside, using a combination of different imaging modalities. Since the object is rotationally symmetric, this also holds for the displacement field, which allows for a relatively high resolution 2D image.

## 4.2 Mathematical Model of Linearized Elasticity

For different variants of excitation in elastography, suitable PDE models are commonly derived from the equations of motion [Doy12, WS15]. Assuming that the tissue which we would like to study is inhomogeneous linear isotropic and that we work with small deformations, the model of *linearized elasticity*, describing the relation between forces and displacements, is valid in this case [WS15]. Hence, quantitative elastography consists in estimating the spatially varying *Lamé parameters* $\lambda, \mu$ from a displacement field measurement $u$ induced by external forces.

First, we introduce the basic notation, which we use throughout this chapter, and recall the basic equations of linearized elasticity.

**Notation.** *$\Omega$ denotes a non-empty, bounded, open and connected set in $\mathbb{R}^N$, $N = 1, 2, 3$, with a Lipschitz continuous boundary $\partial\Omega$, which has two subsets $\Gamma_D$ and $\Gamma_T$, satisfying $\partial\Omega = \overline{\Gamma_D \cup \Gamma_T}$, $\Gamma_D \cap \Gamma_T = \emptyset$ and $\operatorname{meas}(\Gamma_D) > 0$.*

Next, we provide the forward model suitable for the experimental setting discussed above and schematically depicted in Figure 4.2. Given body forces $f$, displacement $g_D$, surface traction $g_T$ and Lamé parameters $\lambda$ and $\mu$, the forward problem of *linearized elasticity* with displacement-traction boundary conditions consists in finding $\tilde{u}$ satisfying

$$\begin{aligned} -\operatorname{div}(\sigma(\tilde{u})) &= f\,, \qquad \text{in } \Omega\,, \\ \tilde{u}\,|_{\Gamma_D} &= g_D\,, \\ \sigma(\tilde{u})\vec{n}\,|_{\Gamma_T} &= g_T\,, \end{aligned} \tag{4.1}$$

where $\vec{n}$ is an outward unit normal vector of $\partial\Omega$ and the *stress tensor* $\sigma$ defining the stress-strain relation in $\Omega$ is defined by

$$\sigma(u) := \lambda \operatorname{div}(u)\, I + 2\mu\, \mathcal{E}(u)\,, \qquad \mathcal{E}(u) := \frac{1}{2}\left(\nabla u + \nabla u^T\right)\,, \tag{4.2}$$

where $I$ is the identity matrix and $\mathcal{E}$ is called the *strain tensor*.

In the following, we only consider weak solutions of (4.1). For this, we make the following:

**Assumption 4.2.1.** *Let $f \in H^{-1}(\Omega)^N$, $g_D \in H^{\frac{1}{2}}(\Gamma_D)^N$, and $g_T \in H^{-\frac{1}{2}}(\Gamma_T)^N$. Furthermore, let $\Phi \in H^1(\Omega)^N$ be such that $\Phi|_{\Gamma_D} = g_D$.*

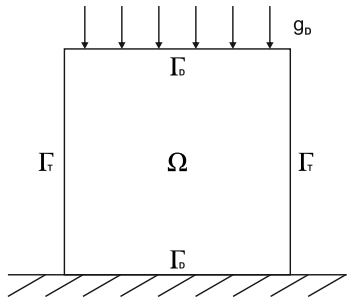


Figure 4.2: Schematic drawing of the domain $\Omega$ with applied displacement $g_D$.

Additionally, we define the space

$$V := H^1_{0,\Gamma_D}(\Omega)^N\,, \qquad \text{where} \qquad H^1_{0,\Gamma_D}(\Omega) := \{u \in H^1(\Omega) \mid u|_{\Gamma_D} = 0\}\,. \tag{4.3}$$

Next, we introduce the linear form

$$l(v) := \langle\, f, v \,\rangle_{H^{-1}(\Omega),H^1(\Omega)} + \langle\, g_T, v \,\rangle_{H^{-\frac{1}{2}}(\Gamma_T),H^{\frac{1}{2}}(\Gamma_T)}\,, \tag{4.4}$$

and the bilinear form

$$a_{\lambda,\mu}(u,v) := \int_\Omega \left(\lambda\, \operatorname{div}(u) \operatorname{div}(v) + 2\mu\, \mathcal{E}(u) : \mathcal{E}(v)\right) dx\,, \tag{4.5}$$

where the expression $\mathcal{E}(u) : \mathcal{E}(v)$ denotes the Frobenius product of the matrices $\mathcal{E}(u)$ and $\mathcal{E}(v)$, which also induces the Frobenius norm $\|\mathcal{E}(u)\|_F := \sqrt{\mathcal{E}(u) : \mathcal{E}(u)}$. For details on the derivation of (4.5) and (4.4) for problem (4.1), see Appendix B.

We define a weak solution of the linearized elasticity problem (4.1) as a function $u \in V$ satisfying the variational problem

$$a_{\lambda,\mu}(u,v) = l(v) - a_{\lambda,\mu}(\Phi, v)\,, \qquad \forall\, v \in V\,. \tag{4.6}$$

Furthermore, we define the set $\mathcal{M}(\underline{\mu})$ of admissible Lamé parameters by

$$\mathcal{M}(\underline{\mu}) := \left\{ (\lambda,\mu) \in L^\infty(\Omega)^2 \,|\, \exists\, 0 < \varepsilon \le \frac{\underline{\mu}\, c_K^2}{N + 2c_K^2} \;:\; \lambda \ge -\varepsilon\,,\; \mu \ge \underline{\mu} - \varepsilon > 0 \right\}.$$

Existence and uniqueness of solutions is guaranteed by Proposition 4.2.1, which was proven using the Lax-Milgram Lemma.

**Proposition 4.2.1** (Paper B, Theorem 2.1)**.** *Let the Assumption 4.2.1 hold and assume that the Lamé parameters* $(\lambda, \mu) \in \mathcal{M}(\underline{\mu})$ *for some* $\underline{\mu} > 0$*. Then there exists a unique weak solution* $u \in V$ *of* (4.6)*. Moreover, there exists a constant* $c_{LM} > 0$ *such that*

$$\|u\|_{H^1(\Omega)} \leq c_{LM} \Big( \|f\|_{H^{-1}(\Omega)} + c_T \|g_T\|_{H^{-\frac{1}{2}}(\Gamma_T)} + \Big( N \|\lambda\|_{L^\infty(\Omega)} + 2 \|\mu\|_{L^\infty(\Omega)} \Big) \|\Phi\|_{H^1(\Omega)} \Big) .$$

Since it is an elliptic problem, many regularity results are available for linearized elasticity, which can for example be found in [Cia94, ADN59, Nec11, Gri92, Gri11, LM12, GT98, Val13]. In summary, for pure displacement or traction problems, full $H^2(\Omega)$ regularity of the solution can be obtained if both the data and the boundary of the domain $\Omega$ are smooth enough. This also holds for displacement-traction problems, given that $\bar{\Gamma}_D \cap \bar{\Gamma}_T = \emptyset$. If this is not the case, then still interior regularity in open subsets $\Omega'$ of $\Omega$ with $\bar{\Omega}' \subset \Omega$ can be obtained. However, at points of intersection of $\bar{\Gamma}_D$ and $\bar{\Gamma}_T$, regularity can be lost, which also often happens in corners of the domain $\Omega$, even if the boundary condition does not change its type there. In the experiment described above, we look at the 2D cross-sections of the sample, which is a rectangular domain with both displacement and traction conditions assigned to the two opposite edges of the domain. In this case, interior $H^2(\Omega)$ regularity holds and in addition, full $H^2(\Omega)$ regularity for a connected homogenized problem was proven in the Appendix of Paper B.

## 4.3 The Inverse Problem

In this section, we provide essential theoretical results for constructing a computational method later on. After considering the forward problem of linearized elasticity, we turn to the inverse problem of identifying the Lamé parameters $\lambda, \mu$ from static displacement field measurements $u$. For *dynamic* measurement data of the displacement field $u$, similar investigation have been performed in [LS17, KR16]. More precisely, we face the following

**Problem.** *Let Assumption 4.2.1 hold and let* $u^\delta \in L^2(\Omega)^N$ *be a measurement of the true displacement field* $u$ *satisfying*

$$\left\| u - u^\delta \right\|_{L^2(\Omega)} \leq \delta \,, \tag{4.7}$$

*where* $\delta \geq 0$ *is the noise level. Given the model of linearized elasticity* (4.1) *in the weak form* (4.6)*, the problem is to find the Lamé parameters* $\lambda, \mu$*.*

This problem can be formulated as the solution of the nonlinear operator equation

$$F(\lambda, \mu) = u \,, \tag{4.8}$$

with the operator

$$\begin{aligned} F : \mathcal{D}_s(F) := \left\{ (\lambda, \mu) \in H^s(\Omega)^2 \mid \lambda \geq 0 \,,\, \mu \geq \underline{\mu} > 0 \right\} \to L^2(\Omega)^N \,, \\ (\lambda, \mu) \mapsto u(\lambda, \mu) \,, \end{aligned} \tag{4.9}$$

which is also called *parameter-to-solution map*, where $u(\lambda, \mu)$ is the solution of (4.6) and $s > N/2$. In the context of optimization, equation (4.8) can be expressed as the minimization of the functional

$$\frac{1}{2} \left\| u - F(\lambda, \mu) \right\|^2 .$$

Originally, the Lamé parameters were assumed to belong to $L^\infty(\Omega)$. However, this space is not reflexive, which makes the analysis of the resulting problem not straightforward. Due to Sobolev's embedding theorem [AF03], the Sobolev space $H^s(\Omega)$ embeds compactly into $L^\infty(\Omega)$ for $s > N/2$ and hence, assuming that $(\lambda, \mu) \in H^s(\Omega)$, we can treat the problem in the classical framework of inverse problems in Hilbert spaces [EHN96].

In Paper B, we introduced the auxiliary operator $\tilde{A}_{\lambda,\mu}$, connected to the bilinear form $a_{\lambda,\mu}$, and defined by

$$\begin{aligned} \tilde{A}_{\lambda,\mu} : \, H^1(\Omega)^N \to V^* \,, \\ \tilde{v} \mapsto (v \mapsto a_{\lambda,\mu}(\tilde{v}, v)) \,, \end{aligned} \tag{4.10}$$

and its restriction to $V$, i.e., $A := \tilde{A}|_V$, where $V^*$ is the dual space of $V$. Important properties of the operators $\tilde{A}_{\lambda,\mu}$ and $A_{\lambda,\mu}$ such as boundedness and linearity, as well as continuous invertability of $A_{\lambda,\mu}$ hold (Paper B, Proposition 3.1). The operator $F$ can be written in the alternative form

$$F(\lambda, \mu) = A^{-1}_{\lambda,\mu} \left( l - \tilde{A}_{\lambda,\mu} \Phi \right) \,, \tag{4.11}$$

and it is shown to be continuous.

The Fréchet derivative of the operator $F$ can be found from (4.11) using results of the following theorem.

**Theorem 4.3.1** (Paper B, Theorem 3.2)**.** *The operator $F$ defined by* (4.11) *and considered as an operator from $\mathcal{M}(\underline{\mu}) \to L^2(\Omega)^N$ for some $\underline{\mu} > 0$ is Fréchet differentiable for all $(\lambda, \mu) \in \mathcal{D}(F)$ with*

$$F'(\lambda, \mu)(h_\lambda, h_\mu) = -A^{-1}_{\lambda,\mu} \left( A_{h_\lambda, h_\mu} u(\lambda, \mu) + \tilde{A}_{h_\lambda, h_\mu} \Phi \right) . \tag{4.12}$$

To compute the adjoint of the Fréchet derivative of the operator $F$, the two linear operators $T : L^2(\Omega)^N \to V^*$ and $E_s : L^1(\Omega) \to H^s(\Omega)$, defined by

$$Tw := \left( v \mapsto \int_\Omega w \cdot v \, dx \right) , \tag{4.13}$$

and

$$\langle E_s u, v \rangle_{H^s(\Omega)} = \int_\Omega uv \, dx , \qquad \forall v \in H^s(\Omega) , \tag{4.14}$$

were introduced. Finally, the expression for the adjoint is given by

**Theorem 4.3.2** (Paper B, Theorem 3.4)**.** *Let $F : \mathcal{D}_s(F) \to L^2(\Omega)^2$ with $\mathcal{D}_s(F)$ for some $s > N/2$. Then the adjoint of the Fréchet derivative of $F$ is given by*

$$F'(\lambda,\mu)^* w = \begin{pmatrix} E_s \left( \operatorname{div} \left( u(\lambda,\mu) + \Phi \right) \operatorname{div} \left( -A_{\lambda,\mu}^{-1} T w \right) \right) \\ E_s \left( 2\,\mathcal{E} \left( u(\lambda,\mu) + \Phi \right) : \mathcal{E} \left( -A_{\lambda,\mu}^{-1} T w \right) \right) \end{pmatrix}^T , \tag{4.15}$$

*where $T$ and $E_s$ are defined by* (4.13) *and* (4.14)*, respectively.*

The main theoretical result of the paper is the verification of a *tangential cone condition*, which guarantees convergence of many iterative regularization methods. Assuming that in many physical settings the composition of a sample and hence, the Lamé parameters $\lambda, \mu$ are known in a small neighbourhood of the boundary, they have to be determined only on the remaining part. In this case the inverse problem can be reformulated and a version of the tangential cone condition (2.12) for the operator $F_c$, defined by $F_c(\lambda,\mu) := F(\lambda_b + \lambda, \mu_b + \mu)$ for compactly supported $\lambda, \mu$ and background functions $\lambda_b, \mu_b$ (for details, see Paper B), can be shown.

The next theorem shows a version of a tangential cone condition under a restriction on the Lamé parameters, which is then used for proving a tangential cone condition for the operator $F_c$ in the subsequent corollary, which in turn implies that (2.13) is valid (see Paper B for details).

**Theorem 4.3.3** (Paper B, Theorem 3.5)**.** *Let $F : \mathcal{D}_s(F) \to L^2(\Omega)^2$ for some $s > N/2 + 1$ and let $\Omega_1 \subset \Omega$ be a bounded, open, connected Lipschitz domain with $\bar{\Omega}_1 \Subset \Omega$. Then for each $(\lambda,\mu) \in \mathcal{D}_s(F)$ there exists a constant $c_{NL} = c_{NL}(\lambda,\mu,\Omega_1,\Omega) > 0$ such that for all $(\bar{\lambda},\bar{\mu}) \in \mathcal{D}_s(F)$ satisfying $(\lambda,\mu) = (\bar{\lambda},\bar{\mu})$ on $\Omega \setminus \Omega_1$ and $(\lambda,\mu) = (\bar{\lambda},\bar{\mu})$ on $\partial\Omega_1$ there holds*

$$\begin{aligned} &\left\| F(\lambda,\mu) - F(\bar{\lambda},\bar{\mu}) - F'(\lambda,\mu)((\lambda,\mu) - (\bar{\lambda},\bar{\mu})) \right\|_{L^2(\Omega)} \\ &\qquad \le c_{NL} \left\| (\bar{\lambda} - \lambda, \bar{\mu} - \mu) \right\|_{W^{1,\infty}(\Omega_1)} \left\| F(\lambda,\mu) - F(\bar{\lambda},\bar{\mu}) \right\|_{L^2(\Omega)} . \end{aligned} \tag{4.16}$$

**Corollary 4.3.4** (Paper B, Corollary 3.6). *Let* $F_c : \mathcal{D}_s(F_c) \to L^2(\Omega)^2$ *for some* $s > N/2 + 1$. *Then for each* $(\lambda, \mu) \in \mathcal{D}_s(F_c)$ *there exists a constant* $c_{NL} = c_{NL}(\lambda, \mu, \Omega_1, \Omega) > 0$ *such that for all* $(\bar{\lambda}, \bar{\mu}) \in \mathcal{D}_s(F_c)$ *there holds*

$$\begin{aligned} &\left\| F_c(\lambda,\mu) - F_c(\bar{\lambda},\bar{\mu}) - F_c'(\lambda,\mu)((\lambda,\mu)-(\bar{\lambda},\bar{\mu})) \right\|_{L^2(\Omega)} \\ &\qquad \leq c_{NL} \left\| (\bar{\lambda}-\lambda, \bar{\mu}-\mu) \right\|_{W^{1,\infty}(\Omega_1)} \left\| F_c(\lambda,\mu) - F_c(\bar{\lambda},\bar{\mu}) \right\|_{L^2(\Omega)} . \end{aligned} \tag{4.17}$$

Condition (4.17) is already strong enough to prove convergence of Landweber iteration for the operator $F_c$ to a solution $(\lambda^\dagger, \mu^\dagger)$, given that the initial guess $(\lambda_0, \mu_0)$ is chosen close enough to $(\lambda^\dagger, \mu^\dagger)$ [HNS95,KNS08]. If the constant $c_{NL}$ is bounded in terms of the Lamé parameters, then the original, strong nonlinearity (2.9) holds. Note furthermore that in Paper B also a source condition for the problem was investigated.

It is worth mentioning once again that local convergence of the employed iteration guarantees stably obtaining numerical solutions of the inverse problem, which is a crucial point in dealing with this type of problems. Furthermore, the above observations on the operator $F_c$ hold independently of the boundary condition, i.e., both for pure displacement and displacement-traction boundary conditions (see Paper B, Theorem 3.5, Corollary 3.6 and Theorem 3.7).

### 4.3.1 Numerical Results

After providing the necessary theoretical investigation on the problem (4.8), we use the modified iteration (2.21) based on nonlinear Landweber iteration and on Nesterov's acceleration strategy for reconstructing the Lamé parameters. Landweber iteration is known for converging quite slowly, but it remains an attractive regularization method because of the fact that it is easy to implement and a comprehensive theoretical analysis is available for it. Additionally, as was noted in Section 2.2.4, Landweber iteration can be easily speeded up using Nesterov's acceleration strategy.

As in the general setting described at the beginning of this section, a rectangular domain was considered for the numerical example problem. For the displacement-traction boundary conditions, on $\Gamma_T$, corresponding to the sides of the object, a zero traction condition was set, i.e., $g_T = 0$ on the sides of the domain. On the bottom, the object was fixed, i.e., $g_D = 0$ on the bottom part of $\Gamma_D$, and a constant displacement was applied from above, i.e., $g_D = c_P = \text{const}$ on the top part of $\Gamma_D$.

Initially, the accelerated Landweber iteration was tested with the different step-

sizes (2.18), (2.19), and (2.20) to find the most suitable one, and terminated using the discrepancy principle (2.6) together with $\tau = 1$. We looked at a test with simple exact Lamé parameters, where only $\mu^\dagger$ has a smooth inclusion inside, see Figure 4.3.

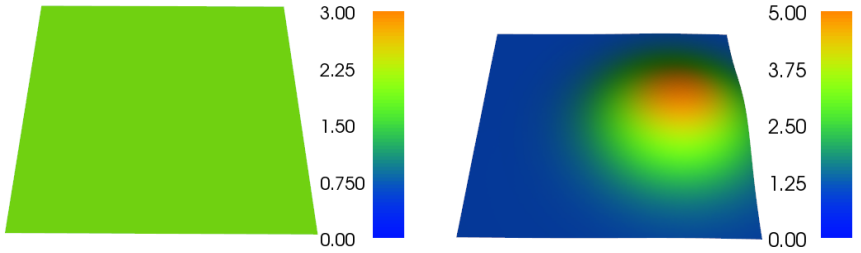


Figure 4.3: Exact Lamé parameters $(\lambda^\dagger, \mu^\dagger)$.

The reconstructions, obtained using the operator $F$ and displacement data corrupted with 1% relative noise (see Appendix A), are depicted in Figure 4.4 for the stepsize (2.18) and (2.20).

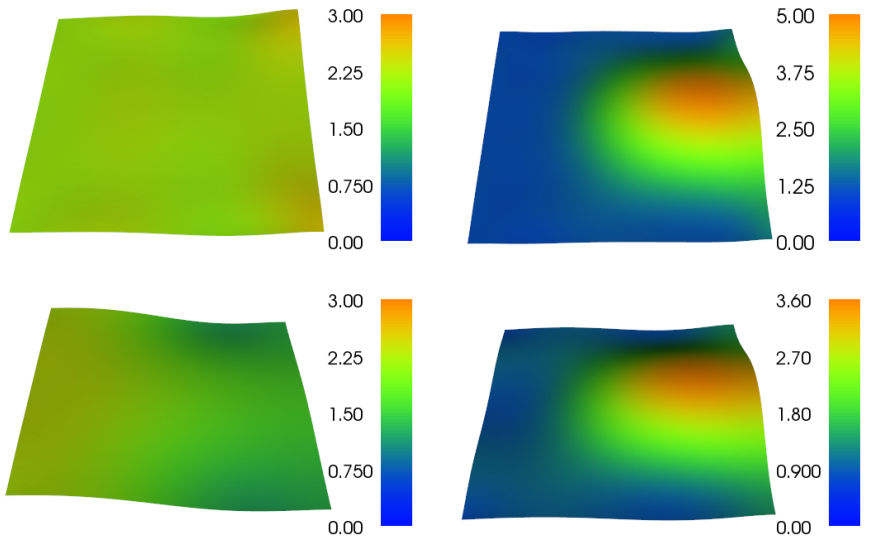


Figure 4.4: Reconstructions of the Lamé parameters $(\lambda^\dagger, \mu^\dagger)$ depicted in Figure 4.3 - Displacement-Traction boundary conditions - operator $F$ using stepsizes (2.18) (top) and (2.20) (bottom).

The minimal error stepsize (2.19) was left out due to its bad performance and mediocre reconstruction of the inclusion in the Lamé parameter $\mu^\dagger$. These experiments showed that the steepest descent stepsize (2.18) performs best, and that it showed faster convergence than (2.19) and (2.20), which can be seen in the development of the relative errors depicted in Figure 4.5.

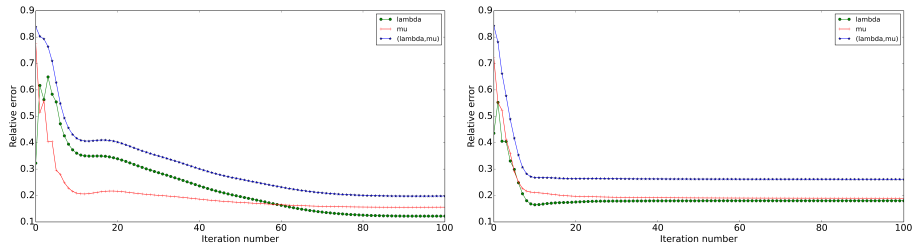


Figure 4.5: Relative errors of the accelerated Landweber iteration with stepsizes (2.18) (left) and (2.20) (right)

In Paper B, reconstructions are obtained from various simulated displacement field data for different Lamé parameters, imitating physical values, using both the operators $F$ and $F_c$. All data have a relative noise of 0.5% (see Appendix A) added to simulate noisy data. One example of the exact Lamé parameters and the simulated displacement field derived from them are depicted in Figures 4.6 and 4.7, respectively. The resulting reconstructions using stepsize (2.18), obtained after 921 iterations, are depicted in Figure 4.8.

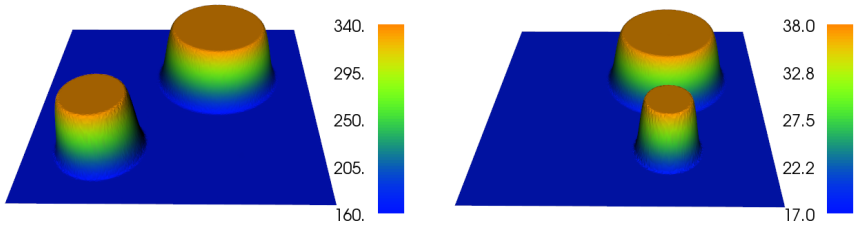


Figure 4.6: Exact Lamé parameters $(\lambda^\dagger, \mu^\dagger)$, in kPa.

In general, the operator $F_c$ used in the iterative regularization methods for estimating the Lamé parameters leads to better reconstructions than the operator $F$. This can be explained by the fact that we provide information on the Lamé parameters in an area around the boundary and that the nonlinearity condition holds for the operator $F_c$.

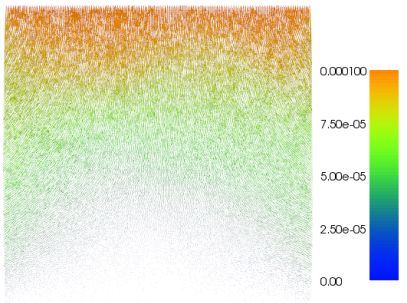


Figure 4.7: Displacement field $u$ corresponding to the Lamé parameters $(\lambda^\dagger, \mu^\dagger)$ depicted in Figure 4.6.

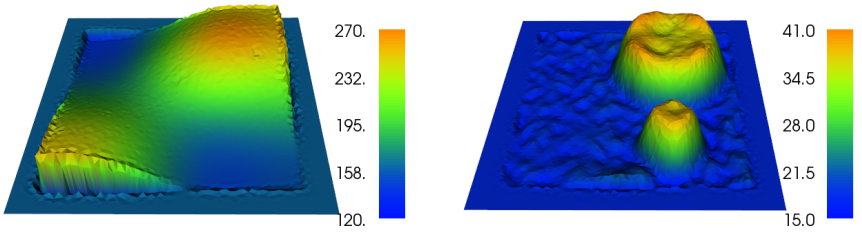


Figure 4.8: Reconstructions of the Lamé parameters $(\lambda^\dagger, \mu^\dagger)$ depicted in Figure 4.6, in kPa - Displacement-Traction boundary conditions - operator $F_c$.

Finally, we make some observations concerning the reconstructions obtained using the designed computational method. The numerical examples show that the Lamé parameter $\mu^\dagger$ is typically nicely reconstructed in shape, value and location. Even though the reconstructions of $\lambda^\dagger$ do not display the same shape as the exact parameter, some information about the value and the location of its inclusions can be obtained. The problem exhibits a smaller sensitivity to changes in $\lambda$ than in $\mu$.

## 4.4 Application in Medicine - Experimental Data

In this section, we present a part of a joint work with the University of Vienna and the Medical University of Vienna, where we are interested in quantitatively estimating the elastic parameters of phantom samples from physical experiments carried out at the facilities of the Center for Medical Physics and Biomedical Engineering at the Medical University of Vienna. For this, we improve and apply the computational method which we designed and tested for simulated data in the previous section. Here, we show how it performs when applied to experimental data and present reconstructions of the Lamé parameters. This is a part of an ongoing work together with Julian Schmidt (University of Vienna, Medical University of Vienna), Prof. Otmar Scherzer (University of Vienna), Prof. Wolfgang Drexler (Medical University of Vienna) and Zhe Chen (Medical University of Vienna). The data were acquired by Julian Schmidt.

### 4.4.1 Experimental Setting

First, we describe the experimental setting and how the data are obtained. In this work, Optical Coherence Tomography (OCT) is combined with Photoacoustic Tomography (PAT) to produce the displacement field measurements, which are then used for quantitative estimates of the material parameters of a sample. Combined together, OCT and PAT take advantage of absorption and scattering effects in tissues, thus scanning the object in two regimes, such that different parts of the tissue are 'visible' either using light or acoustic waves.

The experimental procedure includes the following steps and is schematically depicted in Figure 4.9:

- A cylindrical sample with a spherical inclusion is prepared from agarose gels of different stiffnesses. The ink coloured inclusion is visible using PAT, while the surrounding background with $< 1‰$ Titanium dioxide is visible using OCT. The values for the Young's modulus $E$ are derived using the empirical formula $E = 0.349C^{1.87}$ [HBIK97].
- The sample is imaged before and after compression by a multi-modal PAT/OCT System.
- The sample is coordinate transformed into 2D radial cross-sections.
- A 2D vectorial displacement map is derived using a modified version of the available Optical Flow code [SRB10].
- The biomechanical parameters are recovered from the derived displacement map and can be compared to the ground truth.

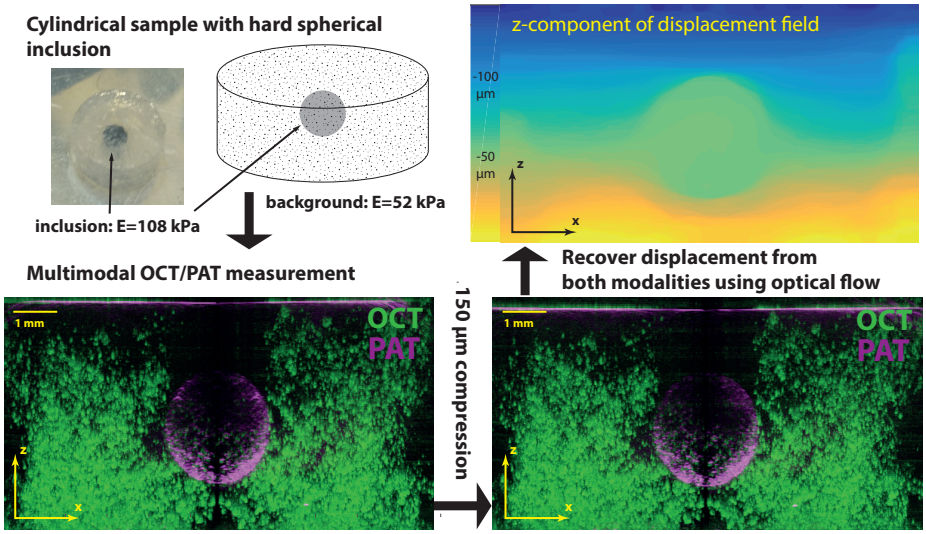


Figure 4.9: Workflow of the experimental procedure - from phantom measurement to vectorial displacement (courtesy of Julian Schmidt).

Furthermore, we briefly discuss the simplified concept of the soft tissues to explain the elastic parameters we are interested in. In isotropic materials, the Young's modulus $E$ is defined as the proportionality constant describing the amount of longitudinal deformation (strain) that happens in a given material in response to an applied longitudinal force (stress) [MOD$^+$01]. Another important physical property is the first Lamé parameter also known as the shear modulus $\mu$, which is given by the relation of transverse strain to stress. This parameter is especially interesting for diagnostics as well as Young's modulus $E$. Related to them, the Poisson's ratio $\nu$ is the ratio of transverse contraction per unit width divided by longitudinal extension per unit length [MOD$^+$01]. All parameters are associated with each other - one of them can be calculated by conversion formulas from the other two. The value of Poisson's ratio for soft tissues varies in the range of $0.490 - 0.499$ [MOD$^+$01]. The Young's modulus and shear modulus in this case are related by $E = 3\mu$. The agarose gel used for preparing the sample is well suited for mimicking soft tissues of the human body.

### 4.4.2 Numerical Results

Before testing experimental data for each sample, the boundary locations and geometry are extracted and a discretization is made for the rectangular domain

approximating the sample geometry. We used grids with approximately 25000 vertices. The given datasets are interpolated to the grid and scaled. Then the problem is solved starting from a given initial guess. Since there is no explicit rule for stopping the iteration in case of experimental data as the noise level is not known and the discrepancy principle can not be employed, we have to terminate the computations after a certain number of iterations, usually chosen experimentally. One reconstruction of the Lamé parameters from one of the experimental datasets is depicted in Figure 4.10. The compression applied to the sample in this experiment is 150 microns.

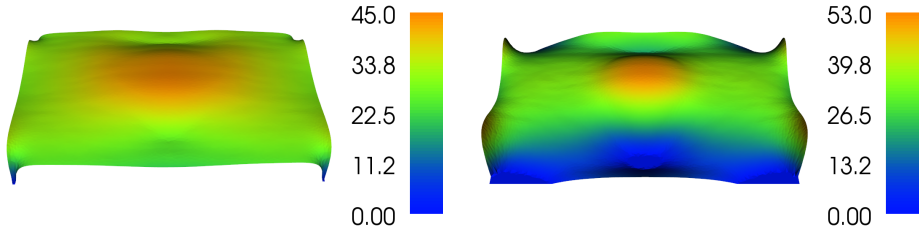


Figure 4.10: Reconstructed Lamé parameters $\lambda, \mu$ from the experiment on the sample depicted in Figure 4.9 - operator $F$.

Two other physical parameters are also interesting for diagnostics, namely the Young's modulus $E$ and the Poisson's ratio $\nu$. For our problem, they can be calculated from the Lamé parameters $\lambda, \mu$ by the conversion formulae

$$E = \frac{\mu\,(3\lambda + 2\mu)}{\lambda + \mu}\,, \qquad \nu = \frac{\lambda}{2\,(\lambda + \mu)}\,,$$

which is applicable in the isotropic compressible case. The resulting parameters are depicted in Figure 4.11.

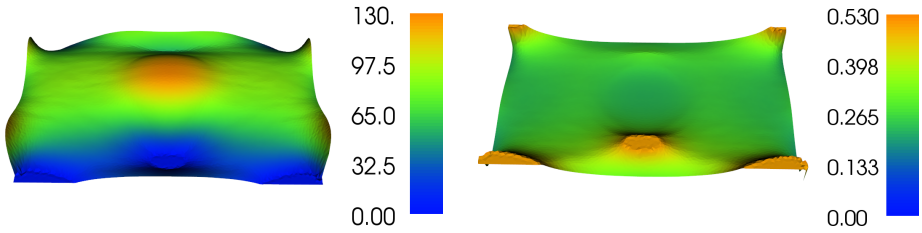


Figure 4.11: Young's modulus (left) and Poisson's ratio (right), derived from the reconstruction of the Lamé parameters depicted in Figure 4.10.

An empirical estimation of Young's modulus from the ground truth gives 108.0

kPa for the ball inclusion and 51.9 kPa for the background. The calculated mean values of Young's modulus from the reconstruction are 106.0 kPa for the inclusion and 61.0 kPa for the background.

The estimation of the Lamé parameters from experimental data of the displacement field fits well to our observation from the previous section. As expected, the Lamé parameter $\mu$ is typically nicely reconstructed in value and location. The reconstructions of $\lambda$ display some information about the value and the location of the inclusion, even though one cannot expect perfect reconstructions there as it is not practically feasible. Nevertheless, the Young's modulus computed from both parameters $\lambda$ and $\mu$ using the conversion formula is reasonably well estimated and matches the expected values, which were calculated empirically from the prepared sample. Reconstruction results using the operator $F_c$ were left out in this section since they did not lead to any significant improvement of the reconstruction quality for the experimental data compared to using the operator $F$.

Note that the reconstructions exhibit some artefact below the spherical inclusion, caused by a lack of data in this area, which can be explained by the imaging setting. The acoustic wave coming from PAT is absorbed by the inclusion, while the light from OCT does not penetrate deep into the sample, Figure 4.9, which leads to incompleteness of the data.

Finally, it is worth mentioning that the application of the algorithm to the experimental dataset is sensitive to details. Proper fitting of the sample's geometry and boundaries is an important part for interpolating the displacement field to the discretized domain, because the scanner area is typically larger than the size of the sample. Moreover, the method requires assigning exact boundary conditions.

# Chapter 5

# Conclusions and Outlook

This thesis dealt with two important tomography problems based on hybrid data from coupled physics phenomena emerging in Acousto-Electrical Tomography and Quantitative Elastography. These methods were motivated by their ability to resolve large variations in physical parameters and to obtain high contrast and high resolution reconstructions.

The first problem, considered in Paper A, dealt with a problem from Electrical Impedance Tomography with hybrid data. We formulated the nonlinear inverse problem of estimating a spatially varying conductivity $\sigma$ from measurements of the power density resulting from different prescribed boundary currents or potentials in an infinite dimensional setting and presented various numerical results, focusing especially on the limited angle case. Our main goal was to theoretically analyse the problem within the framework of nonlinear inverse problems and to construct a robust computational method for solving it. Numerical examples for fully available measurements of the power density confirm that using internal data allows to estimate the conductivity reasonably well. In other words, combining EIT and ultrasound is advantageous since they can produce images of both a high contrast and a high resolution. Additionally, we made some observations on the limited angle case for the hybrid imaging problem. In this case, one is able to obtain a good reconstruction mainly in areas close to the accessible measurement boundary, since the power density carries information mainly in the area penetrated by the electric current. Through a numerical ill-posedness quantification, we were able to establish a close connection between the reconstruction quality and the SVD of the Fréchet derivative of $F$. The obtained results shed some light on the influence of limited angle data in hybrid tomography, clearly illustrating the possibilities and limitations of those methods in numerical practice.

The second problem, which was considered in Paper B, dealt with the identification of the Lamé parameters from given static displacement field measurements. We proposed an operator formulation of the underlying nonlinear inverse problem and proved an important tangential cone condition which guarantees convergence of the Landweber type gradient method used to numerically solve the problem later on. Furthermore, we made some observations concerning reconstructions obtained using the designed computational method. The numerical examples show that the Lamé parameter $\mu^\dagger$ is typically nicely reconstructed in shape, value and location. Even though the reconstructions of $\lambda^\dagger$ do not display the same shape as the exact parameter, some information about the value and the location of the inclusion can be obtained. The problem exhibits a smaller sensitivity to changes in $\lambda$ than in $\mu$. In general, the reconstructions of the Lamé parameters are very promising. Furthermore, we applied the developed algorithm to an experimental dataset obtained from a physical experiment. The results allowed us to obtain information on the Lamé parameters of the physical sample and thus show that this method is applicable in practice as well.

It would be interesting to extend the work presented in this thesis by:

- Supporting the numerical results of Paper A by establishing theoretical results to quantify the ill-posedness of the problem, for example by deriving an analytical SVD of the Fréchet derivative.
- Proving a nonlinearity condition for the operator considered in the inverse problem in Paper A, which would guarantee convergence of iterative solution methods.
- Establishing results on the identifiability of the conductivity and stability in the limited angle case considered in Paper A.
- Instead of only treating pure Dirichlet or Neumann boundary conditions in the AET problem, treating mixed boundary conditions with an inaccessible Neumann sub-boundary.
- Proving a uniqueness result for the elasticity problem. Furthermore, the problem of identifying the Lamé parameters from the time-dependent elasticity equations could become useful for the discussed medical application.
- In case of larger deformations, the equations of linearized elasticity are no longer the right model to apply, and therefore, using different PDE models could become necessary. Extending the analysis of Paper B to those models is therefore desirable.
- The theoretical and numerical results of Paper B have direct applications in medical imaging. Hence, increasing the quality of the reconstructions and creating a robust and efficient software package is therefore another possible extension of the PhD work.

# Appendices

## A Adding Noise to Data

Let $y$ be precise data. Usually in numerical examples, one wants to add noise to the data such that either

$$\left\|y^\delta - y\right\| = \delta\,, \tag{1}$$

where $\delta$ is a given absolute noise level, or

$$\frac{\left\|y^\delta - y\right\|}{\|y\|} = \delta^{rel}\,, \tag{2}$$

where $\delta^{rel}$ is a given relative noise level. This can be done by taking

$$y^\delta = y + c\hat{\delta}\,, \tag{3}$$

where $c$ is a scalar and $\hat{\delta}$ is a randomly selected noise function. In order to conform with (2), the factor $c$ has to be chosen as

$$c = \delta^{rel}\frac{\|y\|}{\left\|\hat{\delta}\right\|}\,.$$

This means that

$$y^\delta = y + \delta^{rel}\,\|y\|\,\frac{\hat{\delta}}{\left\|\hat{\delta}\right\|}\,.$$

Obviously, with this choice one has (1) with $\delta = \delta^{rel}\,\|y\|$.

# B The Variational Formulation of Linearized Elasticity

For the sake of completeness, we derive the variational formulation for the forward problem of linearized elasticity (see for example also [Cia94, JL12]). Multiplying a homogenized version of (4.1) by a test function $v \in V$ and integrating over $\Omega$, we get

$$-\int_\Omega \operatorname{div}(\sigma(u)) \cdot v \, dx = \int_\Omega f \cdot v \, dx + \int_\Omega \operatorname{div}(\sigma(\Phi)) \cdot v \, dx \,. \tag{4}$$

Using integration by parts, boundary conditions, the fact that the Frobenius product $S : K = S : K^T$ for a symmetric matrix $S$, and some algebraic transformations, we get

$$\begin{aligned}
-\int_\Omega \operatorname{div}(\sigma(u)) \cdot v \, dx &= \int_\Omega \sigma(u) : \nabla v \, dx - \int_{\partial\Omega} (\sigma(u)\vec{n}) \cdot v \, dS \\
&= \int_\Omega \sigma(u) : \nabla v \, dx - \int_{\Gamma_T} (g_T - \sigma(\Phi)\vec{n}) \cdot v \, dS \\
&= \int_\Omega \sigma(u) : \tfrac{1}{2}(\nabla v + \nabla v^T) \, dx - \int_{\Gamma_T} (g_T - \sigma(\Phi)\vec{n}) \cdot v \, dS \\
&= \int_\Omega \sigma(u) : \mathcal{E}(v) \; dx - \int_{\Gamma_T} (g_T - \sigma(\Phi)\vec{n}) \cdot v \, dS \\
&= \int_\Omega \lambda \operatorname{div}(u) \operatorname{div}(v) + 2\mu \, \mathcal{E}(u) : \mathcal{E}(v) \; dx - \int_{\Gamma_T} (g_T - \sigma(\Phi)\vec{n}) \cdot v \, dS \,,
\end{aligned}$$

and, analogously,

$$\begin{aligned}
\int_\Omega \operatorname{div}(\sigma(\Phi)) \cdot v \, dx &= -\int_\Omega \sigma(\Phi) : \nabla v \, dx + \int_{\partial\Omega} (\sigma(\Phi)\vec{n}) \cdot v \, dS \\
&= -\int_\Omega \lambda \operatorname{div}(\Phi) \operatorname{div}(v) + 2\mu \, \mathcal{E}(\Phi) : \mathcal{E}(v) \; dx + \int_{\Gamma_T} (\sigma(\Phi)\vec{n}) \cdot v \, dS \,.
\end{aligned}$$

Hence, equation (4) is equivalent to

$$\begin{aligned}
&\int_\Omega \lambda \operatorname{div}(u) \operatorname{div}(v) + 2\mu \, \mathcal{E}(u) : \mathcal{E}(v) \; dx \\
&\quad = \int_\Omega f \cdot v \, dx + \int_{\Gamma_T} g_T \cdot v \, dS - \int_\Omega \lambda \operatorname{div}(\Phi) \operatorname{div}(v) + 2\mu \, \mathcal{E}(\Phi) : \mathcal{E}(v) \; dx \,.
\end{aligned}$$

This motivates the choice (4.5) for the bilinear form $a_{\lambda,\mu}$ and (4.4) for the linear form $l$.

# C Numerical Solution of the Variational Problem of AET with Neumann Boundary Conditions

To numerically implement (3.7) an equivalent variational problem is solved: Find $(u, c) \in H^1(\Omega) \times \mathbb{R}$ such that

$$a_\sigma(u, v) + c \int_\Omega v \, dx + d \int_\Omega u \, dx = l(v)\,, \qquad \forall\, (v, d) \in H^1(\Omega) \times \mathbb{R}\,.$$

Similarly, instead of (3.8), one solves: Find $(u'(\sigma)h, c) \in H^1(\Omega) \times \mathbb{R}$ such that

$$a_\sigma(u'(\sigma)h, v) + c \int_\Omega v \, dx + d \int_\Omega u'(\sigma)h \, dx = -a_h(u, v)\,, \qquad \forall\, (v, d) \in H^1(\Omega) \times \mathbb{R}\,.$$

Since in both of the above variational problems one can chose $(v, d) = (0, 1)$ it follows that both $u$ and $u'(\sigma)h$ computed this way are in $V$.

# Bibliography


[ABC+08] H. Ammari, E. Bonnetier, Y. Capdeboscq, M. Tanter, and M. Fink. Electrical Impedance Tomography by Elastic Deformation. *SIAM Journal on Applied Mathematics*, 68(6):1557–1573, 2008.

[ABH+15] M. S. Alnæs, J. Blechta, J. Hake, A. Johansson, B. Kehlet, A. Logg, C. Richardson, J. Ring, M. E. Rognes, and G. N. Wells. The FEniCS Project Version 1.5. *Archive of Numerical Software*, 3(100), 2015.

[ADN59] S. Agmon, A. Douglis, and L. Nirenberg. Estimates near the boundary for solutions of elliptic partial differential equations satisfying general boundary conditions. I. *Communications on Pure and Applied Mathematics*, 12(4):623–727, 1959.

[AF03] R. A. Adams and J. J. F. Fournier. *Sobolev Spaces*. Pure and Applied Mathematics. Elsevier Science, 2003.

[AGL15] A. Adler, R. Gaburro, and W. Lionheart. Electrical Impedance Tomography. *Handbook of Mathematical Methods in Imaging*, 1:701–762, 2015.

[Ale88] G. Alessandrini. Stable determination of conductivity by boundary measurements. *Applicable Analysis*, 27(1-3):153–172, 1988.

[Amm08] H. Ammari. *An Introduction to Mathematics of Emerging Biomedical Imaging*. Mathématiques & Applications. Berlin: Springer, 2008.

[AP06] K. Astala and L. Paivarinta. Calderón's inverse conductivity problem in the plane. *Annals of Mathematics*, 163(1):262–299, 2006.

[AS12] S. Arridge and O. Scherzer. Imaging from coupled physics. *Inverse Problems*, 28(8):080201, 2012.

[Bal13a] G. Bal. Cauchy problem for ultrasound-modulated EIT. *Analysis and PDE*, 6(4):751–775, 2013.

[Bal13b] G. Bal. Hybrid inverse problems and internal functionals. *Mathematical Sciences Research Institute Publications*, 60:325–368, 2013.

[Bal14] G. Bal. Hybrid inverse problems and redundant systems of partial differential equations. *Inverse Problems and Applications: Conference on Inverse Problems, in honor of Gunther Uhlmann, June 18-22, 2012, University of California, Irvine, CA; International Conference on Inverse Problems, in honor of Gunther Uhlmann's 60th birthday, September 17-21, 2012, Zhejiang University, Hangzhou, China*, 615:325–368, 2014.

[BBIM14] G. Bal, C. Bellis, S. Imperiale, and F. Monard. Reconstruction of constitutive parameters in isotropic linear elasticity from noisy full–field measurements. *Inverse Problems*, 30(12):125004, 2014.

[BBMT13] G. Bal, E. Bonnetier, F. Monard, and F. Triki. Inverse diffusion from knowledge of power densities. *Inverse Problems and Imaging*, 7(2):353–375, 2013.

[BG04] P. E. Barbone and N. H. Gokhale. Elastic modulus imaging: on the uniqueness and nonuniqueness of the elastography inverse problem in two dimensions. *Inverse Problems*, 20(1):283–296, 2004.

[BKA10] J. Baumeister, B. Kaltenbacher, and A. Leitao. On Levenberg-Marquardt-Kaczmarz iterative methods for solving systems of nonlinear ill-posed equations. *Inverse Problems and Imaging*, 4(3):335–350, 2010.

[BNSS13] G. Bal, W. Naetar, O. Scherzer, and J. Schotland. The Levenberg-Marquardt iteration for numerical inversion of the power density operator. *Journal of Inverse and Ill-Posed Problems*, 21(2):265–280, 2013.

[BO07] P. E. Barbone and A. A. Oberai. Elastic modulus imaging: some exact solutions of the compressible elastography inverse problem. *Physics in Medicine and Biology*, 52(6):1577–1593, 2007.

[Bor02] L. Borcea. Electrical impedance tomography. *Inverse Problems*, 18(6):99–136, 2002.

[BU12] G. Bal and G. Uhlmann. Reconstructions for some coupled-physics inverse problems. *Applied Mathematics Letters*, 25(7):1030–1033, 2012.

[BU13] G. Bal and G. Uhlmann. Reconstruction of coefficients in scalar second-order elliptic equations from knowledge of their solutions. *Communications on Pure and Applied Mathematic*, 66(10):1629–1652, 2013.

[Cal80] A. P. Calderón. On an inverse boundary value problem. *Seminar on Numerical Analysis and its Applications to Continuum Physics (Rio de Janeiro, 1980)*, pages 65–73, 1980.

[CFdGK09] Y. Capdeboscq, J. Fehrenbach, F. de Gournay, and O. Kavian. Imaging by modification: Numerical reconstruction of local conductivities from corresponding power density measurements. *SIAM Journal on Imaging Sciences*, 2(4):1003–1030, 2009.

[CHLS08] A. De Cezaro, M. Haltmeier, A. Leitao, and O. Scherzer. On Steepest-Descent-Kaczmarz methods for regularizing systems of nonlinear ill-posed equations. *Applied Mathematics and Computation*, 202(2):596–607, 2008.

[Cia94] P. G. Ciarlet. *Three-dimensional elasticity*, volume 1 of *Mathematical Elasticity*. North-Holland, 1994.

[CIN99] M. Cheney, D. Isaacson, and J. C. Newell. Electrical Impedance Tomography. *SIAM Review*, 41(1):85–101, 1999.

[DMB00] M. M. Doyley, P. M. Meaney, and J. C. Bamber. Evaluation of an iterative reconstruction method for quantitative elastography. *Physics in Medicine and Biology*, 45(6):1521–1540, 2000.

[Doy12] M. M. Doyley. Model-based elastography: a survey of approaches to the inverse elasticity problem. *Physics in Medicine and Biology*, 57(3):R35–R73, 2012.

[EHN96] H. W. Engl, M. Hanke, and A. Neubauer. *Regularization of inverse problems*. Dordrecht: Kluwer Academic Publishers, 1996.

[EKN89] H. W. Engl, K. Kunisch, and A. Neubauer. Convergence rates for Tikhonov regularisation of non-linear ill-posed problems. *Inverse Problems*, 5(4):523, 1989.

[Eva98] L. C. Evans. *Partial Differential Equations*. Graduate Studies in Mathematics. American Mathematical Society, 1998.

[FMST06] J. Fehrenbach, M. Masmoudi, R. Souchon, and P. Trompette. Detection of small inclusions by elastography. *Inverse Problems*, 22(3):1055–1069, 2006.

[GBO08] N. H. Gokhale, P. E. Barbone, and A. A. Oberai. Solution of the nonlinear elasticity imaging inverse problem: the compressible case. *Inverse Problems*, 24(4):045010, 2008.

[Gri92] P. Grisvard. *Singularities in Boundary Value Problems.* Research Notes in Applied Mathematics. Masson, 1992.

[Gri11] P. Grisvard. *Elliptic Problems in Nonsmooth Domains.* Classics in Applied Mathematics. Society for Industrial and Applied Mathematics, 2011.

[GS08] B. Gebauer and O. Scherzer. Impedance-Acoustic Tomography. *SIAM Journal on Applied Mathematics*, 69(2):565–576, 2008.

[GT98] D. Gilbarg and N. S. Trudinger. *Elliptic partial differential equations of second order.* Grundlehren der mathematischen Wissenschaften. Springer, 1998.

[Had23] J. Hadamard. *Lectures on the Cauchy Problem in Linear Partial Differential Equations.* Yale University Press, New Haven, 1923.

[Han97] M. Hanke. A regularizing Levenberg-Marquardt scheme, with applications to inverse groundwater filtration problems. *Inverse Problems*, 13(1):79, 1997.

[HBIK97] T.J. Hall, M. Bilgen, M.F. Insana, and T.A. Krouskop. Phantom materials for elastography. *Trans. Ultrason., Ferroeletr., Freq. Control*, 44(6):1355–1365, 1997.

[HK14] K. Hoffmann and K. Knudsen. Iterative reconstruction methods for hybrid inverse problems in impedance tomography. *Sensing and Imaging*, 15(96):1–27, 2014.

[HLS07] M. Haltmeier, A. Leitao, and O. Scherzer. Kaczmarz methods for regularizing nonlineal ill-posed equations I: Convergence analysis. *Inverse Problems and Imaging*, 1(2):289–298, 2007.

[HNS95] M. Hanke, A. Neubauer, and O. Scherzer. A convergence analysis of the Landweber iteration for nonlinear ill-posed problems. *Numerische Mathematik*, 72(1):21–37, 1995.

[Hol05] D. S. Holder. *Electrical Impedance Tomography: Methods, History and Applications.* Boca Raton: CRC Press, 2005.

[HR17] S. Hubmer and R. Ramlau. Convergence analysis of a two-point gradient method for nonlinear ill-posed problems. *Inverse Problems*, 33(9):095004, 2017.

[HS97] C. H. Huang and W. Y. Shih. A boundary element based solution of an inverse elasticity problem by conjugate gradient and regularization method. *Inverse Problems in Engineering*, 4(4):295–321, 1997.

[Jin10] Q. Jin. On a regularized Levenberg-Marquardt method for solving nonlinear inverse problems. *Numerische Mathematik*, 115(2):229–259, 2010.

[Jin16] Q. Jin. Landweber-Kaczmarz method in banach spaces with inexact inner solvers. *Inverse Problems*, 32(10):104005, 2016.

[JKR08] B. Jadamba, A. A. Khan, and F. Raciti. On the inverse problem of identifying Lamé coefficients in linear elasticity. *Computers and Mathematics with Applications*, 56(2):431–443, 2008.

[JL12] M. Jung and U. Langer. *Methode der finiten Elemente für Ingenieure: Eine Einführung in die numerischen Grundlagen und Computersimulation*. SpringerLink: Bücher. Springer Fachmedien Wiesbaden, 2012.

[JM04] L. Ji and J. McLaughlin. Recovery of the Lamé parameter $\mu$ in biological tissues. *Inverse Problems*, 20(1):1–24, 2004.

[JMRY03] L. Ji, J. R. McLaughlin, D. Renzi, and J. R. Yoon. Interior elastodynamics inverse problems: shear wave speed reconstruction in transient elastography. *Inverse Problems*, 19(6):S1–S29, 2003.

[Kir96] A. Kirsch. *An Introduction to the Mathematical Theory of Inverse Problems*. Springer-Verlag New York, 1996.

[KK10] P. Kuchment and L. Kunyansky. Synthetic focusing in ultrasound modulated tomography. *Inverse Problems and Imaging*, 4(4):665–673, 2010.

[KK11] P. Kuchment and L. Kunyansky. 2D and 3D reconstructions in acousto-electric tomography. *Inverse Problems*, 27(5):055013, 2011.

[KL14] S. Kindermann and A. Leitao. Convergence rates for Kaczmarz-type regularization methods. *Inverse Problems and Imaging*, 8(1):149–172, 2014.

[KNS08] B. Kaltenbacher, A. Neubauer, and O. Scherzer. *Iterative Regularization Methods for Nonlinear Ill-Posed Problems*. Berlin: de Gruyter, 2008.

[Koc12] I. Kocyigit. Acousto-electric tomography and CGO solutions with internal data. *Inverse Problems*, 28(12):125004, 2012.

[KR16] A. Kirsch and A. Rieder. Inverse problems for abstract evolution equations with applications in electrodynamics and elasticity. *Inverse Problems*, 32(8):085001, 2016.

[KS02] R. Kowar and O. Scherzer. Convergence analysis of a Landweber-Kaczmarz method for solving nonlinear ill-posed problems. *Ill-Posed and Inverse Problems*, 23:69–90, 2002.

[KS12] P. Kuchment and D. Steinhauer. Stabilizing inverse problems by internal data. *Inverse Problems*, 28(8):084007, 2012.

[Kuc12] P. Kuchment. Mathematics of hybrid imaging: A brief review. *The Mathematical Legacy of Leon Ehrenpreis*, 16:183–208, 2012.

[LM12] J. L. Lions and E. Magenes. *Non-Homogeneous Boundary Value Problems and Applications.* Number 3 in Grundlehren der mathematischen Wissenschaften. Springer Berlin Heidelberg, 2012.

[LS17] A. Lechleiter and J. W. Schlasche. Identifying Lamé parameters from time-dependent elastic wave measurements. *Inverse Problems in Science and Engineering*, 25(1):2–26, 2017.

[McL00] W. C. H. McLean. *Strongly Elliptic Systems and Boundary Integral Equations.* Cambridge University Press, 2000.

[MOD+01] A. Manduca, T. E. Oliphant, M. A. Dresner, J. L. Mahowald, S. A. Krise, E. Amromin, J. P. Felmlee, J. F. Greenleaf, and R. L. Ehman. Magnetic resonance elastography: non-invasive mapping of tissue elasticity. *Medical Image Analysis*, 5:237–254, 2001.

[MR06] J. McLaughlin and D. Renzi. Shear wave speed recovery in transient elastography and supersonic imaging using propagating fronts. *Inverse Problems*, 22(2):681–706, 2006.

[MS12] J. L. Mueller and S. Siltanen. *Linear and nonlinear inverse problems with practical applications.* Computational Science and Engineering. SIAM, 2012.

[MY04] J. McLaughlin and J.-R. Yoon. Unique identifiability of elastic parameters from time-dependent interior displacement measurement. *Inverse Problems*, 20(1):25–45, 2004.

[Nac96] A. I. Nachman. Global uniqueness for a two-dimensional inverse boundary value problem. *Annals of Mathematics*, 143(1):71–96, 1996.

[Nec11] J. Necas. *Direct Methods in the Theory of Elliptic Equations.* Springer Monographs in Mathematics. Springer Berlin Heidelberg, 2011.

[Nes83] Y. Nesterov. A method of solving a convex programming problem with convergence rate $O(1/k^2)$. *Soviet Mathematics Doklady*, 27(2):372–376, 1983.

[Neu00] A. Neubauer. On Landweber iteration for nonlinear ill-posed problems in Hilbert scales. *Numerische Mathematik*, 85(2):309–328, 2000.

[Neu17a] A. Neubauer. A new gradient method for ill-posed problems. 2017. submitted.

[Neu17b] A. Neubauer. On Nesterov acceleration for Landweber iteration of linear ill-posed problems. *Journal of Inverse and Ill-Posed Problems*, 25(3):381–390, 2017.

[OGDB04] A. A. Oberai, N. H. Gokhale, M. M. Doyley, and J. C. Bamber. Evaluation of the adjoint equation based algorithm for elasticity imaging. *Physics in Medicine and Biology*, 49(13):2955–2974, 2004.

[OGF03] A. A. Oberai, N. H. Gokhale, and G. R. Feijoo. Solution of inverse problems in elasticity imaging using the adjoint method. *Inverse Problems*, 19(2):297–313, 2003.

[Sch96] O. Scherzer. A convergence analysis of a method of steepest descent and a two-step algorithm for nonlinear ill-posed problems. *Numerical Functional Analysis and Optimization*, 17(1-2):197–214, 1996.

[Sch02] E. Schock. Nonlinear Ill-Posed Problems, Three Counterexamples. *Inverse Problems*, 18:715–717, 2002.

[SCI92] E. Somersalo, M. Cheney, and D. Isaacson. Existence and Uniqueness for Electrode Models for Electric Current Computed Tomography. *SIAM Journal on Applied Mathematics*, 52(4):1023–1040, 1992.

[SKHK12] T. Schuster, B. Kaltenbacher, B. Hofmann, and K. S. Kazimierski. *Regularization Methods in Banach Spaces*. Radon Series on Computational and Applied Mathematics. De Gruyter, 2012.

[SRB10] D. Sun, S. Roth, and M.J. Black. Secrets of optical flow estimation and their principles. *CVPR*, pages 2432–2439, 2010.

[SU87] J. Sylvester and G. Uhlmann. A global uniqueness theorem for an inverse boundary value problem. *Annals of Mathematics*, 125(1):153–169, 1987.

[Tik63a] A. N. Tikhonov. Regularization of incorrectly posed problems. *Soviet Mathematics Doklady*, 4:1624–1627, 1963.

[Tik63b] A. N. Tikhonov. Solution of incorrectly formulated problems and the regularization method. *Soviet Mathematics Doklady*, 4:1035–1038, 1963.

[Val13] T. Valent. *Boundary Value Problems of Finite Elasticity: Local Theorems on Existence, Uniqueness, and Analytic Dependence on Data*. Springer Tracts in Natural Philosophy. Springer New York, 2013.

[WS12] T. Widlak and O. Scherzer. Hybrid tomography for conductivity imaging. *Inverse Problems*, 28(8):084008, 2012.

[WS15] T. Widlak and O. Scherzer. Stability in the linearized problem of quantitative elastography. *Inverse Problems*, 31(3):035005, 2015.

[ZW04] H. Zhang and L. V. Wang. Acousto-electric tomography. *Proceedings SPIE, Photons Plus Ultrasound: Imaging and Sensing*, 5320(9):145–149, 2004.

# Journal papers

# Paper A

**Limited Angle Electrical Impedance Tomography with Power Density Data**

| | |
|---|---|
| Type | Submitted manuscript (2017) |
| Authors | Simon Hubmer, Kim Knudsen, Changyou Li and Ekaterina Sherina |
| Available from | https://arxiv.org/abs/1712.08009 |

# Limited Angle Electrical Impedance Tomography with Power Density Data

Simon Hubmer*, Kim Knudsen†, Changyou Li‡, Ekaterina Sherina§

December 22, 2017

**Abstract**

This paper considers the reconstruction problem in Acousto-Electrical Tomography, i.e., the problem of estimating a spatially varying conductivity in a bounded domain from measurements of the internal power densities resulting from different prescribed boundary conditions. Particular emphasis is placed on the limited angle scenario, in which the boundary conditions are supported only on a part of the boundary. The reconstruction problem is formulated as an optimization problem in a Hilbert space setting and solved using Landweber iteration. The resulting algorithm is implemented numerically in two spatial dimensions and tested on simulated data. The results quantify the intuition that features close to the measurement boundary are stably reconstructed and features further away are less well reconstructed. Finally, the ill-posedness of the limited angle problem is quantified numerically using the singular value decomposition of the corresponding linearized problem.

**Keywords:** Electrical Impedance Tomography, Acousto-Electrical Tomography, Limited Angle, Hybrid Data, Inverse Problem, Parameter Identification, Landweber Iteration, Regularization Method

**AMS:** 65J22, 35R30, 65M32

## 1 Introduction

Electrical Impedance Tomography is an emerging technology that aims at reconstructing the spatially varying electric conductivity distribution in a body from electrostatic

*Johannes Kepler University Linz, Doctoral Program Computational Mathematics, Altenbergerstraße 69, A-4040 Linz, Austria (simon.hubmer@dk-compmath.jku.at)

†Technical University of Denmark, Department of Applied Mathematics and Computer Science, Asmussens Allé, 2800 Kongens Lyngby, Denmark (kiknu@dtu.dk)

‡Technical University of Denmark, Department of Applied Mathematics and Computer Science, Asmussens Allé, 2800 Kongens Lyngby, Denmark (chgy@dtu.dk) and School of Electronics and Information, Northwestern Polytechnical University, Xian, China

§Technical University of Denmark, Department of Applied Mathematics and Computer Science, Asmussens Allé, 2800 Kongens Lyngby, Denmark (sershe@dtu.dk), corresponding author

measurements of voltages and the corresponding current fluxes on the surface of the body. The quantitative and structural information acquired about the conductivity of the body can potentially be valuable for medical and industrial applications. For example, EIT shows great promise for bed side lung monitoring [18] and for non-destructive testing of concrete [22, 23].

The reconstruction problem in EIT is well-known for being (severely) ill-posed [27]. To overcome the ill-posednes a novel idea of coupling EIT with a different physical phenomena has been promoted in the last decade. EIT used together with magnetic resonance leads to so-called Magnetic Resonance EIT [34], whereas EIT modulated by ultrasound waves leads to Acousto-Electrical Tomography [2, 26, 35] (or equivalently Impedance-Acoustic Tomography (IAT) [14]). Both modalities give rise to additional interior information and may potentially lead to a significant improvement of the conductivity reconstructions having both high contrast and resolution.

In this paper we focus on Acousto-Electrical Tomography (AET). Denote by $\sigma$ the spatially varying conductivity in the bounded and smooth domain $\Omega \subset \mathbb{R}^N$, $N = 2, 3$. The power density is defined as

$$E(\sigma) := \sigma \left|\nabla u(\sigma)\right|^2 , \tag{1.1}$$

where $u(\sigma)$ denotes the interior voltage potential given as the solution of the elliptic equation

$$\operatorname{div}(\sigma \nabla u) = 0 , \qquad \text{in } \Omega . \tag{1.2}$$

Most studies [2, 7, 10] consider the case of (1.2) being supplemented with Dirichlet conditions on the boundary $\partial\Omega$

$$u|_{\partial\Omega} = f . \tag{1.3}$$

In contrast, this paper considers however (1.2) supplemented with Neumann boundary conditions

$$(\sigma \nabla u) \cdot \vec{n}|_{\partial\Omega} = g , \tag{1.4}$$

and can thus be seen as an extension of the mentioned literature. Note that physically the function $g$ measures the current flux at the boundary in the normal direction given by the outward unit normal $\vec{n}$ to $\partial\Omega$.

It is well known that a single measurement of the power density $\sigma \left|\nabla u(\sigma)\right|^2$ is in general not enough to uniquely determine the conductivity $\sigma$ [4, 20]. However, it was shown in [10] for the two dimensional case that if measurements

$$\left(\sigma \left|\nabla u_1(\sigma)\right|^2 , \sigma \left|\nabla u_2(\sigma)\right|^2 , \sigma \nabla u_1(\sigma) \cdot \nabla u_2(\sigma)\right) ,$$

with

$$\det\left(\nabla u_1(\sigma), \nabla u_2(\sigma)\right) \geq c > 0 , \tag{1.5}$$

are available, then $\sigma$ can be uniquely determined from those measurements. (Note that the third measurement can be obtained from a third power density measurement by the polarization identity.) Similar results were also obtained for 3 dimensions in [5] and for arbitrary dimensions in [28]. Hence, the reconstruction of $\sigma$ profits from multiple

power density measurements. See also [6, 9, 16] for more information about the choice of boundary conditions.

Under the abovementioned assumptions the inverse problem is well-posed and one can expect to reconstruct the conductivity stably with high contrast and resolution; see [2, 7, 10, 17] for some numerical implementations of the problem.

To model the scenario when only a part of the boundary is accessible to the electrostatic measurements we introduce the proper subset $\Gamma_1 \subset \partial\Omega$ and assume that the induced current field has $\mathrm{supp}(g) \subset \Gamma_1$. This assumption tacitly enforces a no flux condition on the inaccessible boundary $\Gamma_0 = \partial\Omega \setminus \Gamma_1$. The main purpose of this paper is to study the influence of the size of $\Gamma_1$ on the quality of the reconstructions. See [3] for related work.

For EIT the problem of limited angle data (in that context known as partial data) is fairly well understood [8, 19, 24, 25]; and the instability is known to be severe [11]. We expect that a similar instability appears here and we want to see how the ill-posedness of the problem is affected by accessibility of the measurement boundary.

In this paper we take a computational approach to the problem by formulating the inverse problem as a nonlinear operator equation

$$F(\sigma) = E\,. \tag{1.6}$$

We provide the Fréchet derivative and its adjoint of the operator $F$ and approximate the solution using Landweber iteration. Numerical examples are presented focusing especially on the limited angle problem. Furthermore, a numerical ill-posedness quantification is performed, quantifying the expected reconstruction quality in various areas of the domain $\Omega$ in this case by considering the singular value decomposition of the linearized problem.

The paper is organized as follows: in Section 2 we recall the basic notation and important results from PDE theory for the problem (1.2), (1.4). In Section 3 we discuss the inverse problem (1.6), showing that the operator $F$ is Frechet differentiable. Furthermore, we derive the Frechet derivative and the adjoint thereof. The results are generalized to multiple measurements of the power density. The regularization approach, which we apply for approximating the solution of the inverse problem (1.6), is briefly outlined in Section 4. The idea on ill-posedness quantification of the problem are given in Section 5. In Sections 6 and 7 we describe the setting of our numerical example problem and present various reconstruction results for different boundary settings, especially focusing on the limited angle case. Moreover, we present results of the ill-posedness quantification.

# 2 Mathematical Preliminaries

In this section we recall the basic notations and results for the Neumann problem (1.2), (1.4). In addition we consider the Fréchet differentiablity of the solution $u$ with respect to $\sigma$. We start by stating the main assumptions taken throughout:

**Assumption 2.1.** Let $\Omega$ denote a non-empty, bounded, open and connected set in $\mathbb{R}^N$, $N = 2, 3$, with boundary $\partial\Omega \in C^{1,1}$. Furthermore, assume that $g \in L^2(\partial\Omega)$ be given such that

$$\int_{\partial\Omega} g \, dS = 0 \,. \tag{2.1}$$

Finally, we assume that a priori a lower bound $\underline{\sigma} > 0$ is given such that

$$\sigma \in \mathcal{M}(\underline{\sigma}) := \{\sigma \in L^\infty(\Omega) \,|\, \sigma \geq \underline{\sigma} > 0\} \,.$$

It is well-known from standard theory for elliptic PDEs [15] that under Assumption 2.1 the Neumann problem (1.2), (1.4) has a unique weak solution

$$u(\sigma) \in H^1_\diamond(\Omega) := \left\{ u \in H^1(\Omega) \,\middle|\, \int_\Omega u \, dx = 0 \right\} \,.$$

We occasionally drop $\sigma$ in the notation and write $u = u(\sigma)$. Moreover, there is a constant $C > 0$ such that

$$\|u\|_{H^1(\Omega)} \leq C \, \|g\|_{L^2(\partial\Omega)} \,.$$

If in addition $\sigma \in C^{0,1}(\Omega)$ and $g \in H^{1/2}(\partial\Omega)$ then $u \in H^2(\Omega)$ with

$$\|u\|_{H^2(\Omega)} \leq C \, \|g\|_{H^{1/2}(\partial\Omega)} \,.$$

We now consider the solution mapping $u \colon \sigma \mapsto u(\sigma)$ as a mapping $\mathcal{M}(\underline{\sigma}) \to L^2(\Omega)$. From the weak formulation of the PDE problem the continuity estimate

$$\|u(\sigma) - u(\sigma_0)\|_{H^1(\Omega)} \leq c_{LM} \, \|\sigma - \sigma_0\|_{L^\infty(\Omega)} \, \|u(\sigma_0)\|_{H^1(\Omega)} \,.$$

follows. In addition, $u$ is Fréchet differentiable with derivative $u'(\sigma)h$ at $\sigma \in \mathcal{M}(\underline{\sigma})$ in direction $h$, given as the unique weak solution to the Neumann problem

$$\begin{aligned} \operatorname{div}(\sigma \nabla(u'(\sigma)h)) &= -\operatorname{div}(h \nabla u(\sigma)) \,, \qquad \text{in } \Omega \,, \\ (\sigma \nabla(u'(\sigma)h)) \cdot \vec{n}|_{\partial\Omega} &= 0 \,. \end{aligned} \tag{2.2}$$

# 3 Fréchet Differentiability of the Forward Operator

In this section we consider the forward operator $F \colon \sigma \mapsto E(\sigma)$. We first analyse the mapping properties in the situation of a single boundary condition and show that $F$ is Fréchet differentiable. Then we generalize the results to more boundary conditions.

## 3.1 The Single Measurement Case

When $\sigma \in \mathcal{M}(\underline{\sigma})$ the power density is naturally considered as an element in $L^1(\Omega)$, i.e.,

$$\begin{aligned} F : \mathcal{M}(\underline{\sigma}) &\to L^1(\Omega)\,, \\ \sigma &\mapsto E(\sigma)\,, \end{aligned} \tag{3.1}$$

but since $L^1(\Omega)$ is not reflexive, solving (1.6) in $L^1(\Omega)$ is not straightforward. By increasing the regularity of $\sigma$ we pose the problem in a better suited Hilbert space. Introduce the space

$$\mathcal{D}_s(F) := H^s(\Omega) \cap \mathcal{M}(\underline{\sigma})\,, \tag{3.2}$$

and note that for $s > N/2 + 1$ by Sobolev embedding $\mathcal{D}_s(F) \subset C^{0,1}(\overline{\Omega}) \cap \mathcal{M}(\underline{\sigma})$, and hence $u(\sigma) \in H^2(\Omega)$ leaving $E(\sigma) \in L^2(\Omega)$ by the Hölder inequality. Thus we can consider

$$F : \mathcal{D}_s(F) \to L^2(\Omega)\,, \tag{3.3}$$

and the equation (1.6) can be considered in the standard framework of nonlinear ill-posed problems in Hilbert spaces [12].

We eventually address (1.6) using an iterative approach and hence the Fréchet derivative is required. In the following proposition we obtain the derivative. The proof is analogous to the case of Dirichlet boundary conditions [7].

**Proposition 3.1.** *The operators $F : \mathcal{D}_s(F) \to L^2(\Omega)$ defined by (3.3) is Fréchet differentiable for $s > N/2 + 1$ with*

$$F'(\sigma)h = h\,|\nabla u(\sigma)|^2 + 2\,\sigma \nabla u(\sigma) \cdot \nabla(u'(\sigma)h)\,, \tag{3.4}$$

*where $u'(\sigma)h$ is defined by (2.2).*

*Proof.* This follows immediately from the definition of the operator, (2.2) and the product and the chain rule applied to the function $x\,|\nabla f(x)|^2$, in the same way as in [7]. □

In order to calculate the adjoint of $F$, we need the following proposition regarding the adjoint of embedding operators in Sobolev spaces.

**Proposition 3.2.** *Denote by $E_s : H^s(\Omega) \to L^2(\Omega)$ the embedding operator for $s \geq 0$, i.e., $E_s v = v$ for all $v \in H^s(\Omega)$. Then for any element $w \in L^2(\Omega)$ the adjoint $E_s^* w$ is given as the unique solution of the variational problem*

$$\langle\, E_s^* w, v \,\rangle_{H^s(\Omega)} = \langle\, w, v \,\rangle_{L^2(\Omega)}\,, \qquad \forall\, v \in H^s(\Omega)\,. \tag{3.5}$$

*Proof.* This follows from the definition of $E_s$ and the Lax-Milgram Lemma. □

We are now prepared to give the adjoint of $F$:

**Theorem 3.3.** *Let $F : \mathcal{D}_s(F) \to L^2(\Omega)$ be defined by (3.3) with $s > N/2+1$. Then for the adjoint of the Fréchet derivative of $F$ there holds*

$$F'(\sigma)^* w = E_s^* \left( w \, |\nabla u(\sigma)|^2 + 2\nabla u(\sigma) \cdot \nabla(Aw) \right) ,$$

*where $Aw \in V$ is given as the unique solution of the variational problem*

$$\int_\Omega \sigma \nabla(Aw) \cdot \nabla v \, dx = - \int_\Omega \sigma w \nabla u(\sigma) \cdot \nabla v \, dx , \qquad \forall \, v \in V . \tag{3.6}$$

*Proof.* By Proposition 3.1 we have

$$\begin{aligned} \langle \, F'(\sigma)h, w \, \rangle_{L^2(\Omega)} &= \left\langle \, h \, |\nabla u(\sigma)|^2 + 2\sigma \nabla u(\sigma) \cdot \nabla(u'(\sigma)h), w \, \right\rangle_{L^2(\Omega)} \\ &= \left\langle \, h, w \, |\nabla u(\sigma)|^2 \, \right\rangle_{L^2(\Omega)} + 2 \int_\Omega \sigma w \nabla u(\sigma) \cdot \nabla(u'(\sigma)h) \, dx . \end{aligned}$$

Together with (3.6) and (2.2), there follows

$$\begin{aligned} \int_\Omega \sigma w \nabla u(\sigma) \cdot \nabla(u'(\sigma)h) \, dx &= - \int_\Omega \sigma \nabla(Aw) \cdot \nabla(u'(\sigma)h) \, dx \\ &= \int_\Omega h \nabla u(\sigma) \cdot \nabla(Aw) \, dx , \end{aligned}$$

which, together with (3.5) implies

$$\begin{aligned} \langle \, F'(\sigma)h, w \, \rangle_{L^2(\Omega)} &= \left\langle \, h, w \, |\nabla u(\sigma)|^2 + 2\nabla u(\sigma) \cdot \nabla(Aw) \, \right\rangle_{L^2(\Omega)} \\ &= \left\langle \, h, E_s^* \left( w \, |\nabla u(\sigma)|^2 + 2\nabla u(\sigma) \cdot \nabla(Aw) \right) \, \right\rangle_{H^s(\Omega)} , \end{aligned}$$

which yields the assertion. □

*Remark.* If $s$ is an integer, we can also consider the following inner product on $H^s(\Omega)$

$$\langle \, u, v \, \rangle_{s,\beta} := \sum_{|\alpha| \le s} \beta_\alpha \, \langle \, \partial^\alpha u, \partial^\alpha v \, \rangle_{L^2(\Omega)} ,$$

where $\{\beta_\alpha\}$ is a family of positive weights. The resulting inner product generalizes the standard inner product $\langle \, . \, , . \, \rangle_{H^s(\Omega)}$ and induces an equivalent norm on $H^s(\Omega)$. The adjoint of the operators $F : \mathcal{D}_s(F) \to L^2(\Omega)$ with respect to these inner products can be computed the same way as in Theorem 3.3, with $E_s^*$ replaced by $E_{s,\beta}^*$, where $E_{s,\beta}^* w \in H^s(\Omega)$ is given as the unique solution of the variational problem

$$\left\langle \, E_{s,\beta}^* w, v \, \right\rangle_{s,\beta} = \langle \, w, v \, \rangle_{L^2(\Omega)} , \qquad \forall \, v \in H^s(\Omega) . \tag{3.7}$$

Using this weighted inner product gives us more flexibility in the reconstruction process, as we can put emphasis on different derivatives of the solution. A similar generalization of the scalar product is also possible for $H^s(\Omega)$ with $s \in \mathbb{R}$.

### 3.2 The Multiple Measurement Case

As mentioned in the introduction, having the internal power density for one boundary condition is in general not sufficient to uniquely reconstruct the conductivity. To consider multiple data we introduce $\{g_j\}_{j=1}^M$ of boundary current data such that $g_j \in H^{\frac{1}{2}}(\partial\Omega)$, for $j \in \{1, \dots, M\}$ where $M \in \mathbb{N}$ is fixed. Furthermore, denote by $E_j$ the power density

$$E_j(\sigma) := \sigma \left|\nabla u_j(\sigma)\right|^2 ,$$

where $u_j(\sigma)$ is the weak solution of the boundary value problem

$$\begin{aligned} -\operatorname{div}(\sigma \nabla u_j) &= 0 , \quad \text{in } \Omega , \\ (\sigma \nabla u_j) \cdot \vec{n}\,|_{\partial\Omega} &= g_j . \end{aligned} \tag{3.8}$$

This problem can again be written as a nonlinear inverse problem in standard form, or rather, as a nonlinear system in standard form, by introducing the nonlinear operator

$$F : \mathcal{D}_s(F) \to L^2(\Omega)^M , \quad \sigma \mapsto \{E_j(\sigma)\}_{j=1}^M . \tag{3.9}$$

Continuity and Fréchet differentiability readily translate from $F$ (3.1) in the single measurement case to $F$ defined by (3.9). For example, for the Fréchet derivative we have

$$F'(\sigma)h := \left\{h \left|\nabla u_j(\sigma)\right|^2 + 2\,\sigma \nabla u_j(\sigma) \cdot \nabla(u_j'(\sigma)h)\right\}_{j=1}^M , \tag{3.10}$$

with $u_j'(\sigma)h$ being given analogously as in (2.2), and for the adjoint we have

$$F'(\sigma)^* w := \sum_{j=1}^M E_s^* \left(w_j \left|\nabla u_j(\sigma)\right|^2 + 2\,\sigma \nabla u_j(\sigma) \cdot \nabla(A w_j)\right) . \tag{3.11}$$

# 4 Iterative Regularization Approach

Both the single and the multiple measurement problems of the previous section are inverse problems in the standard form

$$F(x) = y ,$$

and therefore, need to be regularized in order to enable a stable reconstruction of the conductivity $\sigma$ from noisy measurement data $E^\delta$. Besides well-known Tikhonov regularization and its variants [12], iterative regularization methods are very popular, especially for nonlinear Inverse Problems [21]. Since the focus of this paper lies more on qualitative and quantitative aspects of the solution and less on numerical efficiency, we focus on the following simple yet robust Landweber-type gradient method, given by

$$\begin{aligned} x_{k+1}^\delta &= x_k^\delta + \omega_k^\delta \left(x_k^\delta\right) s_k^\delta \left(x_k^\delta\right) , \\ s_k^\delta(x) &:= F'(x)^* \left(y^\delta - F(x)\right) , \end{aligned} \tag{4.1}$$

where for the stepsize $\omega_k^\delta$ we use the steepest descent stepsize [32]

$$\omega_k^\delta(x) := \frac{\left\| s_k^\delta(x) \right\|^2}{\left\| F'(x) s_k^\delta(x) \right\|^2} \,. \tag{4.2}$$

As a stopping rule, we employ the well-known Morozov discrepancy principle [29], i.e., the iteration is stopped after $k_*$ steps, with $k_*$ satisfying

$$\left\| y^\delta - F\left(x_{k_*}^\delta\right) \right\| \le \tau\delta \le \left\| y^\delta - F\left(x_k^\delta\right) \right\| \,, \qquad 0 \le k \le k_* \,, \tag{4.3}$$

where $\tau$ is an appropriately chosen positive number ($\tau \in [1,2]$ being common practise).

*Remark.* Note that for proving convergence of iterative regularization methods one requires at least a weak form of the so-called nonlinearity or tangential cone condition (see [21] for details). This condition is to the best of our knowledge not known for this particular problem.

# 5 Ill-Posedness Quantification

In order to get a better understanding of the reconstruction quality in different areas of the domain, we also consider an ill-posedness quantification of the problem based on the singular value decomposition (SVD) of the discretization of the Fréchet derivative of $F$ at the exact solution $\sigma^\dagger$.

For linear operators $F$, the degree of ill-posedness of the inverse problem $F(x) = y$ is directly connected to the singular value expansion of $F$ [12], a rapid decay of the singular values corresponding for example to severe ill-posedness of the problem. In the nonlinear case, the connection between the ill-posedness and the Fréchet derivative $F'(x)$ is not as strong as one might expect it to be (see for example [13,33]). However, in many cases there is a connection, as can for example be seen from the assumption

$$\left\| F(x^\dagger)h \right\|_Y \ge c \left\| h \right\|_{-a} \,, \qquad \forall\, h \in X \,, \tag{5.1}$$

commonly used for analyzing iterative methods in Hilbert scales [31]. Here the parameter $a$ effectively measures the degree of ill-posedness of the problem. Furthermore, since almost all methods for solving ill-posed problems rely on the Fréchet derivative of $F$, information about the expectable quality of the reconstruction may be obtained from this Fréchet derivative.

Given the two finite element basis $\{\phi_i\}$ and $\{\psi_i\}$ of the data and the image space of $F$ used in the discretization of the inverse problem, the transfer matrix $T$ of the discretization of the Fréchet derivative of $F$ is given by

$$T_{i,j} := \left\langle\, F'(\sigma^\dagger)\phi_i, \psi_j \,\right\rangle_{L^2(\Omega)} \,. \tag{5.2}$$

In Section 7, we compute $T$ and its SVD for different boundary condition settings corresponding to various parts of the boundary being inaccessible for measurements. The resulting singular values and singular vectors are then analyzed and correlated to the obtained reconstructions for each considered setting.

# 6 Numerical Setting and Implementation Details

We now describe the precise setting of our numerical example problem. For the domain $\Omega$, we choose a unit disk in $2D$, i.e., in polar coordinates,

$$\Omega := \{(r, \theta) \in [0, 1) \times [0, 2\pi]\} .$$

For the accessible boundary $\Gamma_1$ we choose the family of subsets $\Gamma(\alpha) \subset \partial\Omega$ defined by

$$\Gamma(\alpha) := \{(r, \theta) \in \{1\} \times [0, \alpha]\} ,$$

and we set

$$g_j(r, \theta) := \sin\left(\frac{2j\pi\theta}{\alpha}\right) , \qquad \forall\, (r, \theta) \in \Gamma(\alpha) . \tag{6.1}$$

On the remaining part of the boundary, we always assume that $g_j = 0$. The resulting boundary functions $g_j$ are continuous on $\Gamma$ and satisfy

$$\int_{\partial\Omega} g_j \, dS = 0 ,$$

which implies that the compatibility condition (2.1) is satisfied. The trigonometric functions (6.1) are a natural choice for current density patterns [30]. Being normed, they represent elements of an orthonormal basis of the space $L^2(\Gamma(\alpha))$. Moreover, this choice of boundary functions guarantees a similar magnitude of the computed power densities $E_i$, which ensures that every power density contributes evenly to the reconstruction.

For the true conductivity $\sigma^\dagger$ we use the phantom depicted in Figure 6.1. It has a uniform background of value 1 as well as three inclusions: a big circle of value 2, a crescent of value 1.7 and a small circle of value 1.3, which are slightly smoothed towards their edges to conform with the smoothness requirements on $\sigma$. In order to implement this, we use 2D bump functions built from piecewise polynomial functions, where the polynomials are chosen in such a way that the resulting bump function is $C^2$.

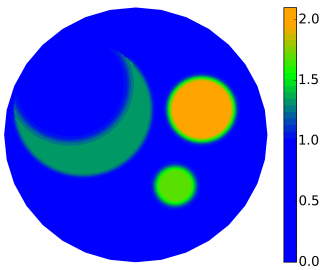


Figure 6.1: Exact value of the electrical conductivity $\sigma^\dagger$.

The discretization, implementation and computation of the involved variational problems was done using Python and the library FEniCS [1]. A triangulation with approximately 2000 vertices for discretizing the domain was used. This rather coarse choice of the discretization is due to time limitations in the computation of the SVD, since computing the matrix (5.2) already takes approximately 5 hours for this discretization level, see Section 7. The power density data $E(\sigma^\dagger)$ was created by applying the forward model to $\sigma^\dagger$ using a finer discretization with approximately 40000 vertices to avoid an inverse crime. The resulting power densities are depicted in Figures 6.2, 6.3, 6.4, for the angles $\alpha = 2\pi$, $\alpha = 3\pi/2$, and $\alpha = \pi$, respectively. The red circle (segment) in the figures indicate the available, i.e., non-zero, boundary. Accessibility of the boundary is reflected in the power densities: in Figure 6.2 we clearly see the internal structure such as the location of the inclusions, while in Figures 6.3 and 6.4 only some of it, but less than before, is visible. Furthermore, the potentials induced by the boundary functions $g_j$ for $j = 2, 3$ have a higher frequency and do not penetrate deep into the domain. Different random noise with a relative noise level of 5% is added to the power density to obtain the noisy data $E^\delta$, i.e., $E^\delta = E + \delta^{rel} \|E\| \tilde{e} / \|\tilde{e}\|$, where $\tilde{e}$ is a normally distributed random noise vector and $\delta^{rel}$ is the relative noise level. Obviously, with this choice one has an absolute noise in the data of $\delta = \delta^{rel} \|E\|$.

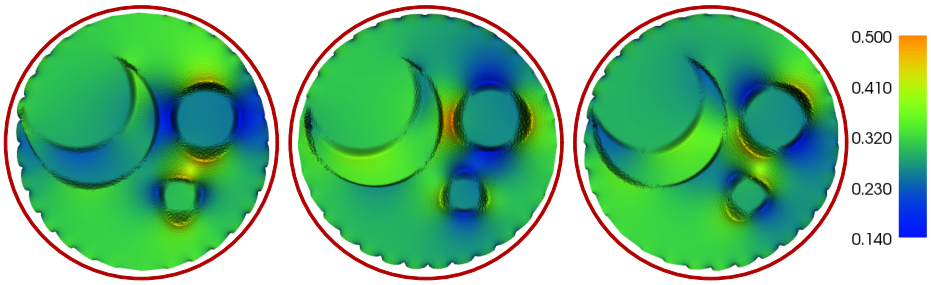


Figure 6.2: Power densities $E_j(\sigma^\dagger)$ with $\sigma^\dagger$ as in Figure 6.1 with boundary data $g_j$, $j = 1, 2, 3$ defined in (7.1) and $\alpha = 2\pi$ in $\Gamma(\alpha)$, i.e., 100% available boundary.

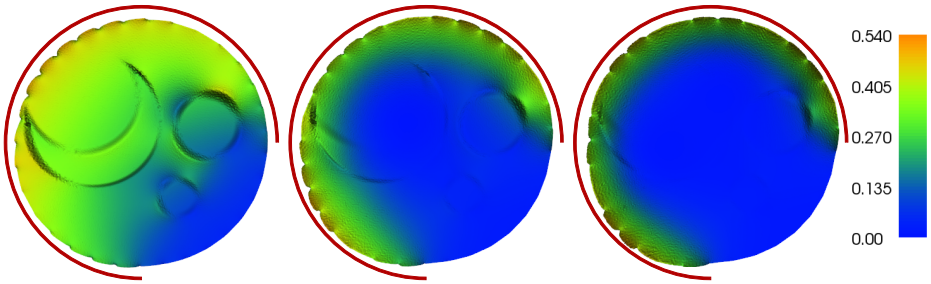


Figure 6.3: Power densities $E_j(\sigma^\dagger)$ with $\sigma^\dagger$ as in Figure 6.1 with boundary data $g_j$, $j = 1, 2, 3$ defined in (6.1) and $\alpha = 3\pi/2$ in $\Gamma(\alpha)$, i.e., 75% available boundary.

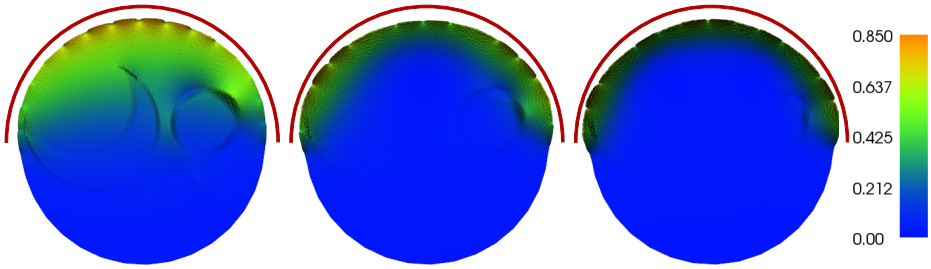


Figure 6.4: Power densities $E_j(\sigma^\dagger)$ with $\sigma^\dagger$ as in Figure 6.1 with boundary data $g_j$, $j = 1, 2, 3$ defined in (6.1) and $\alpha = \pi$ in $\Gamma(\alpha)$, i.e., 50% available boundary.

Since the domain $\Omega$ is two-dimensional, i.e., $N = 2$, by the above analysis we should choose $s > 2$ in the domain of $F$. However, since numerically there is hardly any difference between using $s = 2$ and $s = 2 + \varepsilon$ for $\varepsilon$ small enough, and since $s$ should be kept as small as possible to avoid unnecessary smoothness requirements for the exact conductivity $\sigma^\dagger$, we choose $s = 2$ for ease of implementation in the examples presented below. For obtaining the reconstructions, the steepest-descent Landweber method (4.1) together with the discrepancy principle (4.3) with the canonical choice $\tau = 1$ was used. For the initial guess, $\sigma_0 = 1.5$ was used throughout all tests.

Furthermore, in all cases additional reconstructions are presented where instead of using $E_s$ in the adjoint of the Fréchet derivative the operator $E_{s,\beta}$ defined by (3.7) was used with $s = 2$ and the choice $\beta_\alpha = 1, 10^{-3}, 10^{-6}$ for $|\alpha| = 0, 1, 2$, respectively. Moreover, we also present results in case that $E_s^*$ is dropped altogether in the reconstruction process, which can be seen as a preconditioning or in the light of regularization in Hilbert scales [31]. We refer to those cases as using the $H^2_\beta$ or the $L^2$ adjoint, while in the standard case we speak of using the $H^2$ adjoint.

# 7 Numerical Results

In this section we present various numerical results for different boundary value settings. Hereby, an emphasis is placed on the limited angle case, i.e., that $g = 0$ on the inaccessible boundary part $\partial\Omega \setminus \Gamma(\alpha)$. For ease of writing, we refer to these cases by the percentage value of the available boundary, e.g., we say that 75% of the boundary is available for measurements if $\alpha = 3\pi/2$. We consider the cases of 25%, 50%, 75%, and 100% available boundary in this section. Moreover, we present an ill-posedness quantification of the problem based on the singular value decomposition of the Fréchet derivative of $F$ in Section 5.

## 7.1 Reconstructions without Noise

Before considering the noisy data case of interest to us, we first present two examples where no noise was added to the data. Since the discrepancy principle is not a suitable stopping rule in case of no noise, the iteration has to be stopped differently. Due to computational limitations and since the iterative procedure does not make much progress from this point onwards, the iteration was stopped after 1000 iterations in both cases.

**Example 7.1.** As a first test we look at the reconstruction of the conductivity for a fully available Neumann boundary and three power density measurements. Contrary to all the other tests, here we have a different set of boundary functions, namely

$$g_1 = \sin(\theta)\,, \qquad g_2 = \cos(\theta)\,, \qquad g_3 = (\sin(\theta) + \cos(\theta))/\sqrt{2}\,.$$

After 1000 iterations we obtain the reconstructions for the $L^2$, $H^2_\beta$ and $H^2$ adjoint case depicted in Figure 7.1. The resulting reconstructions look rather similar, which is due to the fact that without noise, the residual $F(x) - y$ is already smooth and hence, the various smoothing properties of the different adjoints do not have much additional effect. However, they differ in the noisy case, where the $H^2_\beta$ adjoint performs somewhat better than the others (see Section 7.2).

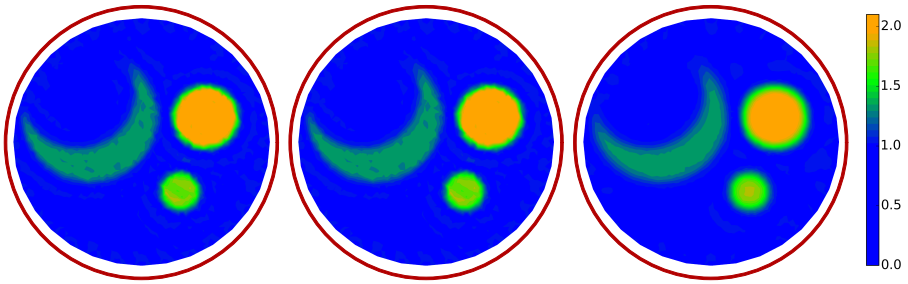


Figure 7.1: Reconstruction of conductivity $\sigma^\dagger$, Figure 6.1, with boundary data $g_j$, $j = 1, 2, 3$ defined in (7.1) and $\alpha = 2\pi$ in $\Gamma(\alpha)$, i.e., 100% available boundary. From left to right: $L^2$ adjoint, 1000 iterations; $H^2_\beta$ adjoint, 1000 iterations; $H^2$ adjoint, 1000 iterations.

**Example 7.2.** Following example 7.1 we present reconstructions for $75\%, 50\%, 25\%$ boundary available for measurements with boundary data $g_j$, $j = 1, 2, 3$ defined in (6.1) and $H^2_\beta$ adjoint, which are depicted in Figure 7.2.

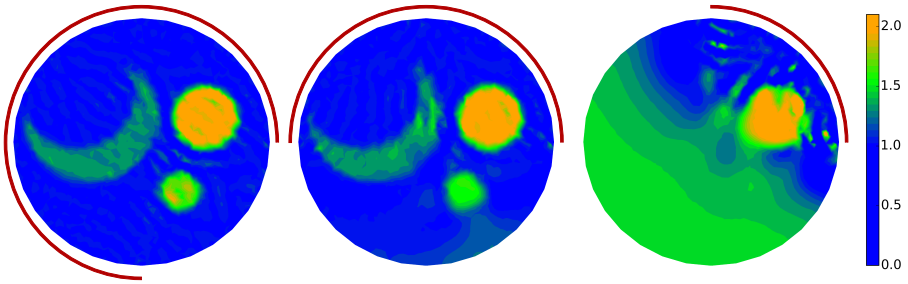


Figure 7.2: Reconstruction of conductivity $\sigma^\dagger$, Figure 6.1, with boundary data $g_j$, $j = 1, 2, 3$ defined in (6.1) and various angles in $\Gamma(\alpha)$. From left to right: $\alpha = 3\pi/2$, i.e., 75% available boundary, $H^2_\beta$ adjoint, 1000 iterations; $\alpha = \pi$, i.e., 50% available boundary, $H^2_\beta$ adjoint, 1000 iterations; $\alpha = \pi/2$, i.e., 25% available boundary, $H^2_\beta$ adjoint, 1000 iterations.

## 7.2 Reconstructions with Noise

After we saw in the previous section that reasonable reconstructions can be obtained in the case of noise-free data, in this section we focus on noisy data $E^\delta$ with a noise level of $\delta = 5\%$. Again the focus is on different limited angle cases.

**Example 7.3.** We consider 100% boundary available for measurements with boundary data $g_j$, $j = 1, 2, 3$ defined in (7.1). The iteration terminated after 3, 3 and 74

iterations for the $L^2$, $H^2_\beta$ and $H^2$ adjoint case, respectively, and yielded the reconstructions depicted in Figure 7.3. Even though the noise level is high, the conductivity $\sigma^\dagger$ is nicely reconstructed both in shape and quantity. The $L^2$ adjoint does not give enough smoothness on the solution, which is visible in the non-sharp edges of the inclusions. Due to the high noise level, the discrepancy principle stops the iteration very early, which affects the contrast of the reconstructions.

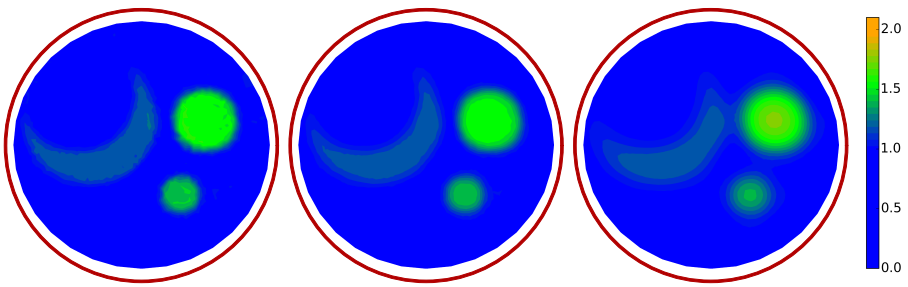


Figure 7.3: Reconstruction of conductivity $\sigma^\dagger$, Figure 6.1, with boundary data $g_j$, $j = 1, 2, 3$ defined in (7.1) and $\alpha = 2\pi$ in $\Gamma(\alpha)$, i.e., 100% available boundary. From left to right: $L^2$ adjoint, 3 iterations; $H^2_\beta$ adjoint, 3 iterations; $H^2$ adjoint, 74 iterations.

**Example 7.4.** Next we consider 75% boundary available for measurements with boundary data $g_j$, $j = 1, 2, 3$ defined in (6.1). In this case the iteration stops after 16, 10 and 177 steps for the $L^2$, $H^2_\beta$ and $H^2$ adjoints, respectively, which leads to the reconstructions depicted in Figure 7.4. As we can see, the missing data in the right bottom part of the power density in the Figures 6.3 transfers to the reconstructed conductivity through artefacts near the $\partial\Omega \setminus \Gamma(\alpha)$ boundary, where the background value and inclusions are not well reconstructed. Similarly to the previous example, the solution lacks smoothness with the $L^2$ adjoint, but captures more of the internal structure compared to the $H^2$ adjoint, which hardly detects the small circular inclusion. Meanwhile, the $H^2_\beta$ adjoint exhibits a good trade-off result between the other two.

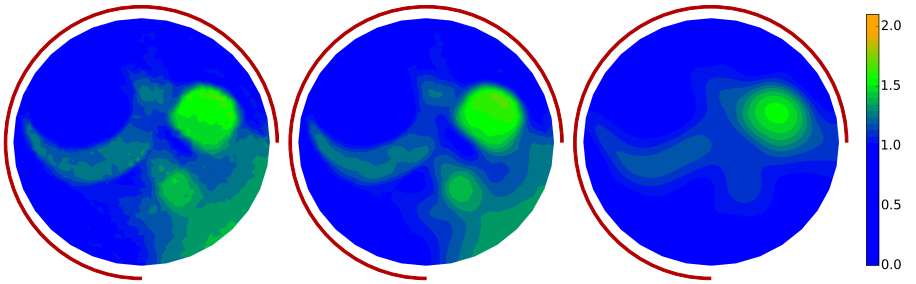


Figure 7.4: Reconstruction of conductivity $\sigma^\dagger$, Figure 6.1, with boundary data $g_j$, $j = 1, 2, 3$ defined in (6.1) and $\alpha = 3\pi/2$ in $\Gamma(\alpha)$, i.e., 75% available boundary. From left to right: $L^2$ adjoint, 16 iterations; $H^2_\beta$ adjoint, 10 iterations; $H^2$ adjoint, 177 iterations.

**Example 7.5.** For 50% available boundary and three measurements we obtain the reconstructions depicted in Figure 7.5. The discrepancy principle was satisfied after 44, 38 and 602 iterations for the $L^2$, $H^2_\beta$ and $H^2$ adjoints, respectively. In this test we see what happens when only half of the boundary is accessible and hence, half of the internal conductivity can be reconstructed, see Figure 6.4. The reconstructions are worse than in the previous examples, although we are able to obtain some information about the inclusions. The conductivity value of the big circle comes closer to the expected value and its shape remains almost proper, while the crescent is partly visible only. The small circular inclusion cannot be reconstructed due to the lack of information in this area.

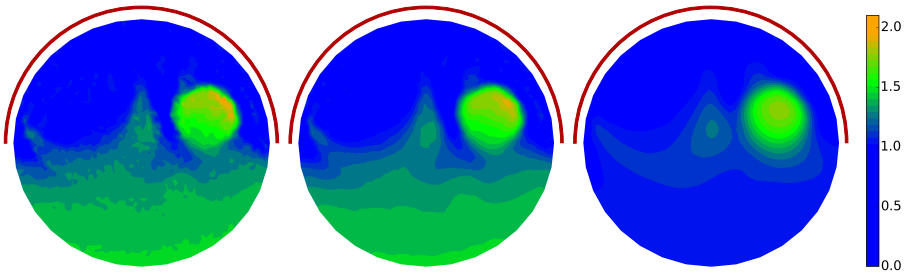


Figure 7.5: Reconstruction of conductivity $\sigma^\dagger$, Figure 6.1, with boundary data $g_j$, $j = 1, 2, 3$ defined in (6.1) and $\alpha = \pi$ in $\Gamma(\alpha)$, i.e., 50% available boundary. From left to right: $L^2$ adjoint, 44 iterations; $H^2_\beta$ adjoint, 38 iterations; $H^2$ adjoint, 602 iterations.

**Example 7.6.** As a last test we consider an available boundary of only 25% with three measurements. We obtain the reconstructions depicted in Figure 7.6 after 1000 iterations (the iteration was terminated even though the discrepancy principle was not reached due to time limitations). We can recover the big circle inclusion located close to the accessible boundary with some artefacts notable around it for the cases of the

$L^2$ and $H^2_\beta$ adjoints. The $H^2$ adjoint smooths the artefacts in the solution. However, quantitatively, the inclusion has a higher contrast than in the previous examples with noise.

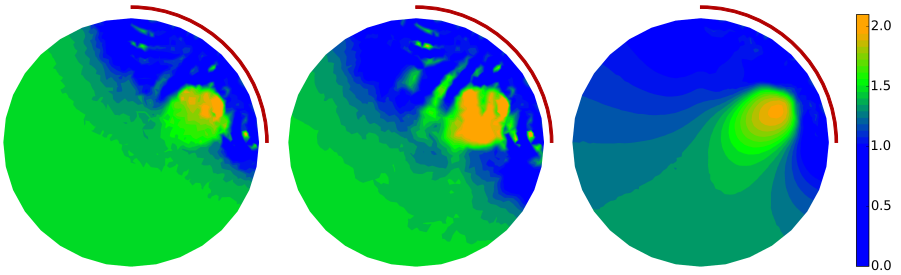


Figure 7.6: Reconstruction of conductivity $\sigma^\dagger$, Figure 6.1, with boundary data $g_j$, $j = 1, 2, 3$ defined in (6.1) and $\alpha = \pi/2$ in $\Gamma(\alpha)$, i.e., 25% available boundary. From left to right: $L^2$ adjoint, 1000 iterations; $H^2_\beta$ adjoint, 1000 iterations; $H^2$ adjoint, 1000 iterations.

## 7.3 Results of the Ill-Posedness Quantification

In this section, we present some results from the ill-posedness quantification introduced in Section 5 and show that the varying reconstruction results obtained for the different limited angle cases nicely correspond to certain pairs of singular values and vectors obtained from the SVD of $T$.

First, we look at the condition numbers of $T$ for different limited angles and numbers of power density measurements, which are given in Table 7.7. The transfer matrix $T$ becomes more and more ill-conditioned with decreasing angle and number of measurements, and therefore, we should not expect good reconstructions, especially further away from the accessible boundary. Additionally, we can see that using two measurements instead of one reduces the condition number of $T$ drastically, which should be compared with the identifiability results discussed in Section 3.2. However, the third measurement does not reduce the condition number and therefore obtaining reasonable reconstructions with two measurements promises good reconstruction results as well, and with a shorter computational time.

| Number of measurements | Limited angle, % | | | |
|---|---|---|---|---|
| | 100 | 75 | 50 | 25 |
| 3 | $1.5 \cdot 10^1$ | $3.8 \cdot 10^2$ | $3.6 \cdot 10^3$ | $8.8 \cdot 10^4$ |
| 2 | $1.5 \cdot 10^1$ | $3.7 \cdot 10^2$ | $3.4 \cdot 10^3$ | $8.1 \cdot 10^4$ |
| 1 | $4.6 \cdot 10^3$ | $6.4 \cdot 10^3$ | $1.8 \cdot 10^5$ | $4.5 \cdot 10^6$ |

Table 7.7: Condition numbers of the matrix $T$.

The singular values for different limited angle cases are depicted in Figure 7.8, which shows a decrease of the smallest singular values with the available angle, and as expected the problem becomes more ill-posed with less data.

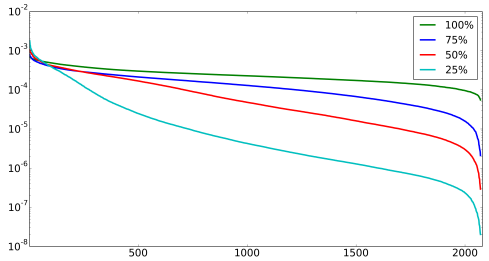


Figure 7.8: Singular values for 100%, 75%, 50% and 25% available boundary with three measurements.

Moreover, in Figure 7.9 we observe a similar decrease of the singular values depending on the number of measurements, thus confirming our conclusions about condition numbers.

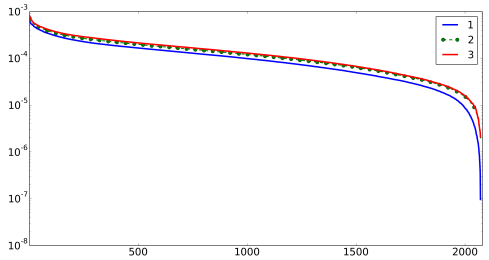


Figure 7.9: Singular values for 75% available boundary depending on the number of measurements.

A selection of the resulting singular vectors for the Examples 7.4, 7.5 and 7.6 is depicted in Figures 7.10, 7.11 and 7.12, respectively. The ordering of the singular values and singular vectors, denoted by $v_i$, is done in the common way, i.e., the singular values are arranged in descending order, from the largest to the smallest, and the singular vector $v_1$ belongs to the largest singular value.

We see that different singular vectors carry information about the true conductivity $\sigma^\dagger$ in different areas of the domain. Unfortunately for the reconstruction, the singular vectors containing information about the area close to the inaccessible boundary correspond to small singular values. Since regularization methods have to rely on the singular vectors corresponding to larger singular values for a stable reconstruction, this adds to the explanation of the fact that close to the inaccessible boundary, the conductivity $\sigma^\dagger$ cannot be reconstructed.

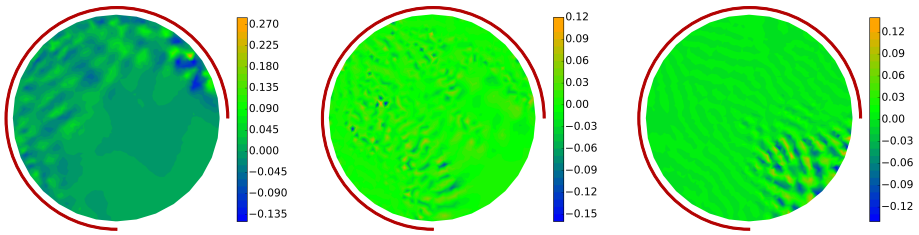


Figure 7.10: Singular vectors from $\sigma^\dagger$, Figure 6.1, with boundary conditions $g_j$, $j = 1, 2, 3$ defined in (6.1) and $\alpha = 2\pi/3$ in $\Gamma(\alpha)$, i.e., 75% available boundary. From left to right: $v_{100}$, $v_{1000}$, $v_{2060}$.

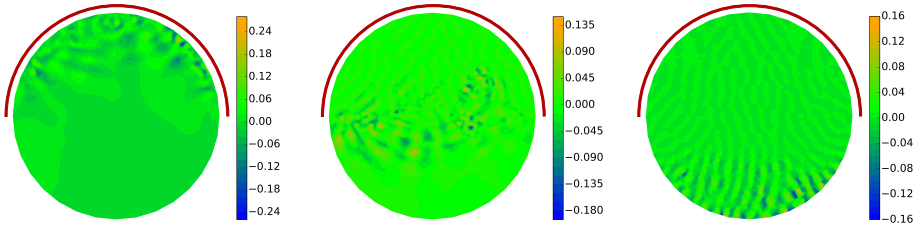


Figure 7.11: Singular vectors from $\sigma^\dagger$, Figure 6.1, with boundary conditions $g_j$, $j = 1, 2, 3$ defined in (6.1) and $\alpha = \pi$ in $\Gamma(\alpha)$, i.e., 50% available boundary. From left to right: $v_{100}$, $v_{1000}$, $v_{2060}$.

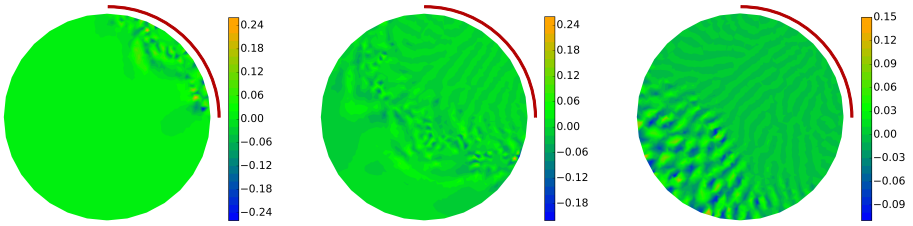


Figure 7.12: Singular vectors from $\sigma^\dagger$, Figure 6.1, with boundary conditions $g_j$, $j = 1, 2, 3$ defined in (6.1) and $\alpha = \pi/2$ in $\Gamma(\alpha)$, i.e., 25% available boundary. From left to right: $v_{100}$, $v_{1000}$, $v_{2060}$.

# 8 Conclusions

We formulated the hybrid imaging problem of estimating a spatially varying conductivity $\sigma$ from measurements of power densities resulting from different prescribed boundary

currents in an infinite dimensional setting and presented various numerical results, focusing especially on the limited angle case. In particular, we saw that reconstructing the conductivity is difficult far away from the accessible part of the boundary, due to lack of information in this area. Through a numerical ill-posedness quantification, we were able to establish a close connection between the reconstruction quality and the SVD of the Fréchet derivative of $F$. As the size of the accessible boundary becomes smaller, the reconstruction quality deteriorates, which is confirmed by a rapid decay of the corresponding singular values. The degree of ill-posedness of the linearized problem decreases with the number of used measurements and the size of the accessible boundary. The obtained results shed some light on the influence of limited angle data in hybrid tomography, clearly illustrating the possibilities and limitations of those methods in numerical practise.

# 9 Support and Acknowledgements

ES was funded by the Danish Council for Independent Research - Natural Sciences: grant 4002-00123. SH was funded by the Austrian Science Fund (FWF): W1214-N15, project DK8. The authors would like to acknowledge the M.Sc. work of Christina Hilderbrandt, which includes early ideas on ill-posedness quantification for the limited angle problem with Dirichlet boundary conditions.

# References

[1] M. S. Alnæs, J. Blechta, J. Hake, A. Johansson, B. Kehlet, A. Logg, C. Richardson, J. Ring, M. E. Rognes, and G. N. Wells. The FEniCS Project Version 1.5. *Archive of Numerical Software*, 3(100), 2015.

[2] H. Ammari, E. Bonnetier, Y. Capdeboscq, M. Tanter, and M. Fink. Electrical impedance tomography by elastic deformation. *SIAM Journal on Applied Mathematics*, 68(6):1557–1573, 2008.

[3] H. Ammari, J. Garnier, and W. Jing. Resolution and stability analysis in acousto-electric imaging. *Inverse Problems*, 28(8):084005, 2012.

[4] G. Bal. Cauchy problem for ultrasound-modulated eit. *Analysis and PDE*, 6(4):751–775, 2013.

[5] G. Bal, E. Bonnetier, F. Monard, and F. Triki. Inverse diffusion from knowledge of power densities. *Inverse Problems and Imaging*, 7(2):353–375, 2013.

[6] G. Bal, K. Hoffmann, and K. Knudsen. Propagation of singularities for linearised hybrid data impedance tomography. *Inverse Problems*, 34(2):024001, 2017.

[7] G. Bal, W. Naetar, O. Scherzer, and J. Schotland. The Levenberg-Marquardt iteration for numerical inversion of the power density operator. *J. Inv. Ill-Posed Problems*, 21(2):265–280, 2013.

[8] A. Bukhgeim and G. Uhlmann. Recovering a potential from partial cauchy data. *Communications in Partial Differential Equations*, 27(3-4):653–668, 2002.

[9] Y. Capdeboscq. On a counter-example to quantitative Jacobian bounds. *J. Éc. polytech. Math.*, 2:171–178, 2015.

[10] Y. Capdeboscq, J. Fehrenbach, F. de Gournay, and O. Kavian. Imaging by modification: Numerical reconstruction of local conductivities from corresponding power density measurements. *SIAM Journal on Imaging Sciences*, 2(4):1003–1030, 2009.

[11] P. Caro, D. Dos Santos Ferreira, and A. Ruiz. Stability estimates for the Calderón problem with partial data. *Journal of Differential Equations*, 260(3):2457–2489, 2016.

[12] H. W. Engl, M. Hanke, and A. Neubauer. *Regularization of inverse problems.* Dordrecht: Kluwer Academic Publishers, 1996.

[13] H. W. Engl, K. Kunisch, and A. Neubauer. Convergence rates for tikhonov regularisation of non-linear ill-posed problems. *Inverse Problems*, 5(4):523, 1989.

[14] B. Gebauer and O. Scherzer. Impedance-acoustic tomography. *SIAM Journal on Applied Mathematics*, 69(2):565–576, 2008.

[15] D. Gilbarg and N. S. Trudinger. *Elliptic partial differential equations of second order*. Grundlehren der mathematischen Wissenschaften. Springer, 1998.

[16] A. S. Giovanni, G. Bal, and M. Di Cristo. Critical points for elliptic equations with prescribed boundary conditions. *Archive for Rational Mechanics and Analysis*, 226(1):117–141, 2017.

[17] K. Hoffmann and K. Knudsen. Iterative reconstruction methods for hybrid inverse problems in impedance tomography. *Sensing and Imaging*, 15(96):1–27, 2014.

[18] D. S. Holder. *Electrical Impedance Tomography: Methods, History and Applications*. Boca Raton: CRC Press, 2005.

[19] O. Yu. Imanuvilov, G. Uhlmann, and M. Yamamoto. The Calderón problem with partial data in two dimensions. *Journal of the American Mathematical Society*, 23(3):655–691, 2010.

[20] V. Isakov. *Inverse Problems for Partial Differential Equations.* Applied Mathematical Sciences. Springer, New York, NY, 2006.

[21] B. Kaltenbacher, A. Neubauer, and O. Scherzer. *Iterative regularization methods for nonlinear ill-posed problems.* Berlin: de Gruyter, 2008.

[22] K. Karhunen, A. Seppänen, A. Lehikoinen, J. Blunt, J. P. Kaipio, and P. J. M. Monteiro. Electrical resistance tomography for assessment of cracks in concrete. *Materials Journal*, 107(5):523–531, 2010.

[23] K. Karhunen, A. Seppänen, A. Lehikoinen, P. J. M. Monteiro, and J. P. Kaipio. Electrical resistance tomography imaging of concrete. *Cement and Concrete Research*, 40:137–145, 2010.

[24] C. E. Kenig, J. Sjöstrand, and G. Uhlmann. The Calderón problem with partial data. *Annals of Mathematics*, 165(2):567–591, 2007.

[25] K. Knudsen. The Calderón problem with partial data for less smooth conductivities. *Communications in Partial Differential Equations*, 31(1):57–71, 2006.

[26] P. Kuchment and L. Kunyansky. Synthetic focusing in ultrasound modulated tomography. *Inverse Problems and Imaging*, 4(4):665–673, 2010.

[27] N. Mandache. Exponential instability in an inverse problem for the Schrödinger equation. *Inverse Problems*, 17(5):1435–1444, 2001.

[28] F. Monard and G. Bal. Inverse anisotropic diffusion from power density measurements in two dimensions. *Inverse Problems*, 28(8):084001, 2012.

[29] V. A. Morozov. *Methods for Solving Incorrectly Posed Problems*. Springer-Verlag New York, 1984.

[30] J. Mueller and S. Siltanen. *Linear and Nonlinear Inverse Problems with Practical Applications*. Society for Industrial and Applied Mathematics, Philadelphia, PA, 2012.

[31] A. Neubauer. On Landweber iteration for nonlinear ill-posed problems in Hilbert scales. *Numer. Math.*, 85(2):309–328, 2000.

[32] O. Scherzer. A convergence analysis of a method of steepest descent and a two-step algorithm for nonlinear ill-posed problems. *Numerical Functional Analysis and Optimization*, 17(1-2):197–214, 1996.

[33] E. Schock. Nonlinear Ill-Posed Problems, Three Counterexamples. *Inverse Problems*, 18:715–717, 2002.

[34] J. K. Seo and E. J.Woo. Magnetic resonance electrical impedance tomography (mreit). *Siam Review*, 53(1):40–68, 2011.

[35] H. Zhang and L. V. Wang. Acousto-electric tomography. *Proceedings SPIE, Photons Plus Ultrasound: Imaging and Sensing*, 5320(9):145–149, 2004.

# Paper B

---

**Lamé Parameter Estimation from Static Displacement Field Measurements in the Framework of Nonlinear Inverse Problems**

---

| | |
|---|---|
| Type | Submitted manuscript (2017) |
| Authors | Simon Hubmer, Ekaterina Sherina, Andreas Neubauer and Otmar Scherzer |
| Available from | https://arxiv.org/abs/1710.10446 |

# Lamé Parameter Estimation from Static Displacement Field Measurements in the Framework of Nonlinear Inverse Problems

Simon Hubmer*, Ekaterina Sherina†, Andreas Neubauer‡, Otmar Scherzer§¶

October 31, 2017

**Abstract**

The problem of estimating Lamé parameters from full internal static displacement field measurements is formulated as a nonlinear operator equation. The Fréchet derivative and the adjoint of the nonlinear operator are derived. The main theoretical result is the verification of a nonlinearity condition guaranteeing convergence of iterative regularization methods, which is proven in an infinite dimensional context. Furthermore, numerical examples for recovery of the Lamé parameters from simulated displacement data are presented, simulating a static elastography experiment.

**Keywords:** Elastography, Inverse Problems, Nonlinearity Condition, Linearized Elasticity, Lamé Parameters, Parameter Identification, Landweber Iteration

**AMS:** 65J22, 65J15, 74G75

## 1 Introduction

The inverse problem of quantitative elastography consists in estimating material parameters from measurements of displacement data.

In this paper we assume that the model of linearized elasticity, describing the relation between forces and displacements, is valid. Then, quantitative elastography

*Johannes Kepler University Linz, Doctoral Program Computational Mathematics, Altenbergerstraße 69, A-4040 Linz, Austria (simon.hubmer@dk-compmath.jku.at), corresponding author.

†Technical University of Denmark, Department of Applied Mathematics and Computer Science, Asmussens Allé, 2800 Kongens Lyngby, Denmark (sershe@dtu.dk)

‡Johannes Kepler University Linz, Industrial Mathematics Institute, Altenbergerstraße 69, A-4040 Linz, Austria (neubauer@indmath.uni-linz.ac.at)

§University of Vienna, Computational Science Center, Oskar Morgenstern-Platz 1, 1090 Vienna, Austria (otmar.scherzer@univie.ac.at)

¶Johann Radon Institute Linz, Altenbergerstraße 69, A-4040 Linz, Austria (otmar.scherzer@univie.ac.at)

consists in estimating the spatially varying *Lamé parameters* $\lambda, \mu$ from displacement field measurements $u$ induced by external forces.

There exist a vast amount of literature on identifiability of the Lamé parameters, stability, and different reconstruction methods. See for example [6,8–11,14,15,18,20,22, 25,26,30–32,37,38,43] and the references therein. Many of the above works deal with the time-dependent equations of linearized elasticity, since the resulting inverse problem is arguably more stable and better to solve. However, in many application including the ones we have in mind, no dynamic, i.e., time-dependent displacement field data is available and hence, one has to work with the static elasticity equations.

In this paper we consider the inverse problem of identifying the Lamé parameters from *static* displacement field measurements. We reformulate this problem as a nonlinear operator equation

$$F(\lambda, \mu) = u\,, \tag{1.1}$$

and provide the Fréchet derivative and its adjoint of $F$. For *dynamic* measurement data of the displacement field $u$, similar investigation have been performed in [30,31].

The main result of this paper is the verification of the *(strong) nonlinearity condition* [21] in an infinite dimensional setting, which is the basic assumption guaranteeing convergence of iterative regularization methods. Finally, we present some sample reconstructions with iterative regularization methods from numerically simulated displacement field data.

# 2 Mathematical Model of Linearized Elasticity

In this section we introduce the basic notation and recall the basic equation of linearized elasticity:

**Notation.** $\Omega$ denotes a non-empty bounded, open and connected set in $\mathbb{R}^N$, $N = 1, 2, 3$, with a Lipschitz continuous boundary $\partial\Omega$, which has two subsets $\Gamma_D$ and $\Gamma_T$, satisfying $\partial\Omega = \overline{\Gamma_D \cup \Gamma_T}$, $\Gamma_D \cap \Gamma_T = \emptyset$ and $\operatorname{meas}(\Gamma_D) > 0$.

**Definition 2.1.** Given body forces $f$, displacement $g_D$, surface traction $g_T$ and Lamé parameters $\lambda$ and $\mu$, the forward problem of linearized elasticity with displacement-traction boundary conditions consists in finding $\tilde{u}$ satisfying

$$\begin{aligned} -\operatorname{div}(\sigma(\tilde{u})) &= f\,, \quad \text{in } \Omega\,, \\ \tilde{u}\,|_{\Gamma_D} &= g_D\,, \\ \sigma(\tilde{u})\vec{n}\,|_{\Gamma_T} &= g_T\,, \end{aligned} \tag{2.1}$$

where $\vec{n}$ is an outward unit normal vector of $\partial\Omega$ and the stress tensor $\sigma$ defining the stress-strain relation in $\Omega$ is defined by

$$\sigma(u) := \lambda\ \operatorname{div}(u)\, I + 2\mu\ \mathcal{E}(u)\ , \qquad \mathcal{E}(u) := \frac{1}{2}\left(\nabla u + \nabla u^T\right)\ , \tag{2.2}$$

where $I$ is the identity matrix and $\mathcal{E}$ is called the strain tensor.

It is convenient to homogenize problem (2.1) in the following way: Taking a $\Phi$ such that $\Phi|_{\Gamma_D} = g_D$, one then seeks $u := \tilde{u} - \Phi$ such that

$$\begin{aligned} -\operatorname{div}(\sigma(u)) &= f + \operatorname{div}(\sigma(\Phi)), \quad \text{in } \Omega, \\ u\,|_{\Gamma_D} &= 0, \\ \sigma(u)\vec{n}\,|_{\Gamma_T} &= g_T - \sigma(\Phi)\vec{n}\,|_{\Gamma_T}. \end{aligned} \tag{2.3}$$

Throughout this paper, we make the following

**Assumption 2.1.** Let $f \in H^{-1}(\Omega)^N$, $g_D \in H^{\frac{1}{2}}(\Gamma_D)^N$, and $g_T \in H^{-\frac{1}{2}}(\Gamma_T)^N$. Furthermore, let $\Phi \in H^1(\Omega)^N$ be such that $\Phi|_{\Gamma_D} = g_D$.

Since we want to consider weak solutions of (2.3), we make the following

**Definition 2.2.** Let Assumption 2.1 hold. We define the space

$$V := H^1_{0,\Gamma_D}(\Omega)^N, \qquad \text{where} \qquad H^1_{0,\Gamma_D}(\Omega) := \{u \in H^1(\Omega) \,|\, u|_{\Gamma_D} = 0\},$$

the linear form

$$l(v) := \langle f, v \rangle_{H^{-1}(\Omega), H^1(\Omega)} + \langle g_T, v \rangle_{H^{-\frac{1}{2}}(\Gamma_T), H^{\frac{1}{2}}(\Gamma_T)}, \tag{2.4}$$

and the bilinear form

$$a_{\lambda,\mu}(u,v) := \int_\Omega (\lambda \operatorname{div}(u) \operatorname{div}(v) + 2\mu\, \mathcal{E}(u) : \mathcal{E}(v))\, dx, \tag{2.5}$$

where the expression $\mathcal{E}(u) : \mathcal{E}(v)$ denotes the Frobenius product of the matrices $\mathcal{E}(u)$ and $\mathcal{E}(v)$, which also induces the Frobenius norm $\|\mathcal{E}(u)\|_F := \sqrt{\mathcal{E}(u) : \mathcal{E}(u)}$.

Note that both $a_{\lambda,\mu}(u,v)$ and $l(v)$ are also well defined for $u, v \in H^1(\Omega)^N$.

**Definition 2.3.** A function $u \in V$ satisfying the variational problem

$$a_{\lambda,\mu}(u,v) = l(v) - a_{\lambda,\mu}(\Phi, v), \qquad \forall\, v \in V, \tag{2.6}$$

is called a weak solution of the linearized elasticity problem (2.3).

From now on, we only consider weak solutions of (2.3) in the sense of Definition 2.3.

**Definition 2.4.** The set $\mathcal{M}(\underline{\mu})$ of admissible Lamé parameters is defined by

$$\mathcal{M}(\underline{\mu}) := \left\{ (\lambda,\mu) \in L^\infty(\Omega)^2 \,|\, \exists\, 0 < \varepsilon \le \frac{\underline{\mu}\, c_K^2}{N + 2c_K^2} \,:\, \lambda \ge -\varepsilon,\, \mu \ge \underline{\mu} - \varepsilon > 0 \right\}.$$

Concerning existence and uniqueness of weak solutions, we get the following

**Theorem 2.1.** *Let the Assumption 2.1 hold and assume that the Lamé parameters* $(\lambda, \mu) \in \mathcal{M}(\underline{\mu})$ *for some* $\underline{\mu} > 0$*. Then there exists a unique weak solution* $u \in V$ *of* (2.3)*. Moreover, there exists a constant* $c_{LM} > 0$ *such that*

$$\|u\|_{H^1(\Omega)} \leq c_{LM}\Big( \|f\|_{H^{-1}(\Omega)} + c_T \|g_T\|_{H^{-\frac{1}{2}}(\Gamma_T)} + \Big(N \|\lambda\|_{L^\infty(\Omega)} + 2\|\mu\|_{L^\infty(\Omega)}\Big) \|\Phi\|_{H^1(\Omega)} \Big).$$

*Proof.* Using the Cauchy-Schwarz inequality yields

$$|a_{\lambda,\mu}(u,v)| \leq \Big(N \|\lambda\|_{L^\infty(\Omega)} + 2\|\mu\|_{L^\infty(\Omega)}\Big) \|u\|_{H^1(\Omega)} \|v\|_{H^1(\Omega)} , \tag{2.7}$$

for all $u, v \in H^1(\Omega)^N$. From this and the trace inequality (5.1), it follows that $L(v) := l(v) - a_{\lambda,\mu}(\Phi, v)$ satisfies the estimate:

$$\begin{aligned} &|L(v)| \leq |l(v)| + |a_{\lambda,\mu}(\Phi, v)| \\ &\leq \Big( \|f\|_{H^{-1}(\Omega)} + c_T \|g_T\|_{H^{-\frac{1}{2}}(\Gamma_T)} + \Big(N \|\lambda\|_{L^\infty(\Omega)} + 2\|\mu\|_{L^\infty(\Omega)}\Big) \|\Phi\|_{H^1(\Omega)} \Big) \|v\|_{H^1(\Omega)} . \end{aligned}$$

Since $(\lambda, \mu) \in \mathcal{M}(\underline{\mu})$, there exists an $0 < \varepsilon \leq (\underline{\mu}\, c_K^2)/(N + 2c_K^2)$ such that $\lambda \geq -\varepsilon$ and $\mu \geq \underline{\mu} - \varepsilon > 0$. Together with Korn's inequality (5.4) and (5.3), for all $v \in V$ we have

$$\begin{aligned} a_{\lambda,\mu}(v,v) &= \int_\Omega \lambda(\operatorname{div}(v))^2 + 2\mu \|\mathcal{E}(v)\|_F^2 \, dx \\ &\geq \big(-\varepsilon N + 2(\underline{\mu} - \varepsilon)\big) \int_\Omega \|\mathcal{E}(v)\|_F^2 \, dx \geq \underline{\mu}\, c_K^2 \|\nabla v\|_{L^2(\Omega)}^2 \geq \frac{\underline{\mu}\, c_K^2}{1 + c_F^2} \|v\|_{H^1(\Omega)}^2 , \end{aligned}$$

which shows the coercivity of $a_{\lambda,\mu}$. Hence, the assertion follows from the Lax-Milgram Lemma applied to $a_{\lambda,\mu}$ and $L$ with $c_{LM} = (1 + c_F^2)/(\underline{\mu}\, c_K^2)$. □

# 3 The Inverse Problem

After considering the forward problem of linearized elasticity, we now turn to the inverse problem, which is to estimate the Lamé parameters $\lambda, \mu$ by measurements of the displacement field $u$. More precisely, we are facing the following

**Problem.** *Let Assumption 2.1 hold and let* $u^\delta \in L^2(\Omega)^N$ *be a measurement of the true displacement field* $u$ *satisfying*

$$\big\|u - u^\delta\big\|_{L^2(\Omega)} \leq \delta , \tag{3.1}$$

*where* $\delta \geq 0$ *is the noise level. Given the model of linearized elasticity* (2.1) *in the weak form* (2.6)*, the problem is to find the Lamé parameters* $\lambda, \mu$*.*

The problem of linearized elastography can be formulated as the solution of the operator equation (1.1) with the operator

$$\begin{aligned} F : \mathcal{D}(F) := \left\{ (\lambda, \mu) \in L^\infty(\Omega)^2 \,|\, \lambda \geq 0\,,\ \mu \geq \underline{\mu} > 0 \right\} &\to L^2(\Omega)^N\,, \\ (\lambda, \mu) &\mapsto u(\lambda, \mu)\,, \end{aligned} \tag{3.2}$$

where $u(\lambda, \mu)$ is the solution of (2.6) and hence, we can apply all results from classical inverse problems theory [16], given that the necessary requirements on $F$ hold. For showing them, it is necessary to write $F$ in a different way: We define the space

$$V^* := \left( H^1_{0,\Gamma_D}(\Omega)^N \right)^*\,, \tag{3.3}$$

which is the dual space of $V = H^1_{0,\Gamma_D}(\Omega)^N$. Next, we introduce the operator $\tilde{A}_{\lambda,\mu}$ connected to the bilinear form $a_{\lambda,\mu}$, defined by

$$\begin{aligned} \tilde{A}_{\lambda,\mu} :\ H^1(\Omega)^N &\to V^*\,, \\ \tilde{v} &\mapsto (v \mapsto a_{\lambda,\mu}(\tilde{v}, v))\ , \end{aligned} \tag{3.4}$$

and its restriction to $V$, i.e., $A := \tilde{A}|_V$, namely

$$\begin{aligned} A_{\lambda,\mu} :\ V &\to V^*\,, \\ v &\mapsto (\bar{v} \mapsto a_{\lambda,\mu}(v, \bar{v}))\ . \end{aligned} \tag{3.5}$$

Furthermore, for $v \in V$ and $v^* \in V^*$, we define the canonical dual

$$\langle\, v^*, v \,\rangle_{V^*,V} = \langle\, v, v^* \,\rangle_{V,V^*} := v^*(v)\,.$$

Next, we collect some important properties of $\tilde{A}_{\lambda,\mu}$ and $A_{\lambda,\mu}$. For ease of notation,

$$\left\| (\bar{\lambda}, \bar{\mu}) - (\lambda, \mu) \right\|_\infty := N \left\| \bar{\lambda} - \lambda \right\|_{L^\infty(\Omega)} + 2 \left\| \bar{\mu} - \mu \right\|_{L^\infty(\Omega)}\ . \tag{3.6}$$

**Proposition 3.1.** *The operators $\tilde{A}_{\lambda,\mu}$ and $A_{\lambda,\mu}$ defined by* (3.4) *and* (3.5)*, respectively, are bounded and linear for all $\lambda, \mu \in L^\infty(\Omega)$. In particular, for all $\lambda, \mu, \bar{\lambda}, \bar{\mu} \in L^\infty(\Omega)$*

$$\left\| A_{\bar{\lambda},\bar{\mu}} - A_{\lambda,\mu} \right\|_{V,V^*} \leq \left\| \tilde{A}_{\bar{\lambda},\bar{\mu}} - \tilde{A}_{\lambda,\mu} \right\|_{H^1(\Omega),V^*} \leq \left\| (\bar{\lambda}, \bar{\mu}) - (\lambda, \mu) \right\|_\infty\ . \tag{3.7}$$

*Furthermore, for all $(\lambda, \mu) \in \mathcal{M}(\underline{\mu})$ with $\underline{\mu} > 0$, the operator $A_{\lambda,\mu}$ is bijective and has a continuous inverse $A^{-1}_{\lambda,\mu} : V^* \to V$ satisfying $\left\| A^{-1}_{\lambda,\mu} \right\|_{V^*,V} \leq c_{LM}$. In particular, for all $v^*, \bar{v}^* \in V^*$ and $(\lambda, \mu), (\bar{\lambda}, \bar{\mu}) \in \mathcal{M}(\underline{\mu})$*

$$\left\| A^{-1}_{\bar{\lambda},\bar{\mu}} \bar{v}^* - A^{-1}_{\lambda,\mu} v^* \right\|_V \leq c_{LM} \left( \left\| (\bar{\lambda}, \bar{\mu}) - (\lambda, \mu) \right\|_\infty \left\| A^{-1}_{\lambda,\mu} v^* \right\|_V + \left\| \bar{v}^* - v^* \right\|_{V^*} \right)\ . \tag{3.8}$$

*Proof.* The boundedness and linearity of $A_{\lambda,\mu}$ and $\tilde{A}_{\lambda,\mu}$ for all $\lambda, \mu \in L^\infty(\Omega)$ are immediate consequences of the boundedness and bilinearity of $a_{\lambda,\mu}$ and we have

$$\left\|\tilde{A}_{\lambda,\mu} - \tilde{A}_{\bar{\lambda},\bar{\mu}}\right\|_{H^1(\Omega),V^*} = \left\|\tilde{A}_{\bar{\lambda}-\lambda,\bar{\mu}-\mu}\right\|_{H^1(\Omega),V^*} = \sup_{u\in H^1(\Omega),u\neq 0} \frac{\left\|\tilde{A}_{\bar{\lambda}-\lambda,\bar{\mu}-\mu}u\right\|_{V^*}}{\|u\|_{H^1(\Omega)}}$$
$$= \sup_{u\in H^1(\Omega),u\neq 0} \frac{\sup_{v\in V,v\neq 0}\left|a_{\bar{\lambda}-\lambda,\bar{\mu}-\mu}(u,v)\right|}{\|u\|_{H^1(\Omega)}\|v\|_V} \leq \left\|(\bar{\lambda},\bar{\mu})-(\lambda,\mu)\right\|_\infty ,$$

which also translates to $A_{\lambda,\mu}$, since $V \subset H^1(\Omega)^N$. Moreover, due to the Lax-Milgram Lemma and Theorem 2.1, $A_{\lambda,\mu}$ is bijective for $(\lambda,\mu) \in \mathcal{M}(\underline{\mu})$ with $\underline{\mu} > 0$ and therefore, by the Open Mapping Theorem, $A^{-1}_{\lambda,\mu}$ exists and is linear and continuous. Again by the Lax-Milgram Lemma, there follows $\left\|A^{-1}_{\lambda,\mu}\right\|_{V^*,V} \leq c_{LM}$.

Let $v^*, \bar{v}^* \in V^*$ and $(\lambda,\mu),(\bar{\lambda},\bar{\mu}) \in \mathcal{M}(\underline{\mu})$ with $\underline{\mu} > 0$ be arbitrary but fixed and consider $u := A^{-1}_{\lambda,\mu}v^*$ and $\bar{u} := A^{-1}_{\bar{\lambda},\bar{\mu}}\bar{v}^*$. Subtracting those two equations, we get

$$A_{\lambda,\mu}u - A_{\bar{\lambda},\bar{\mu}}\bar{u} = v^* - \bar{v}^* ,$$

which, by the definition of $A_{\lambda,\mu}$ and $a_{\lambda,\mu}$, can be written as

$$A_{\bar{\lambda},\bar{\mu}}\,(u-\bar{u}) = A_{\bar{\lambda}-\lambda,\bar{\mu}-\mu}u + v^* - \bar{v}^* .$$

and is equivalent to the variational problem

$$a_{\bar{\lambda},\bar{\mu}}\,((u-\bar{u}),v) = a_{\bar{\lambda}-\lambda,\bar{\mu}-\mu}(u,v) + \langle\, v^*-\bar{v}^*, v\,\rangle_{V^*,V} , \qquad \forall\, v \in V . \tag{3.9}$$

Now since $a_{\lambda,\mu}$ is bounded, the right hand side of (3.9) is bounded by

$$\left(\left\|(\bar{\lambda},\bar{\mu})-(\lambda,\mu)\right\|_\infty \|u\|_{H^1(\Omega)} + \|v^*-\bar{v}^*\|_{V^*}\right)\|v\|_V .$$

Hence, due to the Lax-Milgram Lemma the solution of (3.9) is unique and depends continuously on the right hand side, which immediately yields the assertion. □

Using $A_{\lambda,\mu}$ and $\tilde{A}_{\lambda,\mu}$, the operator $F$ can be written in the alternative form

$$F(\lambda,\mu) = A^{-1}_{\lambda,\mu}\left(l - \tilde{A}_{\lambda,\mu}\Phi\right) , \tag{3.10}$$

with $l$ defined by (2.4). Now since, due to (3.7),

$$\left\|\left(l-\tilde{A}_{\lambda,\mu}\Phi\right)-\left(l-\tilde{A}_{\bar{\lambda},\bar{\mu}}\Phi\right)\right\|_{V^*} = \left\|\tilde{A}_{\bar{\lambda}-\lambda,\bar{\mu}-\mu}\Phi\right\|_{V^*} \leq \left\|(\bar{\lambda},\bar{\mu})-(\lambda,\mu)\right\|_\infty \|\Phi\|_{H^1(\Omega)} ,$$

inequality (3.8) implies

$$\left\|F(\bar{\lambda},\bar{\mu})-F(\lambda,\mu)\right\|_V \leq c_{LM}\left\|(\bar{\lambda},\bar{\mu})-(\lambda,\mu)\right\|_\infty \left(\|F(\lambda,\mu)\|_{H^1(\Omega)} + \|\Phi\|_{H^1(\Omega)}\right) , \tag{3.11}$$

showing that $F$ is a continuous operator.

*Remark.* Note that $F$ can also be considered as an operator from $\mathcal{M}(\underline{\mu})$ to $L^2(\Omega)^N$, in which case Theorem 2.1 and Proposition 3.1 guarantee that it remains well-defined and continuous, which we use later on.

## 3.1 Calculation of the Fréchet Derivative

In this section, we compute the Fréchet derivative $F'(\lambda,\mu)(h_\lambda,h_\mu)$ of $F$ using the representation (3.10).

**Theorem 3.2.** *The operator $F$ defined by (3.10) and considered as an operator from $\mathcal{M}(\underline{\mu}) \to L^2(\Omega)^N$ for some $\underline{\mu} > 0$ is Fréchet differentiable for all $(\lambda,\mu) \in \mathcal{D}(F)$ with*

$$F'(\lambda,\mu)(h_\lambda,h_\mu) = -A_{\lambda,\mu}^{-1}\left(A_{h_\lambda,h_\mu}u(\lambda,\mu) + \tilde{A}_{h_\lambda,h_\mu}\Phi\right). \tag{3.12}$$

*Proof.* We start by defining

$$G_{\lambda,\mu}(h_\lambda,h_\mu) := -A_{\lambda,\mu}^{-1}\left(A_{h_\lambda,h_\mu}u(\lambda,\mu) + \tilde{A}_{h_\lambda,h_\mu}\Phi\right).$$

Due to Proposition 3.1, $G_{\lambda,\mu}$ is a well-defined, bounded linear operator which depends continuously on $(\lambda,\mu) \in D(F)$ with respect to the operator-norm. Hence, if we can prove that $G_{\lambda,\mu}$ is the Gateâux derivative of $F$ it is also the Fréchet derivative of $F$. For this, we look at

$$\begin{aligned}
&\frac{F(\lambda+th_\lambda,\mu+th_\mu)-F(\lambda,\mu)}{t} - G_{\lambda,\mu}(h_\lambda,h_\mu)\\
&\quad= \frac{1}{t}\left(A_{\lambda+th_\lambda,\mu+th_\mu}^{-1}(l-\tilde{A}_{\lambda+th_\lambda,\mu+th_\mu}\Phi) - A_{\lambda,\mu}^{-1}(l-\tilde{A}_{\lambda,\mu}\Phi)\right)\\
&\qquad + A_{\lambda,\mu}^{-1}\left(A_{h_\lambda,h_\mu}u(\lambda,\mu) + \tilde{A}_{h_\lambda,h_\mu}\Phi\right).
\end{aligned} \tag{3.13}$$

Note that it can happen that $(\lambda+th_\lambda,\mu+th_\mu) \notin \mathcal{D}(F)$. However, choosing $t$ small enough, one can always guarantee that $(\lambda+th_\lambda,\mu+th_\mu) \in \mathcal{M}(\underline{\mu})$, in which case $F(\lambda+th_\lambda,\mu+th_\mu)$ remains well-defined as noted above. Applying $A_{\lambda,\mu}$ to (3.13) we get

$$\begin{aligned}
&A_{\lambda,\mu}\left(\frac{F(\lambda+th_\lambda,\mu+th_\mu)-F(\lambda,\mu)}{t} - G_{\lambda,\mu}(th_\lambda,th_\mu)\right)\\
&= \frac{1}{t}\left(A_{\lambda,\mu}A_{\lambda+th_\lambda,\mu+th_\mu}^{-1}(l-\tilde{A}_{\lambda+th_\lambda,\mu+th_\mu}\Phi) - (l-\tilde{A}_{\lambda,\mu}\Phi)\right) + \left(A_{h_\lambda,h_\mu}u(\lambda,\mu) + \tilde{A}_{h_\lambda,h_\mu}\Phi\right),
\end{aligned}$$

which, together with

$$\begin{aligned}
&A_{\lambda,\mu}A_{\lambda+th_\lambda,\mu+th_\mu}^{-1}(l-\tilde{A}_{\lambda+th_\lambda,\mu+th_\mu}\Phi)\\
&= (l-\tilde{A}_{\lambda+th_\lambda,\mu+th_\mu}\Phi) - tA_{h_\lambda,h_\mu}A_{\lambda+th_\lambda,\mu+th_\mu}^{-1}(l-\tilde{A}_{\lambda+th_\lambda,\mu+th_\mu}\Phi),
\end{aligned}$$

yields

$$\begin{aligned}
&A_{\lambda,\mu}\left(\frac{F(\lambda+th_\lambda,\mu+th_\mu)-F(\lambda,\mu)}{t} - G_{\lambda,\mu}(th_\lambda,th_\mu)\right)\\
&= -A_{h_\lambda,h_\mu}A_{\lambda+th_\lambda,\mu+th_\mu}^{-1}(l-\tilde{A}_{\lambda+th_\lambda,\mu+th_\mu}\Phi) + A_{h_\lambda,h_\mu}u(\lambda,\mu)\\
&= -A_{h_\lambda,h_\mu}\left(u(\lambda+th_\lambda,\mu+th_\mu) - u(\lambda,\mu)\right).
\end{aligned} \tag{3.14}$$

By the continuity of $A_{\lambda,\mu}$ and $A_{\lambda,\mu}^{-1}$ and due to (3.11) we can deduce that $G_{\lambda,\mu}$ is indeed the Gateâux derivative and, due to the continuous dependence on $(\lambda, \mu)$, also the Fréchet derivative of $F$, which concludes the proof. □

Concerning the calculation of $F'(\lambda,\mu)(h_\lambda, h_\mu)$, note that it can be carried out in two distinct steps, requiring the solution of two variational problems involving the same bilinear form $a_{\lambda,\mu}$ (which can be used for efficient implementation) as follows:

1. Calculate $u \in V$ as the solution of the variational problem (2.6).
2. Calculate $F'(\lambda,\mu)(h_\lambda, h_\mu) \in V$ as the solution $\hat{u}$ of the variational problem

$$a_{\lambda,\mu}(\hat{u}, v) = -a_{h_\lambda,h_\mu}(u, v) - a_{h_\lambda,h_\mu}(\Phi, v)\,, \qquad \forall\, v \in V\,.$$

*Remark.* Note that for classical results on iterative regularization methods (see [28]) to be applicable, one needs that both the definition space and the image space are Hilbert spaces. However, the operator $F$ given by (3.2) is defined on $L^\infty(\Omega)^2$. Therefore, one could think of applying Banach space regularization theory to the problem (see for example [29, 40, 41]). Unfortunately, a commonly used assumption is that the involved Banach spaces are reflexive, which excludes $L^\infty(\Omega)^2$. Hence, a commonly used approach is to consider a space which embeds compactly into $L^\infty(\Omega)^2$, for example the Banach space $W^{1,p}(\Omega)^2$ or the Hilbert space $H^s(\Omega)^2$ with $p$ and $s$ large enough, respectively. Although it is preferable to assume as little smoothness as possible for the Lamé parameters, we focus on the $H^s(\Omega)^2$ setting in this paper, since the resulting inverse problem is already difficult enough to treat analytically.

Due to Sobolev's embedding theorem [1], the Sobolev space $H^s(\Omega)$ embeds compactly into $L^\infty(\Omega)$ for $s > N/2$, i.e., there exists a constant $c_E^s > 0$ such that

$$\|v\|_{L^\infty(\Omega)} \le c_E^s \|v\|_{H^s(\Omega)}\,, \qquad \forall\, v \in H^s(\Omega)\,. \tag{3.15}$$

This suggests to consider $F$ as an operator from

$$\mathcal{D}_s(F) := \{(\lambda,\mu) \in H^s(\Omega)^2 \,|\, \lambda \ge 0\,, \mu \ge \underline{\mu} > 0\} \to L^2(\Omega)^N\,, \tag{3.16}$$

for some $s > N/2$. Since due to (3.15) there holds $\mathcal{D}_s(F) \subset \mathcal{D}(F)$, our previous results on continuity and Fréchet differentiability still hold in this case. Furthermore, it is now possible to consider the resulting inverse problem $F(\lambda,\mu) = u$ in the classical Hilbert space framework. Hence, in what follows, we always consider $F$ as an operator from $\mathcal{D}_s(F) \to L^2(\Omega)^2$ for some $s > N/2$.

## 3.2 Calculation of the Adjoint of the Fréchet Derivative

We now turn to the calculation of $F'(\lambda,\mu)^* w$, the adjoint of the Fréchet derivative of $F$, which is required below. For doing so, note first that for $A_{\lambda,\mu}$ defined by (3.5)

$$\langle\, A_{\lambda,\mu} v, \bar{v}\,\rangle_{V^*,V} = \langle\, A_{\lambda,\mu}\bar{v}, v\,\rangle_{V^*,V}\,, \qquad \forall\, v, \bar{v} \in V\,. \tag{3.17}$$

This follows immediately from the definition of $A_{\lambda,\mu}$ and the symmetry of the bilinear form $a_{\lambda,\mu}$. Moreover, as an immediate consequence of (3.17), and continuity of $A_{\lambda,\mu}^{-1}$ it follows

$$\left\langle v^*, A_{\lambda,\mu}^{-1}\bar{v}^* \right\rangle_{V^*,V} = \left\langle \bar{v}^*, A_{\lambda,\mu}^{-1}v^* \right\rangle_{V^*,V}, \qquad \forall\, v^*, \bar{v}^* \in V^*. \tag{3.18}$$

In order to give an explicit form of $F'(\lambda,\mu)^* w$ we need the following

**Lemma 3.3.** *The linear operators $T : L^2(\Omega)^N \to V^*$, defined by*

$$Tw := \left( v \mapsto \int_\Omega w \cdot v \, dx \right), \tag{3.19}$$

*and $E_s : L^1(\Omega) \to H^s(\Omega)$,*

$$\left\langle E_s u, v \right\rangle_{H^s(\Omega)} = \int_\Omega uv \, dx, \qquad \forall v \in H^s(\Omega), \tag{3.20}$$

*respectively, are well-defined and bounded for all $s > N/2$.*

*Proof.* Using the Cauchy-Schwarz inequality it is easy to see that $T$ is bounded with $\|T\|_{L^2(\Omega),V^*} \le 1$. Furthermore, due to (3.15),

$$\int_\Omega uv \, dx \le \|u\|_{L^1(\Omega)} \|v\|_{L^\infty(\Omega)} \le c_E^s \|u\|_{L^1(\Omega)} \|v\|_{H^s(\Omega)}, \quad \forall v \in H^s(\Omega),$$

and the Lax-Milgram Lemma also $E_s$ is bounded for $s > N/2$. □

Using this, we can now proof the main result of this section.

**Theorem 3.4.** *Let $F : \mathcal{D}_s(F) \to L^2(\Omega)^2$ with $\mathcal{D}_s(F)$ given as in (3.16) for some $s > N/2$. Then the adjoint of the Fréchet derivative of $F$ is given by*

$$F'(\lambda,\mu)^* w = \begin{pmatrix} E_s\left(\operatorname{div}\left(u(\lambda,\mu)+\Phi\right)\operatorname{div}\left(-A_{\lambda,\mu}^{-1}Tw\right)\right) \\ E_s\left(2\,\mathcal{E}\left(u(\lambda,\mu)+\Phi\right) : \mathcal{E}\left(-A_{\lambda,\mu}^{-1}Tw\right)\right) \end{pmatrix}^T, \tag{3.21}$$

*where $T$ and $E_s$ are defined by (3.19) and (3.20), respectively.*

*Proof.* Using Theorem 3.2 and (3.19) we get

$$\begin{aligned} \left\langle F'(\lambda,\mu)(h_\lambda,h_\mu), w \right\rangle_{L^2(\Omega)} &= \left\langle -A_{\lambda,\mu}^{-1}(A_{h_\lambda,h_\mu}u(\lambda,\mu) + \tilde{A}_{h_\lambda,h_\mu}\Phi), w \right\rangle_{L^2(\Omega)} \\ &= \left\langle Tw, -A_{\lambda,\mu}^{-1}(A_{h_\lambda,h_\mu}u(\lambda,\mu) + \tilde{A}_{h_\lambda,h_\mu})\Phi) \right\rangle_{V^*,V} \end{aligned}$$

Together with (3.18) and the definition of $A_{h_\lambda,h_\mu}$ and $a_{h_\lambda,h_\mu}$ we get

$$\begin{aligned} &\left\langle Tw, -A_{\lambda,\mu}^{-1}(A_{h_\lambda,h_\mu}u(\lambda,\mu) + \tilde{A}_{h_\lambda,h_\mu})\Phi) \right\rangle_{V^*,V} = a_{h_\lambda,h_\mu}\left(u(\lambda,\mu)+\Phi, -A_{\lambda,\mu}^{-1}Tw\right) \\ &= \int_\Omega h_\lambda \operatorname{div}\left(u(\lambda,\mu)+\Phi\right)\operatorname{div}\left(-A_{\lambda,\mu}^{-1}Tw\right) dx + \int_\Omega 2h_\mu\,\mathcal{E}\left(u(\lambda,\mu)+\Phi\right) : \mathcal{E}\left(-A_{\lambda,\mu}^{-1}Tw\right) dx. \end{aligned}$$

Together with the fact that the product of two $L^2(\Omega)$ functions is in $L^1(\Omega)$, which applies to $\operatorname{div}(u(\lambda,\mu)+\Phi)\operatorname{div}\left(-A_{\lambda,\mu}^{-1}Tw\right)$ and $\mathcal{E}(u(\lambda,\mu)+\Phi):\mathcal{E}\left(-A_{\lambda,\mu}^{-1}Tw\right)$, the statement of the theorem now immediately follows from the definition of $E_s$ (3.20). □

Concerning the calculation of $F'(\lambda,\mu)^*w$, note that it can again be carried out in independent steps, namely:

1. Calculate $u \in V$ as the solution of the variational problem (2.6).
2. Compute $A_{\lambda,\mu}^{-1}Tw$, i.e., find the solution $u(w) \in V$ of the variational problem
$$a_{\lambda,\mu}(u(w),v) = \int_\Omega w \cdot v\, dx\,, \qquad \forall\, v \in V\,.$$
3. Compute the functions $u_1(w), u_2(w) \in L^1(\Omega)$ given by
$$\begin{aligned} u_1(w) &:= \operatorname{div}(u+\Phi)\operatorname{div}(-u(w))\,,\\ u_2(w) &:= 2\,\mathcal{E}(u+\Phi):\mathcal{E}(-u(w))\,. \end{aligned}$$
4. Calculate the functions $\hat\lambda(w) := E_s\, u_1(w)$ and $\hat\mu(w) := E_s\, u_2(w)$ as the solutions of the variational problems
$$\begin{aligned} \left\langle \hat\lambda(w), v \right\rangle_{H^s(\Omega)} &= \int_\Omega u_1(w)\, v\, dx\,, \qquad \forall v \in H^s(\Omega)\,,\\ \left\langle \hat\mu(w), v \right\rangle_{H^s(\Omega)} &= \int_\Omega u_2(w)\, v\, dx\,, \qquad \forall v \in H^s(\Omega)\,. \end{aligned}$$
5. Combine the results to obtain $F'(\lambda,\mu)^*w = (\hat\lambda(w), \hat\mu(w))$.

## 3.3 Reconstruction of compactly supported Lamé parameters

In many cases, the Lamé parameters $\lambda, \mu$ are known in a small neighbourhood of the boundary and hence have to be reconstructed only on the remaining part. As a physical problem, we have in mind a test sample consisting of a known material with various inclusions of unknown location and Lamé parameters inside. The resulting inverse problem is better behaved than the original problem and we are even able to prove a nonlinearity condition guaranteeing convergence of iterative solution methods for nonlinear ill-posed problems in this case.

More precisely, assume that we are given a bounded, open, connected Lipschitz domain $\Omega_1 \subset \Omega$ with $\bar\Omega_1 \Subset \Omega$ and background functions $0 \le \lambda_b \in H^s(\Omega)$ and $\bar\mu \le \mu_b \in H^s(\Omega)$ and assume that the searched for Lamé parameters can be written in the form $(\lambda_b + \lambda, \mu_b + \mu)$, where both $\lambda, \mu \in H^s(\Omega)$ are compactly supported in $\Omega_1$. Hence, after introducing the set
$$\mathcal{D}_s(F_c) := \left\{(\lambda,\mu) \in H^s(\Omega)^2 \,|\, \lambda \ge -\lambda_b\,,\ \mu \ge \underline{\mu} - \mu_b > 0\,,\ \operatorname{supp}((\lambda,\mu)) \subset \Omega_1\right\}\,,$$

we define the operator

$$F_c : \mathcal{D}_s(F_c) \to L^2(\Omega)^N, \quad (\lambda, \mu) \mapsto F_c(\lambda, \mu) := F(\lambda_b + \lambda, \mu_b + \mu), \tag{3.22}$$

which is well-defined for $s > N/2$. Hence, the sought for Lamé parameters can be reconstructed by solving the problem $F_c(\lambda, \mu) = u$ and taking $(\lambda_b + \lambda, \mu_b + \mu)$.

Continuity and Fréchet differentiability of $F$ also transfer to $F_c$. For example,

$$F_c'(\lambda, \mu)(h_\lambda, h_\mu) = -A^{-1}_{(\lambda_b+\lambda, \mu_b+\mu)} \left( A_{h_\lambda, h_\mu} u(\lambda, \mu) + \tilde{A}_{h_\lambda, h_\mu} \Phi \right). \tag{3.23}$$

Furthermore, a similar expression as for the adjoint of the Fréchet derivative of $F$ also holds for $F_c$. Consequently, the computation and implementation of $F_c$, its derivative and the adjoint can be carried out in the same way as for the operator $F$ and hence, the two require roughly the same amount of computational work. However, as we see in the next section, for the operator $F_c$ it is possible to prove a nonlinearity condition.

## 3.4 Strong Nonlinearity Condition

The so-called *(strong) tangential cone condition* or *(strong) nonlinearity condition* is the basis of the convergence analysis of iterative regularization methods for nonlinear ill-posed problems [28]. In the theorem below we show a version of this nonlinearity condition sufficient for proving convergence of iterative methods for the operator $F_c$.

**Theorem 3.5.** *Let $F : \mathcal{D}_s(F) \to L^2(\Omega)^2$ for some $s > N/2 + 1$ and let $\Omega_1 \subset \Omega$ be a bounded, open, connected Lipschitz domain with $\bar{\Omega}_1 \Subset \Omega$. Then for each $(\lambda, \mu) \in \mathcal{D}_s(F)$ there exists a constant $c_{NL} = c_{NL}(\lambda, \mu, \Omega_1, \Omega) > 0$ such that for all $(\bar{\lambda}, \bar{\mu}) \in \mathcal{D}_s(F)$ satisfying $(\lambda, \mu) = (\bar{\lambda}, \bar{\mu})$ on $\Omega \setminus \Omega_1$ and $(\lambda, \mu) = (\bar{\lambda}, \bar{\mu})$ on $\partial\Omega_1$ there holds*

$$\begin{aligned} &\left\| F(\lambda, \mu) - F(\bar{\lambda}, \bar{\mu}) - F'(\lambda, \mu)((\lambda, \mu) - (\bar{\lambda}, \bar{\mu})) \right\|_{L^2(\Omega)} \\ &\qquad \le c_{NL} \left\| (\bar{\lambda} - \lambda, \bar{\mu} - \mu) \right\|_{W^{1,\infty}(\Omega_1)} \left\| F(\lambda, \mu) - F(\bar{\lambda}, \bar{\mu}) \right\|_{L^2(\Omega)}. \end{aligned} \tag{3.24}$$

*Proof.* Let $(\lambda, \mu), (\bar{\lambda}, \bar{\mu}) \in \mathcal{D}_s(F)$ with $s > N/2+1$ such that $(\lambda, \mu) = (\bar{\lambda}, \bar{\mu})$ on $\Omega \setminus \Omega_1$ and $(\lambda, \mu) = (\bar{\lambda}, \bar{\mu})$ on $\partial\Omega_1$. For the purpose of this proof, set $u = F(\lambda, \mu)$ and $\bar{u} = F(\bar{\lambda}, \bar{\mu})$. By definition, we have

$$\begin{aligned} &\left\langle F(\lambda, \mu) - F(\bar{\lambda}, \bar{\mu}) - F'(\lambda, \mu)((\lambda, \mu) - (\bar{\lambda}, \bar{\mu})), w \right\rangle_{L^2(\Omega)} \\ &\quad = \left\langle (u - \bar{u}) - A^{-1}_{\lambda,\mu} \left( A_{\bar{\lambda}-\lambda, \bar{\mu}-\mu} u + \tilde{A}_{\bar{\lambda}-\lambda, \bar{\mu}-\mu} \Phi \right), w \right\rangle_{L^2(\Omega)}. \end{aligned}$$

Together with (3.19) and (3.18), we get

$$\begin{aligned} &\left\langle (u - \bar{u}) - A^{-1}_{\lambda,\mu} \left( A_{\bar{\lambda}-\lambda, \bar{\mu}-\mu} u + \tilde{A}_{\bar{\lambda}-\lambda, \bar{\mu}-\mu} \Phi \right), w \right\rangle_{L^2(\Omega)} \\ &\quad = \left\langle A_{\lambda,\mu}(u - \bar{u}) - \left( A_{\bar{\lambda}-\lambda, \bar{\mu}-\mu} u + \tilde{A}_{\bar{\lambda}-\lambda, \bar{\mu}-\mu} \Phi \right), A^{-1}_{\lambda,\mu} T w \right\rangle_{V^*, V}, \end{aligned}$$

which can be written as

$$\left\langle A_{\bar\lambda-\lambda,\bar\mu-\mu}\,(\bar u-u)\,,A^{-1}_{\lambda,\mu}Tw\right\rangle_{V^*,V}+\left\langle A_{\lambda,\mu}(u-\bar u)-A_{\bar\lambda-\lambda,\bar\mu-\mu}\bar u-\tilde A_{\bar\lambda-\lambda,\bar\mu-\mu}\Phi,A^{-1}_{\lambda,\mu}Tw\right\rangle_{V^*,V}.$$

Now since

$$\begin{aligned}&A_{\lambda,\mu}(u-\bar u)-A_{\bar\lambda-\lambda,\bar\mu-\mu}\bar u-\tilde A_{\bar\lambda-\lambda,\bar\mu-\mu}\Phi\\&\quad=l-\tilde A_{\lambda,\mu}\Phi-A_{\lambda,\mu}\bar u-A_{\bar\lambda-\lambda,\bar\mu-\mu}\bar u-\tilde A_{\bar\lambda-\lambda,\bar\mu-\mu}\Phi=0\,,\end{aligned}$$

it follows together with (3.17) that

$$\begin{aligned}&\left\langle F(\lambda,\mu)-F(\bar\lambda,\bar\mu)-F'(\lambda,\mu)((\lambda,\mu)-(\bar\lambda,\bar\mu)),w\right\rangle_{L^2(\Omega)}\\&\quad=\left\langle A_{\bar\lambda-\lambda,\bar\mu-\mu}\,(\bar u-u)\,,A^{-1}_{\lambda,\mu}Tw\right\rangle_{V^*,V}=\left\langle A_{\bar\lambda-\lambda,\bar\mu-\mu}A^{-1}_{\lambda,\mu}Tw,\bar u-u\right\rangle_{V^*,V}.\end{aligned}$$

Introducing the abbreviation $z:=A^{-1}_{\lambda,\mu}Tw$, and using the definition of $A_{\bar\lambda-\lambda,\bar\mu-\mu}$

$$\begin{aligned}&\left\langle A_{\bar\lambda-\lambda,\bar\mu-\mu}z,\bar u-u\right\rangle_{V^*,V}=a_{\bar\lambda-\lambda,\bar\mu-\mu}(z,\bar u-u)\\&\quad=\int_{\Omega_1}\left((\bar\lambda-\lambda)\,\operatorname{div}(z)\operatorname{div}(\bar u-u)+2(\bar\mu-\mu)\,\mathcal{E}(z):\mathcal{E}(\bar u-u)\right)dx\,,\end{aligned}$$

where we have used that $(\bar\lambda-\lambda,\bar\mu-\mu)=0$ on $\Omega\backslash\Omega_1$. Since we also have $(\bar\lambda-\lambda,\bar\mu-\mu)=0$ on $\partial\Omega_1$, partial integration together with the regularity result Lemma 5.1 yields

$$\begin{aligned}&\int_{\Omega_1}\left((\bar\lambda-\lambda)\,\operatorname{div}(z)\operatorname{div}(\bar u-u)+2(\bar\mu-\mu)\,\mathcal{E}(z):\mathcal{E}(\bar u-u)\right)dx\\&\quad=-\int_{\Omega_1}\operatorname{div}\left((\bar\lambda-\lambda)\,\operatorname{div}(z)\,I+2(\bar\mu-\mu)\,\mathcal{E}(z)\right)\cdot(\bar u-u)\,dx\\&\quad\le\left\|\operatorname{div}\left((\bar\lambda-\lambda)\,\operatorname{div}(z)\,I+2(\bar\mu-\mu)\,\mathcal{E}(z)\right)\right\|_{L^2(\Omega_1)}\|\bar u-u\|_{L^2(\Omega_1)}.\end{aligned}\tag{3.25}$$

Now, since there exists a constant $c_G=c_G(N)$ such that for all $v\in H^2(\Omega_1)^N$

$$\|\operatorname{div}(\lambda\,\operatorname{div}(v)\,I+2\mu\,\mathcal{E}(v))\|_{L^2(\Omega_1)}\le c_G\max\{\|\lambda\|_{W^{1,\infty}(\Omega_1)},\|\mu\|_{W^{1,\infty}(\Omega_1)}\}\,\|v\|_{H^2(\Omega_1)}.$$

Now since

$$\begin{aligned}&\left\|F(\lambda,\mu)-F(\bar\lambda,\bar\mu)-F'(\lambda,\mu)((\lambda,\mu)-(\bar\lambda,\bar\mu))\right\|_{L^2(\Omega)}\\&\quad=\sup_{\|w\|_{L^2(\Omega)}=1}\left\langle F(\lambda,\mu)-F(\bar\lambda,\bar\mu)-F'(\lambda,\mu)((\lambda,\mu)-(\bar\lambda,\bar\mu)),w\right\rangle_{L^2(\Omega)},\end{aligned}$$

combining the above results we get

$$\begin{aligned}&\sup_{\|w\|_{L^2(\Omega)}=1}\left\langle F(\lambda,\mu)-F(\bar\lambda,\bar\mu)-F'(\lambda,\mu)((\lambda,\mu)-(\bar\lambda,\bar\mu)),w\right\rangle_{L^2(\Omega)}\\&\quad\le\sup_{\|w\|_{L^2(\Omega)}=1}c_G\left\|(\bar\lambda-\lambda,\bar\mu-\mu)\right\|_{W^{1,\infty}(\Omega_1)}\|z\|_{H^2(\Omega_1)}\|\bar u-u\|_{L^2(\Omega_1)}.\end{aligned}$$

Together with Lemma 5.1, which implies that there exists a constant $c_R > 0$ such that $\|z\|_{H^2(\Omega_1)} \leq c_R \|w\|_{L^2(\Omega_1)}$, we get

$$\begin{aligned}
&\left\|F(\lambda,\mu) - F(\bar\lambda,\bar\mu) - F'(\lambda,\mu)((\lambda,\mu)-(\bar\lambda,\bar\mu))\right\|_{L^2(\Omega)} \\
&\quad \leq c_G\, c_R \left\|(\bar\lambda-\lambda,\bar\mu-\mu)\right\|_{W^{1,\infty}(\Omega_1)} \|\bar u - u\|_{L^2(\Omega_1)} \\
&\quad \leq c_G\, c_R \left\|(\bar\lambda-\lambda,\bar\mu-\mu)\right\|_{W^{1,\infty}(\Omega_1)} \|\bar u - u\|_{L^2(\Omega)} \ ,
\end{aligned}$$

which immediately yields the assertion with $c_{NL} := c_G\, c_R$. □

We get the following useful corollary

**Corollary 3.6.** *Let $F_c$ be defined as in (3.22) for some $s > N/2+1$. Then for each $(\lambda,\mu) \in \mathcal{D}_s(F_c)$ there exists a constant $c_{NL} = c_{NL}(\lambda,\mu,\Omega_1,\Omega) > 0$ such that for all $(\bar\lambda,\bar\mu) \in \mathcal{D}_s(F_c)$ there holds*

$$\begin{aligned}
&\left\|F_c(\lambda,\mu) - F_c(\bar\lambda,\bar\mu) - F_c'(\lambda,\mu)((\lambda,\mu)-(\bar\lambda,\bar\mu))\right\|_{L^2(\Omega)} \\
&\qquad \leq c_{NL} \left\|(\bar\lambda-\lambda,\bar\mu-\mu)\right\|_{W^{1,\infty}(\Omega_1)} \left\|F_c(\lambda,\mu) - F_c(\bar\lambda,\bar\mu)\right\|_{L^2(\Omega)} \ .
\end{aligned} \tag{3.26}$$

*Proof.* This follows from the definition of $F_c$ and (the proof of) Theorem 3.5. □

In the following theorem, we establish a similar result as in Corollary 3.6 now for $F : \mathcal{D}_s(F) \to L^2(\Omega)^2$ in case that $\Gamma_T = \emptyset$, i.e., $\Gamma_D = \partial\Omega$ and that $\partial\Omega$ is smooth enough.

**Theorem 3.7.** *Let $F : \mathcal{D}_s(F) \to L^2(\Omega)^2$ for some $s > N/2+1$ and let $\partial\Omega = \Gamma_D \in C^{1,1}$ and $\Gamma_T = \emptyset$. Then for each $(\lambda,\mu) \in \mathcal{D}_s(F)$ there exists a constant $c_{NL} = c_{NL}(\lambda,\mu,\Omega) > 0$ such that for all $(\bar\lambda,\bar\mu) \in \mathcal{D}_s(F)$, there holds*

$$\begin{aligned}
&\left\|F(\lambda,\mu) - F(\bar\lambda,\bar\mu) - F'(\lambda,\mu)((\lambda,\mu)-(\bar\lambda,\bar\mu))\right\|_{L^2(\Omega)} \\
&\qquad \leq c_{NL} \left\|(\bar\lambda-\lambda,\bar\mu-\mu)\right\|_{W^{1,\infty}(\Omega)} \left\|F(\lambda,\mu) - F(\bar\lambda,\bar\mu)\right\|_{L^2(\Omega)} \ .
\end{aligned} \tag{3.27}$$

*Proof.* The prove of this theorem is analogous to the one of Theorem 3.5, noting that for this choice of boundary condition, the regularity results of Lemma 5.1 also hold on the entire domain, i.e., for $\Omega_1 = \Omega$, which follows for example from [33, Theorem 4.16 and Theorem 4.18]. Furthermore, the boundary integral appearing in the partial integration step in (3.25) also vanishes in this case, since $\bar u = u = 0$ on $\partial\Omega$ due to the assumption that $\partial\Omega = \Gamma_D$. □

As can be found for example in [2,13,19,34], $H^2(\Omega)$ regularity and hence the above theorem can also be proven under weaker smoothness assumptions on the domain $\Omega$. For example, it suffices that $\Omega$ is a convex Lipschitz domain.

*Remark.* In case of mixed boundary conditions, i.e., $\operatorname{meas}(\Gamma_T) > 0$, a nonlinearity condition like (3.27) can only be proven in the way described above if in addition to $H^2(\Omega)$ regularity of $A_{\lambda,\mu}^{-1} T w$ one can show that there exists a constant $c_I > 0$ such that

$$\begin{aligned}
&\left| \int_{\partial\Omega} \left((\bar\lambda-\lambda)\ \operatorname{div}\left(A_{\lambda,\mu}^{-1} T w\right)\right) I + 2(\bar\mu-\mu)\, \mathcal{E}\left(A_{\lambda,\mu}^{-1} T w\right) \vec n \cdot (\bar u - u)\, dS \right| \\
&\qquad \leq c_I \|w\|_{L^2(\Omega)} \left\|(\bar\lambda-\lambda,\bar\mu-\mu)\right\|_{W^{1,\infty}(\Omega)} \|\bar u - u\|_{L^2(\Omega)} \ .
\end{aligned} \tag{3.28}$$

As mentioned above, for mixed boundary conditions full $H^2(\Omega)$ regularity can in general not be expected. However, if the domain $\Omega$ is a rectangle in $\mathbb{R}^2$, i.e., $N = 2$, with both $g_D$ and $g_T$ consisting of the two opposite edges of the rectangle, then full $H^2(\Omega)$ regularity can be proven (see Appendix 2, Proposition 5.2). Nevertheless, the authors did not manage to prove (3.28) so far.

*Remark.* Note that (3.26) is already strong enough to prove convergence of Landweber iteration for the operator $F_c$ to a solution $(\lambda^\dagger, \mu^\dagger)$ given that the initial guess $(\lambda_0, \mu_0)$ is chosen close enough to $(\lambda^\dagger, \mu^\dagger)$ [21, 28]. Furthermore, if there is a $\bar{\rho} > 0$ such that

$$\sup_{(\lambda,\mu)\in \mathcal{B}_{\bar{\rho}}(\lambda^\dagger,\mu^\dagger)\cap\mathcal{D}_s(F_c)} c_R(\lambda, \mu, \Omega_1, \Omega) \, < \infty \,, \tag{3.29}$$

then for each $\eta > 0$ there exists a $\rho > 0$ such that

$$\begin{aligned} \left\| F_c(\lambda,\mu) - F_c(\bar{\lambda},\bar{\mu}) - F_c'(\lambda,\mu)((\lambda,\mu)-(\bar{\lambda},\bar{\mu}))\right\|_{L^2(\Omega)} \leq \eta \left\| F_c(\lambda,\mu) - F_c(\bar{\lambda},\bar{\mu})\right\|_{L^2(\Omega)} \,, \\ \forall\, (\lambda,\mu), (\bar{\lambda},\bar{\mu}) \in \mathcal{B}_{2\rho}(\lambda_0,\mu_0)\,, \end{aligned}$$

which is the original, well-known nonlinearity condition [21]. Obviously, the same statements also hold analogously for the $F : \mathcal{D}_s(F) \to L^2(\Omega)$ under the assumptions of Theorem 3.7. Note further that condition (3.29) follows directly from the proofs of [33, Theorem 4.16 and Theorem 4.18].

## 3.5 An Informal Discussion of Source Conditions

For general inverse problems of the form $F(x) = y$, source conditions of the form

$$x^\dagger - x_0 \in \mathcal{R}(F'(x^\dagger)^*)\,, \tag{3.30}$$

are important for showing convergence rates or even proving convergence of certain gradient-type methods for nonlinear ill-posed problems [28]. In this section, we make an investigation of the source condition for $F : \mathcal{D}_s(F) \to L^2(\Omega)^N$ and $N = 2, 3$.

**Lemma 3.8.** *Let $F : \mathcal{D}_s(F) \to L^2(\Omega)^N$ with $s > N/2 + 1$. Then* (3.30) *is equivalent to the existence of a $w \in L^2(\Omega)^N$ such that*

$$\begin{pmatrix} \lambda^\dagger - \lambda_0 \\ \mu^\dagger - \mu_0 \end{pmatrix} = \begin{pmatrix} E_s \left( \operatorname{div}\left(u(\lambda^\dagger,\mu^\dagger) + \Phi\right) \operatorname{div}\left(-A^{-1}_{\lambda^\dagger,\mu^\dagger} T w\right)\right) \\ E_s \left( 2\,\mathcal{E}\left(u(\lambda^\dagger,\mu^\dagger) + \Phi\right) : \mathcal{E}\left(-A^{-1}_{\lambda^\dagger,\mu^\dagger} T w\right)\right) \end{pmatrix}. \tag{3.31}$$

*Proof.* This follows immediately from (3.4). □

Hence, one has to have that $\lambda^\dagger - \lambda_0 \in \mathcal{R}(E_s)$ and $\mu^\dagger - \mu_0 \in \mathcal{R}(E_s)$ and

$$\begin{pmatrix} {E_s}^{-1}(\lambda^\dagger - \lambda_0) \\ {E_s}^{-1}(\mu^\dagger - \mu_0) \end{pmatrix} = \begin{pmatrix} \operatorname{div}\left(u(\lambda^\dagger,\mu^\dagger) + \Phi\right) \operatorname{div}\left(-A^{-1}_{\lambda^\dagger,\mu^\dagger} T w\right) \\ 2\,\mathcal{E}\left(u(\lambda^\dagger,\mu^\dagger) + \Phi\right) : \mathcal{E}\left(-A^{-1}_{\lambda^\dagger,\mu^\dagger} T w\right) \end{pmatrix}. \tag{3.32}$$

If $\operatorname{div}\left(u(\lambda^\dagger,\mu^\dagger)+\Phi\right)\operatorname{div}\left(-A^{-1}_{\lambda^\dagger,\mu^\dagger}Tw\right)$ and $2\,\mathcal{E}\left(u(\lambda^\dagger,\mu^\dagger)+\Phi\right):\mathcal{E}\left(-A^{-1}_{\lambda^\dagger,\mu^\dagger}Tw\right)$ are in $L^2(\Omega)$, which is for example the case if $w$ as well as $f$, $\Phi$, $g_D$ and $g_T$ satisfy additional $L^p(\Omega)$ regularity [13], then $E_s$ coincides with $i^*$, where $i$ is given as the embedding operator from $H^s(\Omega)\to L^2(\Omega)$. In this case, $\lambda^\dagger-\lambda_0\in\mathcal{R}(E_s)$ and $\mu^\dagger-\mu_0\in\mathcal{R}(E_s)$ imply a certain differentiability and boundary conditions on $\lambda^\dagger-\lambda_0$ and $\mu^\dagger-\mu_0$. Now, if

$$\frac{{E_s}^{-1}(\lambda^\dagger-\lambda_0)}{\operatorname{div}\left(u(\lambda^\dagger,\mu^\dagger)+\Phi\right)}\in L^2(\Omega)\,,$$

then (3.32) can be rewritten as

$$\begin{pmatrix}{E_s}^{-1}(\lambda^\dagger-\lambda_0)/\operatorname{div}\left(u(\lambda^\dagger,\mu^\dagger)+\Phi\right)\\ {E_s}^{-1}(\mu^\dagger-\mu_0)\end{pmatrix}=\begin{pmatrix}\operatorname{div}\left(-A^{-1}_{\lambda^\dagger,\mu^\dagger}Tw\right)\\ 2\,\mathcal{E}\left(u(\lambda^\dagger,\mu^\dagger)+\Phi\right):\mathcal{E}\left(-A^{-1}_{\lambda^\dagger,\mu^\dagger}Tw\right)\end{pmatrix}. \tag{3.33}$$

Since $A^{-1}_{\lambda^\dagger,\mu^\dagger}Tw\in V\subset H^1(\Omega)^N$, by the Helmholtz decomposition there exists a function $\phi=\phi(w)\in H^2(\Omega)$ and a vector field $\psi=\psi(w)\in H^2(\Omega)^N$ such that

$$\begin{aligned}-A^{-1}_{\lambda^\dagger,\mu^\dagger}Tw&=\nabla\phi(w)+\nabla\times\psi(w)\,,\\ \left(\nabla\phi(w)+\nabla\times\psi(w)\right)|_{\Gamma_D}&=0\,.\end{aligned}$$

Hence, (3.33) is equivalent to

$$\begin{aligned}\Delta\phi(w)&={E_s}^{-1}(\lambda^\dagger-\lambda_0)/\operatorname{div}\left(u(\lambda^\dagger,\mu^\dagger)+\Phi\right)\,,\\ {E_s}^{-1}(\mu^\dagger-\mu_0)&=2\,\mathcal{E}\left(u(\lambda^\dagger,\mu^\dagger)+\Phi\right):\mathcal{E}\left(\nabla\phi(w)+\nabla\times\psi(w)\right)\,,\\ \left(\nabla\phi(w)+\nabla\times\psi(w)\right)|_{\Gamma_D}&=0\,.\end{aligned} \tag{3.34}$$

Note that once $\phi$ and $\psi$ are known such that $-A^{-1}_{\lambda^\dagger,\mu^\dagger}Tw=\nabla\phi+\nabla\times\psi$ holds, $w$ can be uniquely recovered in the following way. Due to the Lax-Milgram Lemma, there exists an element $z(\phi,\psi)\in V$ such that

$$-\left\langle A_{\lambda^\dagger,\mu^\dagger}\left(\nabla\phi+\nabla\times\psi\right),v\right\rangle_{V^*,V}=\left\langle z(\phi,\psi),v\right\rangle_V\,,\qquad\forall\,v\in V\,.$$

However, since

$$\begin{aligned}&-\left\langle A_{\lambda^\dagger,\mu^\dagger}\left(\nabla\phi(w)+\nabla\times\psi(w)\right),v\right\rangle_{V^*,V}\\ &\quad=\left\langle Tw,v\right\rangle_{V^*,V}=\left\langle w,v\right\rangle_{L^2(\Omega)}=\left\langle i_V^*w,v\right\rangle_V\,,\end{aligned}$$

where $i_V$ denotes the embedding from $V$ to $L^2(\Omega)^N$, there follows $z(\phi,\psi)\in\mathcal{R}(i_V^*)$ and $w$ can be recovered by $w=(i_V^*)^{-1}z(\phi,\psi)$.

*Remark.* Hence, we derive that the source condition (3.31) holds for the solution $(\lambda^\dagger,\mu^\dagger)$ and the initial guess $(\lambda_0,\mu_0)$ under the following assumptions:

- $\lambda^\dagger-\lambda_0\in\mathcal{R}(E_s)$ and $\mu^\dagger-\mu_0\in\mathcal{R}(E_s)$ ,

- there holds

$$\frac{{E_s}^{-1}(\lambda^\dagger - \lambda_0)}{\operatorname{div}\left(u(\lambda^\dagger, \mu^\dagger) + \Phi\right)} \in L^2(\Omega)\,, \tag{3.35}$$

- there exist functions $\phi \in H^2(\Omega)$ and $\psi \in H^2(\Omega)^N$ such that

$$\begin{aligned} \Delta\phi &= {E_s}^{-1}(\lambda^\dagger - \lambda_0) / \operatorname{div}\left(u(\lambda^\dagger, \mu^\dagger) + \Phi\right)\,, \\ 2\,\mathcal{E}\left(u(\lambda^\dagger, \mu^\dagger) + \Phi\right) : \mathcal{E}\left(\nabla\phi + \nabla \times \psi\right) &= {E_s}^{-1}(\mu^\dagger - \mu_0)\,, \\ \left(\nabla\phi + \nabla \times \psi\right)|_{\Gamma_D} &= 0\,, \end{aligned}$$

- the unique weak solution $z(\phi, \psi) \in V$ of the variational problem

$$-\left\langle A_{\lambda^\dagger, \mu^\dagger}\left(\nabla\phi + \nabla \times \psi\right), v \right\rangle_{V^*, V} = \left\langle z(\phi, \psi), v \right\rangle_V\,, \qquad \forall\, v \in V\,,$$

  satisfies $z(\phi, \psi) \in \mathcal{R}(i_V^*)$.

The above assumptions are restrictive, which is as usual [28]. However, without these assumptions one cannot expect convergence rates.

*Remark.* Note that since $u(\lambda^\dagger, \mu^\dagger) + \Phi$ is the weak solution of the non-homogenized problem (2.1), condition (3.5) implies that in areas of a divergence free displacement field, one has to know the true Lamé parameter $\lambda^\dagger$. This should be compared to similar conditions in [7–9, 43].

*Remark.* Note that if the source condition is satisfied, then it is known that the iteratively regularized Landweber and Gauss-Newton iterations converge, even if the nonlinearity condition is not satisfied [4, 5, 39].

# 4 Numerical Examples

In this section, we present some numerical examples demonstrating the reconstructions of Lamé parameters from given noisy displacement field measurements $u^\delta$ using both the operators $F|_{\mathcal{D}_s(F)}$ and $F_c$ considered above. The sample problem, described in detail in Section 4.2 is chosen in such a way that it closely mimics a possible real-world setting described below. Furthermore, results are presented showing the reconstruction quality for both smooth and non-smooth Lamé parameters.

## 4.1 Regularization Approach - Landweber Iteration

For reconstructing the Lamé parameters, we use a Two-Point Gradient (TPG) method [24] based on Landweber iteration and on Nesterov's acceleration scheme [35] which, using the abbreviation $x_k^\delta = \left(\lambda_k^\delta, \mu_k^\delta\right)$, is given by

$$\begin{aligned} z_k^\delta &= x_k^\delta + \alpha_k^\delta\left(x_k^\delta - x_{k-1}^\delta\right)\,, \\ x_{k+1}^\delta &= z_k^\delta + \omega_k^\delta\left(z_k^\delta\right) s_k^\delta\left(z_k^\delta\right)\,, \quad s_k^\delta(x) := F'(x)^*\left(u^\delta - F(x)\right)\,. \end{aligned} \tag{4.1}$$

For linear ill-posed problems, a constant stepsize $\omega_k^\delta$ and $\alpha_k^\delta = (k-1)/(k+\alpha-1)$, this method was analysed in [36]. For nonlinear problems, convergence of (4.1) under the tangential cone condition was shown in [24] when the discrepancy principle is used as a stopping rule, i.e., the iteration is stopped after $k_*$ steps, with $k_*$ satisfying

$$\left\|u^\delta - F\left(x_{k_*}^\delta\right)\right\| \leq \tau\delta \leq \left\|u^\delta - F\left(x_k^\delta\right)\right\|, \qquad 0 \leq k \leq k_*, \tag{4.2}$$

where the parameter $\tau$ should be chosen such that

$$\tau > 2\frac{1+\eta}{1-2\eta},$$

although the choices $\tau = 2$ or $\tau$ close to 1 suggested by the linear case are also very popular. For the stepsize $\omega_k^\delta$ we use the steepest descent stepsize [39] and for $\alpha_k^\delta$ we use the well-known Nesterov choice, i.e.,

$$\omega_k^\delta(x) := \frac{\left\|s_k^\delta(x)\right\|^2}{\left\|F'(x)s_k^\delta(x)\right\|^2}, \qquad \text{and} \qquad \alpha_k^\delta = \frac{k-1}{k+2}. \tag{4.3}$$

The method (4.1) is known to work well for both linear and nonlinear inverse problems [23, 27] and also serves as the basis of the well-known FISTA algorithm [12] for solving linear ill-posed problems with sparsity constraints.

## 4.2 Problem Setting, Discretization, and Computation

A possible real-world problem the authors have in mind is a cylinder shaped object made out of agar with a symmetric, ball shaped inclusion of a different type of agar with different material properties and hence, different Lamé parameters. The object is placed on a surface and a constant downward displacement is applied from the top while the outer boundary of the object is allowed to move freely. Due to a marker substance being injected into the object beforehand, the resulting displacement field can be measured inside using a combination of different imaging modalities. Since the object is rotationally symmetric, this also holds for the displacement field, which allows for a relatively high resolution 2D image.

Motivated by this, we consider the following setup for our numerical example problem: For the domain $\Omega$, we choose a rectangle in 2D, i.e., $N = 2$. We split the boundary $\partial\Omega$ of our domain into a part $\Gamma_D$ consisting of the top and the bottom edge of the rectangle and into a part $\Gamma_T$ consisting of the remaining two edges. Since the object is free to move on the sides, we set a zero traction condition on $\Gamma_T$, i.e., $g_T = 0$. Analogously for $\Gamma_D$, since the object is fixed to the surface and a constant displacement is being applied from above, we set $g_D = 0$ and $g_D = c_P = \text{const}$ on the parts of $\Gamma_D$ corresponding to the bottom and the top edge of the domain.

If, for simplicity, we set $\Omega = (0,1)^2$, then the underlying non-homogenized forward

problem (2.1) simplifies to

$$\begin{aligned} -\operatorname{div}(\sigma(\tilde{u}(x))) &= 0\,, \quad && x \in (0,1)^2\,, \\ \tilde{u}(x) &= 0\,, && x \in [0,1] \times \{0\}\,, \\ \tilde{u}(x) &= c_P\,, && x \in [0,1] \times \{1\}\,, \\ \sigma(\tilde{u}(x))\vec{n}(x) &= 0\,, && x \in \{0,1\} \times [0,1]\,. \end{aligned} \tag{4.4}$$

The homogenization function $\Phi$ can be chosen as $\Phi(x_1, x_2) := c_P\, x_2$ in this case.

In order to define the exact Lamé parameters $(\lambda^\dagger, \mu^\dagger)$, we first need to introduce the following family $\mathcal{B}^{h_1,h_2}_{r_1,r_2}$ of symmetric 2D bump functions with a circular plateau

$$\mathcal{B}^{h_1,h_2}_{r_1,r_2}(x,y) := \begin{cases} h_1\,, & \sqrt{x^2+y^2} \le r_1\,, \\ h_2\,, & \sqrt{x^2+y^2} \ge r_2\,, \\ \mathcal{S}^{h_1,h_2}_{r_1,r_2}(\sqrt{x^2+y^2})\,, & r_1 < \sqrt{x^2+y^2} < r_2\,, \end{cases}$$

where $\mathcal{S}^{h_1,h_2}_{r_1,r_2}$ is a 5th order polynomial chosen such that the resulting function $\mathcal{B}^{h_1,h_2}_{r_1,r_2}$ is twice continuously differentiable. The exact Lamé parameters $(\lambda^\dagger, \mu^\dagger)$ are then created by shifting the function $\mathcal{B}^{h_1,h_2}_{r_1,r_2}$ and using different values of $r_1, r_2, h_1, h_2$; see Figure 4.1.

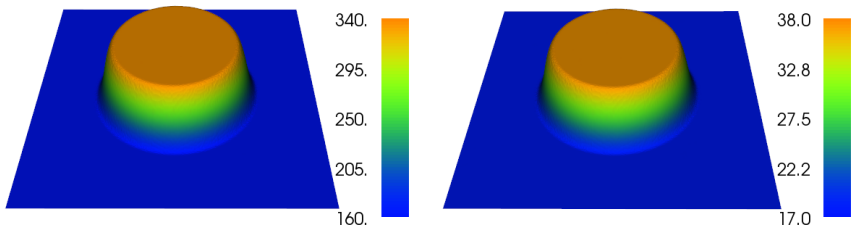


Figure 4.1: Exact Lamé parameters $(\lambda^\dagger, \mu^\dagger)$, in kPa.

As we have seen, a certain smoothness in the exact Lamé parameters is required for reconstruction with the operators $F|_{\mathcal{D}_s(F)}$ and $F_c$. Although this might be an unnatural assumption in some cases as different materials next to each other may have Lamé parameters of high contrast, it can be justified in the case of the combined agar sample, since when combining the different agar samples into one, the transition from one type of agar into the other can be assumed to be continuous, leading to a smooth behaviour of the Lamé parameters in the transition area.

However, since we also want to see the behaviour of the reconstruction algorithm in case of non-smooth Lamé parameters $(\lambda^\dagger, \mu^\dagger)$, we also look at $(\lambda^\dagger, \mu^\dagger)$ depicted in Figure 4.2, which were created using $\mathcal{B}^{h_1,h_2}_{r_1,r_2}$ with $r_1 \approx r_2$ and which, although being twice continuously differentiable in theory, behave like discontinuous functions after discretization.

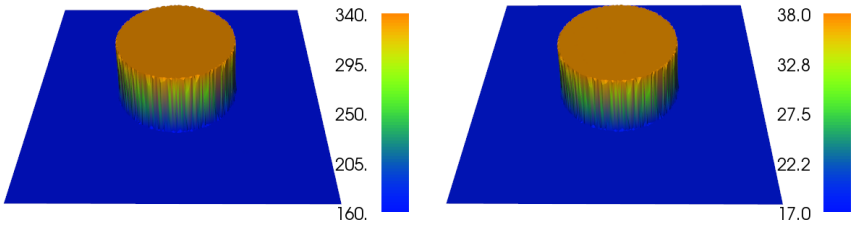


Figure 4.2: Exact Lamé parameters $(\lambda^\dagger, \mu^\dagger)$ created from $\mathcal{B}^{h_1,h_2}_{r_1,r_2}$ with $r_1 \approx r_2$, in kPa.

The discretization, implementation and computation of the involved variational problems was done using Python and the library FEniCS [3]. For the solution of the inverse problem a triangulation with 4691 vertices was introduced for discretizing the Lamé parameters. The data $u$ was created by applying the forward model (4.4) to $(\lambda^\dagger, \mu^\dagger)$ using a finer discretization with 28414 vertices in order to avoid an inverse crime. For the constant $c_P$ in (4.4) the choice $c_P = -10^{-4}$ is used. The resulting displacement field for the smooth Lamé parameters $(\lambda^\dagger, \mu^\dagger)$ is depicted in Figure 4.3. Afterwards, a random noise vector with a relative noise level of 0.5% is added to $u$ to arrive at the noisy data $u^\delta$.

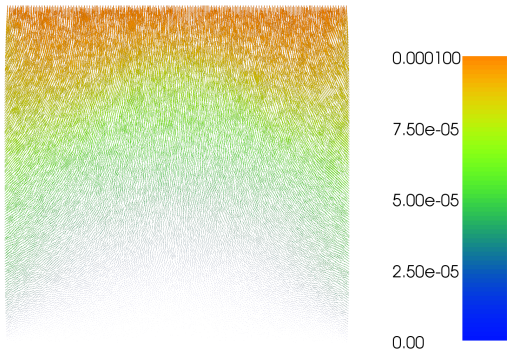


Figure 4.3: Displacement field $u$ corresponding to the Lamé parameters $(\lambda^\dagger, \mu^\dagger)$ depicted in Figure 4.1.

## 4.3 Numerical Results

In this section we present various reconstruction results for different combinations of operators, Lamé parameters and boundary conditions. Since the domain $\Omega$ is two-dimensional, i.e., $N = 2$, the operators $F|_{\mathcal{D}_s(F)}$ and $F_c$ are well-defined for any $s > 1$.

By our analysis above, we know that the nonlinearity condition holds for the operator $F_c$ if $s > N/2 + 1$ which suggests to use $s > 2$. However, since numerically there is hardly any difference between using $s = 2$ and $s = 2 + \varepsilon$ for $\varepsilon$ small enough, we choose $s = 2$ for ease of implementation in the following examples. When using the operator $F_c$ we chose a slightly smaller square than $\Omega$ for the domain $\Omega_1$, which is visible in the reconstructions. Unless noted otherwise, the accelerated Landweber type method (4.1) was used together with the steepest descent stepsize (4.3) and the iteration was terminated using the discrepancy principle (4.2) together with $\tau = 1$. Concerning the initial guess, when using the operator $F|_{\mathcal{D}_s(F)}$ the choice $(\lambda_0, \mu_0) = (2, 0.3)$ was made while when using the operator $F_c$ a zero initial guess was used.

**Example 4.1.** As a first test we look at the reconstruction of the smooth Lamé parameters (Figure 4.1), using the operator $F_c$. The iteration terminated after 642 iterations yields the reconstructions depicted in Figure 4.4. The parameter $\mu^\dagger$ is well reconstructed both qualitatively and quantitatively, with some obvious small artefacts around the border of the inner domain $\Omega_1$. The parameter $\lambda^\dagger$ is less well reconstructed, which is a common theme throughout this section and is due to the smaller sensitivity of the problem to changes of $\lambda$. Anyhow, the location and also some quantitative information of the inclusion is obtained.

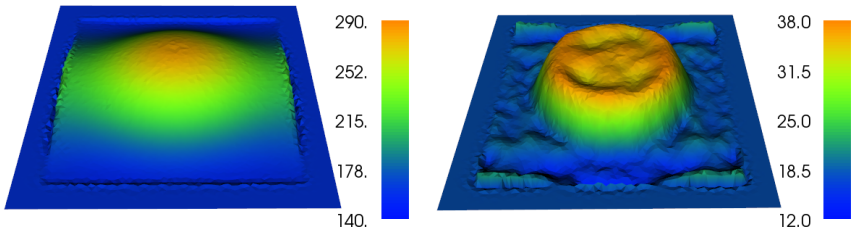


Figure 4.4: Reconstructions of $(\lambda^\dagger, \mu^\dagger)$, in kPa. Smooth Lamé parameters (Figure 4.1) - Displacement-Traction boundary conditions - operator $F_c$.

**Example 4.2.** Using the same setup as before, but this time with the operator $F|_{\mathcal{D}_s(F)}$ instead of $F_c$ leads to the reconstructions depicted in Figure 4.5, the discrepancy principle being satisfied after 422 iterations in this case. Even though some information about the Lamé parameters can be obtained also here, the reconstructions are in general worse than in the previous case. This is probably due to the fact that for mixed boundary conditions and the operator $F|_{\mathcal{D}_s(F)}$ the nonlinearity condition could not be shown and probably does not hold.

**Example 4.3.** Going back to the operator $F_c$ but now using the non-smooth Lamé parameters (Figure 4.2), we obtain the reconstructions depicted in Figure 4.6 after 635 iterations. We get roughly the same results as for the first test with the main difference

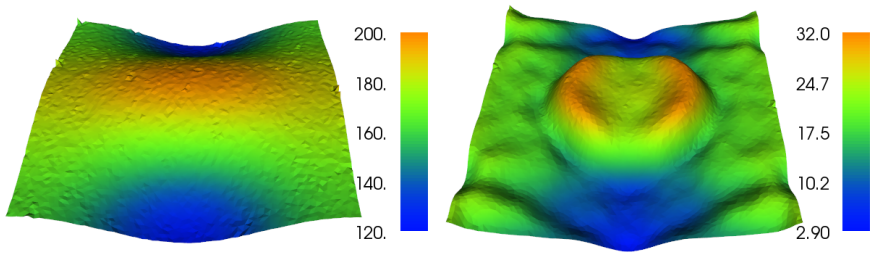


Figure 4.5: Reconstructions of $(\lambda^\dagger, \mu^\dagger)$, in kPa. Smooth Lamé parameters (Figure 4.1) - Displacement-Traction boundary conditions - operator $F|_{\mathcal{D}_s(F)}$.

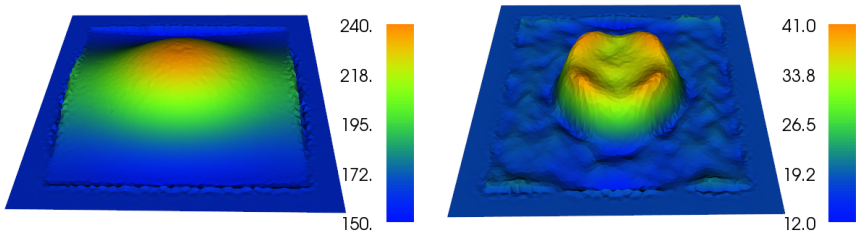


Figure 4.6: Reconstructions of $(\lambda^\dagger, \mu^\dagger)$, in kPa. Non-smooth Lamé parameters (Figure 4.2) - Displacement-Traction boundary conditions - operator $F_c$.

that the reconstructed values of the inclusion now fit a little less well than before, which is probably due to the non-smoothness of the used Lamé parameters.

**Example 4.4.** For the following tests, we want to see what happens if instead of mixed displacement-traction boundary conditions, only pure displacement conditions are used. For this, we replace the traction boundary condition in (4.4) by a zero displacement condition while leaving everything else the same. The resulting reconstructions using the operator $F_c$ for both smooth and non-smooth Lamé parameters are depicted in Figures 4.7 and 4.8. The discrepancy principle stopped after 177 and 194 iterations, respectively. Compared to the previous tests, it is immediately obvious that the parameter $\lambda^\dagger$ is now much better reconstructed than before in both cases. Also the parameter $\mu^\dagger$ is still nicely reconstructed although not as good as in the case of mixed boundary conditions. The influence of the non-smooth Lamé parameters in Figure 4.8 can perhaps best be seen in the volcano like appearance of the reconstruction of $\mu^\dagger$.

**Example 4.5.** Next, we take a look at the reconstruction of the smooth Lamé parameters using $F|_{\mathcal{D}_s(F)}$ and as before the pure displacement boundary conditions. Interestingly, Nesterov acceleration does not seem to work well in this case and so pure Landweber iteration with the steepest descent stepsize was used to obtain the recon-

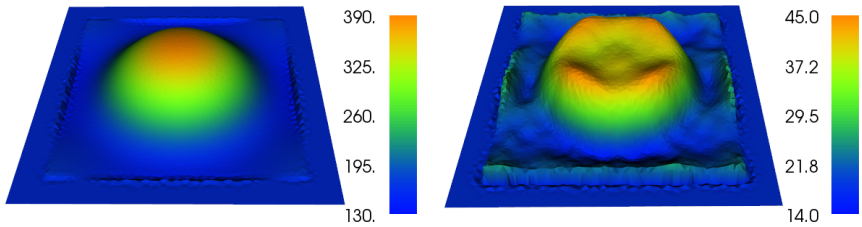


Figure 4.7: Reconstructions of $(\lambda^\dagger, \mu^\dagger)$, in kPa. Smooth Lamé parameters (Figure 4.1) - Pure displacement boundary conditions - operator $F_c$.

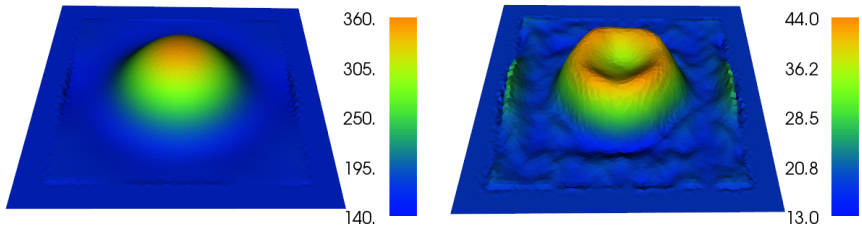


Figure 4.8: Reconstructions of $(\lambda^\dagger, \mu^\dagger)$, in kPa. Non-smooth Lamé parameters (Figure 4.2) - Pure displacement boundary conditions - operator $F_c$.

structions depicted in Figure 4.9, the discrepancy principle being satisfied after 937 iterations. As with the reconstructions obtained in case of mixed boundary conditions, this case is worse than when using $F_c$, for probably the same reasons mentioned above. Note however that in comparison with Figure 4.5, the inclusion in $\lambda^\dagger$ is much better resolved now than in the other case, which is potentially due to the use of pure displacement boundary conditions.

**Example 4.6.** For the last test we return to the same setting as in Example 4.1, i.e., we again use the operator $F_c$ and mixed displacement-traction boundary conditions. However, this time we consider different exact Lamé parameters modelling a material sample with three inclusions of varying elastic behaviour. The exact parameters and the resulting reconstructions, obtained after 921 iterations, are depicted in Figure 4.10. As expected, the Lamé parameter $\mu^\dagger$ is nicely reconstructed in shape, value and location of the inclusions. Moreover, even though the reconstruction of $\lambda^\dagger$ does not exhibit the same shape as the exact parameter, some information about the value and the location of the inclusions was obtained.

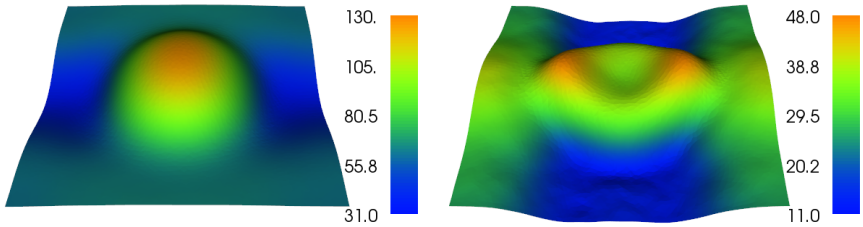


Figure 4.9: Reconstructions of $(\lambda^\dagger, \mu^\dagger)$, in kPa. Smooth Lamé parameters (Figure 4.1) - Pure displacement boundary conditions - operator $F|_{\mathcal{D}_s(F)}$.

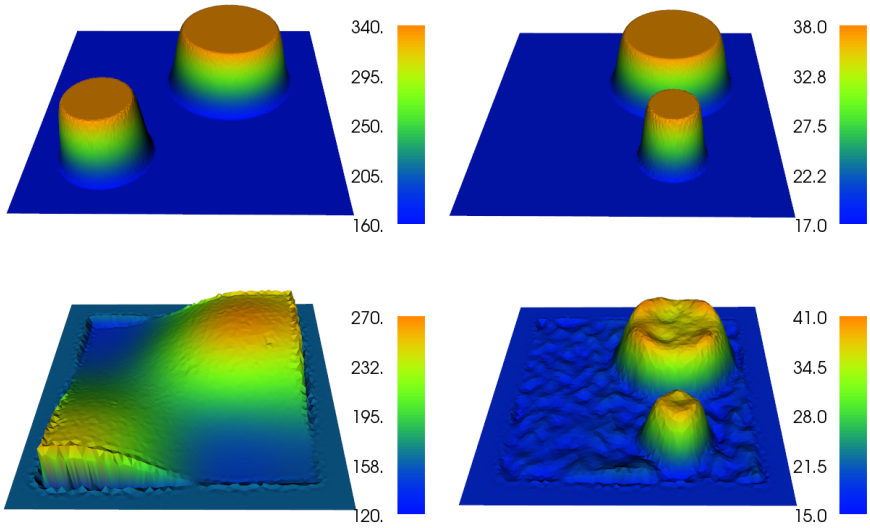


Figure 4.10: Exact Lamé parameters $(\lambda^\dagger, \mu^\dagger)$ (top) and their reconstructions (bottom), in kPa - Displacement-Traction boundary conditions - operator $F_c$.

# 5 Support and Acknowledgements

The first author was funded by the Austrian Science Fund (FWF): W1214-N15, project DK8. The second author was funded by the Danish Council for Independent Research - Natural Sciences: grant 4002-00123. The fourth author is also supported by the FWF-project "Interdisciplinary Coupled Physics Imaging" (FWF P26687). The authors would like to thank Dr. Stefan Kindermann and Dr. Stefan Takacs for reading early drafts of the manuscript and providing valuable suggestions and insights during discussions on the subject.

# Appendix 1. Important results from PDE theory

Here we collect important results in the theory of partial differential used throughout this paper. Two basic results are the trace inequality [1], which states that there exists a constant $c_T = c_T(\Omega) > 0$ such that

$$\|v\|_{H^{\frac{1}{2}}(\Gamma_T)} \leq c_T \|v\|_{H^1(\Omega)} , \quad \forall\, v \in V , \tag{5.1}$$

and Friedrich's inequality [17], i.e., there exists a constant $c_F = c_F(\Omega) > 0$ such that

$$\|v\|_{L^2(\Omega)} \leq c_F \|\nabla v\|_{L^2(\Omega)} , \quad \forall\, v \in V , \tag{5.2}$$

from which we can deduce

$$\|v\|^2_{H^1(\Omega)} \leq (1 + c_F^2) \|\nabla v\|^2_{L^2(\Omega)} , \quad \forall\, v \in V . \tag{5.3}$$

Korn's inequality [42] states that there exists a constant $c_K = c_K(\Omega) > 0$ such that

$$\int_\Omega \|\mathcal{E}(v)\|_F^2 \, dx \geq c_K^2 \|\nabla v\|^2_{L^2(\Omega)} , \qquad \forall\, v \in V . \tag{5.4}$$

Furthermore, we need the following regularity result

**Lemma 5.1.** *Let $(\lambda, \mu) \in \mathcal{D}_s(F)$ with $s > N/2 + 1$ and $w \in L^2(\Omega)^N$. Then there exists a unique weak solution $u$ of the elliptic boundary value problem*

$$\begin{aligned} -\operatorname{div}(\sigma(u)) &= w , \quad \text{in } \Omega , \\ u\,|_{\Gamma_D} &= 0 , \\ \sigma(u)\vec{n}\,|_{\Gamma_T} &= 0 , \end{aligned} \tag{5.5}$$

*and for every bounded, open, connected Lipschitz domain $\Omega_1 \subset \Omega$ with $\bar{\Omega}_1 \Subset \Omega$ there holds $u|_{\Omega_1} \in H^2(\Omega_1)^N$ and $-\operatorname{div}(\sigma(u)) = w$ pointwise almost everywhere in $\Omega_1$. Furthermore, there is a constant $c_R = c_R(\lambda, \mu, \Omega_1, \Omega)$ such that*

$$\|u\|_{H^2(\Omega_1)} \leq c_R \|w\|_{L^2(\Omega_1)} . \tag{5.6}$$

*Proof.* This follows immediately from [33, Theorem 4.16]. □

# Appendix 2. A Regularity Result

In the numerical examples considered above, the domain $\Omega \subset \mathbb{R}^2$ (i.e., $N = 2$) is a rectangle with both $g_D$ and $g_T$ consisting of the two opposite edges of the rectangle. We now see that for this domain $H^2(\Omega)$ regularity holds. For this we use the regularity results in [33], especially Theorem 4.16 and Theorem 4.18, which provide interior regularity and local regularity near the boundary for general elliptic systems with mixed boundary conditions.

**Proposition 5.2.** *Let $s > 2$, $(\lambda, \mu) \in \mathcal{D}_s(F)$ and $w \in L^2(\Omega)^2$. Furthermore, assume that*

$$\begin{aligned}\Omega &:= \{x = (x_1, x_2) \in \mathbb{R}^2 \,|\, (a_1 < x_1 < b_1) \wedge (a_2 < x_2 < b_2)\}\,,\\ \Gamma_T &:= \{x = (x_1, x_2) \in \mathbb{R}^2 \,|\, (x_1 = a_1) \vee (x_1 = b_1)\}\,,\\ \Gamma_D &:= \{x = (x_1, x_2) \in \mathbb{R}^2 \,|\, (x_2 = a_2) \vee (x_2 = b_2)\}\,,\end{aligned}$$

*for $a_1, a_2, b_1, b_2 \in \mathbb{R}$ with $a_1 < b_1$ and $a_2 < b_2$. Then $A^{-1}_{\lambda,\mu} T w \in V \cap H^2(\Omega)^2$ and there exists a constant $c_R = c_R(\lambda, \mu, \Omega) > 0$ such that*

$$\left\| A^{-1}_{\lambda,\mu} T w \right\|_{H^2(\Omega)} \leq c_R \left\| w \right\|_{L^2(\Omega)}\,.$$

*Additionally, there exists a constant $c_D = c_D(\Omega) > 0$ such that*

$$c_R(\lambda, \mu, \Omega) \leq c_D(\Omega) \left\| (\lambda, \mu) \right\|_{W^{1,\infty}(\Omega)}\,.$$

*Proof.* Let $s > 2$, $(\lambda, \mu) \in \mathcal{D}_s(F)$ and $w \in L^2(\Omega)^2$. For the purpose of this proof, we need to make some preliminary definitions. First of all, setting $c := (b_1 - a_1)$, we define

$$\begin{aligned}\Omega_1 &:= \{x = (x_1, x_2) \in \mathbb{R}^2 \,|\, (a_1 - c < x_1 < a_1) \wedge (a_2 < x_2 < b_2)\}\,,\\ \Omega_2 &:= \{x = (x_1, x_2) \in \mathbb{R}^2 \,|\, (b_1 < x_1 < b_1 + c) \wedge (a_2 < x_2 < b_2)\}\,,\\ \Omega' &:= \Omega \cup \Omega_1 \cup \Omega_2\,,\\ \Gamma'_T &:= \{x = (x_1, x_2) \in \mathbb{R}^2 \,|\, (x_1 = a_1 - c) \vee (x_1 = b_1 + c)\}\,,\\ \Gamma'_D &:= \{x = (x_1, x_2) \in \mathbb{R}^2 \,|\, (x_2 = a_2) \vee (x_2 = b_2)\}\,.\end{aligned}$$

Next, we mirror the functions $w$ to the domains $\Omega_1$ and $\Omega_2$, i.e., we set

$$\begin{aligned}w_1(x_1, x_2) &:= w(2a_1 - x_1, x_2)\,, \qquad \forall (x_1, x_2) \in \Omega_1\,,\\ w_2(x_1, x_2) &:= w(2b_1 - x_1, x_2)\,, \qquad \forall (x_1, x_2) \in \Omega_2\,,\\ w'(x_1, x_2) &:= \begin{cases} w(x_1, x_2)\,, & (x_1, x_2) \in \Omega\,,\\ w_1(x_1, x_2)\,, & (x_1, x_2) \in \Omega_1\,,\\ w_2(x_1, x_2)\,, & (x_1, x_2) \in \Omega_2\,. \end{cases}\end{aligned}$$

and we proceed analogously to define the functions $\lambda_1, \lambda_2, \lambda'$ and $\mu_1, \mu_2, \mu'$. In the following, whenever we are considering $a_{\lambda,\mu}, A_{\lambda,\mu}$, and $T$, we always implicitly assume that they are defined on Sobolev spaces corresponding to their arguments.

Next, we define the following functions:

$$u := A^{-1}_{\lambda,\mu} T w\,, \quad u_1 := A^{-1}_{\lambda_1,\mu_1} T w_1\,, \quad u_2 := A^{-1}_{\lambda_2,\mu_2} T w_2\,, \quad u' := A^{-1}_{\lambda',\mu'} T w'\,,$$

Since $w \in L^2(\Omega)^2$ and $(\lambda, \mu) \in \mathcal{D}_s(F)$, which in particular implies that $(\lambda', \mu') \in W^{1,\infty}(\Omega')$, the functions $u, u_1, u_2, u'$ are well-defined. Furthermore, after setting

$$\bar{u}(x_1, x_2) := \begin{cases} u(x_1, x_2)\,, & (x_1, x_2) \in \Omega\,,\\ u_1(x_1, x_2)\,, & (x_1, x_2) \in \Omega_1\,,\\ u_2(x_1, x_2)\,, & (x_1, x_2) \in \Omega_2\,, \end{cases}$$

it follows from

$$\begin{aligned} a_{\lambda',\mu'}(\bar{u},v) &= a_{\lambda',\mu'}(\bar{u},v) + a_{\lambda',\mu'}(\bar{u},v) + a_{\lambda',\mu'}(\bar{u},v) \\ &= a_{\lambda,\mu}(u,v) + a_{\lambda_1,\mu_1}(u_1,v) + a_{\lambda_2,\mu_2}(u_2,v) \\ &= \langle\, Tw, v\,\rangle + \langle\, Tw_1, v\,\rangle + \langle\, Tw_2, v\,\rangle = \langle\, Tw', v\,\rangle\ , \qquad \forall\, v \in H^1_{\Gamma'_D}(\Omega')\,, \end{aligned}$$

that $u' = \bar{u}$, which in particular implies that $u = \bar{u}|_\Omega = u'|_\Omega$.

Now, if we set $\varepsilon := \frac{1}{4}\min\{b_1 - a_1, b_2 - a_2\}$ and define the set

$$U := \Omega \backslash \left(\mathcal{B}_\varepsilon(a_1 - c, a_2) \cup \mathcal{B}_\varepsilon(a_1 - c, b_2) \cup \mathcal{B}_\varepsilon(b_1 + c, a_2) \cup \mathcal{B}_\varepsilon(b_1 + c, b_2)\right)\ ,$$

it follows from [33, Theorem 4.16 and Theorem 4.18] that $u'|_U \in H^2(U)^2$ and that there exists a constant $c_R = c_R(\lambda, \mu, \Omega) > 0$ such that

$$\|u'\|_{H^2(U)} \leq c_R \|w\|_{L^2(\Omega)}\ .$$

Hence, it follows that $u \in H^2(\Omega)$ and that there holds

$$\|u\|_{H^2(\Omega)} \leq c_R \|w\|_{L^2(\Omega)}\ .$$

Furthermore, it can be seen from the proofs of [33, Theorem 4.16 and Theorem 4.18] that there is another constant $c_D = c_D(\Omega)$ such that

$$c_R(\lambda, \mu, \Omega) \leq c_D(\Omega)\, \|(\lambda, \mu)\|_{W^{1,\infty}(\Omega)}\ .$$

Since $u \in H^2(\Omega)^2$, it follows that

$$\operatorname{div}\left(\lambda \operatorname{div}(u)\, I + 2\mu\, \mathcal{E}(u)\right) = w\,,$$

almost everywhere in $\Omega$. Since we already know that $u|_{\Gamma_D} = 0$ it remains to be shown that

$$\left(\bar{\lambda} \operatorname{div}(u)\, I + \bar{\mu}\, \mathcal{E}(u)\right) \vec{n}\,|_{\Gamma'_T} = 0\,. \tag{5.7}$$

Now since for all $v \in V$ by partial integration there holds

$$\begin{aligned} &\langle\, Tw, v\,\rangle_{V^*,V} = a_{\lambda,\mu}(u,v) \\ &\quad = \int_\Omega \operatorname{div}\left(\lambda \operatorname{div}(u)\, I + 2\mu\, \mathcal{E}(u)\right) v\, dx + \int_{\partial\Omega} \left(\bar{\lambda} \operatorname{div}(u)\, I + \bar{\mu}\, \mathcal{E}(u)\right) \vec{n} \cdot v\, dS \\ &\quad = \int_\Omega wv\, dx + \int_{\Gamma_T} \left(\bar{\lambda} \operatorname{div}(u)\, I + \bar{\mu}\, \mathcal{E}(u)\right) \vec{n} \cdot v\, dS \\ &\quad = \langle\, Tw, v\,\rangle_{V^*,V} + \int_{\Gamma_T} \left(\bar{\lambda} \operatorname{div}(u)\, I + \bar{\mu}\, \mathcal{E}(u)\right) \vec{n} \cdot v\, dS\,, \end{aligned}$$

it follows that (5.7) holds, which concludes the proof. □

*Remark.* Similarly as in Proposition 5.2, one could also show $H^2(\Omega)$ regularity using a mirroring argument in case that the domain $\Omega$ is rectangular with $\Gamma_T$ consisting only of one side of the rectangle and $\Gamma_D$ consisting of the remaining three sides.

# References


[1] R. A. Adams and J. J. F. Fournier. *Sobolev Spaces*. Pure and Applied Mathematics. Elsevier Science, 2003.

[2] S. Agmon, A. Douglis, and L. Nirenberg. Estimates near the boundary for solutions of elliptic partial differential equations satisfying general boundary conditions I. *Communications on Pure and Applied Mathematics*, 12(4):623–727, 1959.

[3] M. S. Alnæs, J. Blechta, J. Hake, A. Johansson, B. Kehlet, A. Logg, C. Richardson, J. Ring, M. E. Rognes, and G. N. Wells. The FEniCS Project Version 1.5. *Archive of Numerical Software*, 3(100), 2015.

[4] A. B. Bakushinskii. The problem of the convergence of the iteratively regularized Gauß–Newton method. *Computational Mathematics and Mathematical Physics*, 32:1353–1359, 1992.

[5] A. B. Bakushinsky and M. Y. Kokurin. *Iterative Methods for Approximate Solution of Inverse Problems*, volume 577 of *Mathematics and Its Applications*. Springer, Dordrecht, 2004.

[6] G. Bal, C. Bellis, S. Imperiale, and F. Monard. Reconstruction of constitutive parameters in isotropic linear elasticity from noisy full–field measurements. *Inverse Problems*, 30(12):125004, 2014.

[7] G. Bal, W. Naetar, O. Scherzer, and J. Schotland. The Levenberg-Marquardt iteration for numerical inversion of the power density operator. *J. Inv. Ill-Posed Problems*, 21(2):265–280, 2013.

[8] G. Bal and G. Uhlmann. Reconstructions for some coupled-physics inverse problems. *Applied Mathematics Letters*, 25(7):1030–1033, 2012.

[9] G. Bal and G. Uhlmann. Reconstruction of coefficients in scalar second-order elliptic equations from knowledge of their solutions. *Communications on Pure and Applied Mathematic*, 66(10):1629–1652, 2013.

[10] P. E. Barbone and N. H. Gokhale. Elastic modulus imaging: on the uniqueness and nonuniqueness of the elastography inverse problem in two dimensions. *Inverse Problems*, 20(1):283–296, 2004.

[11] P. E. Barbone and A. A. Oberai. Elastic modulus imaging: some exact solutions of the compressible elastography inverse problem. *Physics in Medicine and Biology*, 52(6):1577–1593, 2007.

[12] A. Beck and M. Teboulle. A Fast Iterative Shrinkage-Thresholding Algorithm for Linear Inverse Problems. *SIAM J. Imaging Sci.*, 2(1):183–202, 2009.

[13] P. G. Ciarlet. *Mathematical Elasticity: Three-dimensional elasticity*. Number 1 in Mathematical Elasticity. North-Holland, 1994.

[14] M. M. Doyley. Model-based elastography: a survey of approaches to the inverse elasticity problem. *Physics in Medicine and Biology*, 57(3):R35–R73, 2012.

[15] M. M. Doyley, P. M. Meaney, and J. C. Bamber. Evaluation of an iterative reconstruction method for quantitative elastography. *Physics in Medicine and Biology*, 45(6):1521–1540, 2000.

[16] H. W. Engl, M. Hanke, and A. Neubauer. *Regularization of inverse problems*. Dordrecht: Kluwer Academic Publishers, 1996.

[17] L. C. Evans. *Partial Differential Equations*. Graduate studies in mathematics. American Mathematical Society, 1998.

[18] J. Fehrenbach, M. Masmoudi, R. Souchon, and P. Trompette. Detection of small inclusions by elastography. *Inverse Problems*, 22(3):1055–1069, 2006.

[19] D. Gilbarg and N. S. Trudinger. *Elliptic partial differential equations of second order*. Grundlehren der mathematischen Wissenschaften. Springer, 1998.

[20] N. H. Gokhale, P. E. Barbone, and A. A. Oberai. Solution of the nonlinear elasticity imaging inverse problem: the compressible case. *Inverse Problems*, 24(4):045010, 2008.

[21] M. Hanke, A. Neubauer, and O. Scherzer. A convergence analysis of the Landweber iteration for nonlinear ill-posed problems. *Numerische Mathematik*, 72(1):21–37, 1995.

[22] C. H. Huang and W. Y. Shih. A boundary element based solution of an inverse elasticity problem by conjugate gradient and regularization method. *Inverse Problems in Engineering*, 4(4):295–321, 1997.

[23] S. Hubmer, A. Neubauer, R. Ramlau, and H. U. Voss. On the parameter estimation problem of Magnetic Resonance Advection Imaging. *Inverse Problems and Imaging*, 2017. Accepted.

[24] S. Hubmer and R. Ramlau. Convergence analysis of a two-point gradient method for nonlinear ill-posed problems. *Inverse Problems*, 33(9):095004, 2017.

[25] B. Jadamba, A. A. Khan, and F. Raciti. On the inverse problem of identifying Lame coefficients in linear elasticity. *Computers and Mathematics With Applications*, 56(2):431–443, 2008.

[26] L. Ji, J. R. McLaughlin, D. Renzi, and J. R. Yoon. Interior elastodynamics inverse problems: shear wave speed reconstruction in transient elastography. *Inverse Problems*, 19(6):S1–S29, 2003.

[27] Q. Jin. Landweber-Kaczmarz method in Banach spaces with inexact inner solvers. *Inverse Problems*, 32(10):104005, 2016.

[28] B. Kaltenbacher, A. Neubauer, and O. Scherzer. *Iterative regularization methods for nonlinear ill-posed problems.* Berlin: de Gruyter, 2008.

[29] B. Kaltenbacher, F. Schöpfer, and T. Schuster. Iterative methods for nonlinear ill-posed problems in Banach spaces: convergence and applications to parameter identification problems. *Inverse Problems*, 25(6):065003 (19pp), 2009.

[30] A. Kirsch and A. Rieder. Inverse problems for abstract evolution equations with applications in electrodynamics and elasticity. *Inverse Problems*, 32(8):085001, 2016.

[31] A. Lechleiter and J. W. Schlasche. Identifying Lame parameters from time-dependent elastic wave measurements. *Inverse Problems in Science and Engineering*, 25(1):2–26, 2017.

[32] J. R. McLaughlin and D. Renzi. Shear wave speed recovery in transient elastography and supersonic imaging using propagating fronts. *Inverse Problems*, 22(2):681–706, 2006.

[33] W. C. H. McLean. *Strongly Elliptic Systems and Boundary Integral Equations.* Cambridge University Press, 2000.

[34] J. Necas. *Direct Methods in the Theory of Elliptic Equations.* Springer Monographs in Mathematics. Springer Berlin Heidelberg, 2011.

[35] Y. Nesterov. A method of solving a convex programming problem with convergence rate $O(1/k^2)$. *Soviet Mathematics Doklady*, 27(2):372–376, 1983.

[36] A. Neubauer. On Nesterov acceleration for Landweber iteration of linear ill-posed problems. *J. Inv. Ill-Posed Problems*, 25(3):381–390, 2017.

[37] A. A. Oberai, N. H. Gokhale, M. M. Doyley, and J. C. Bamber. Evaluation of the adjoint equation based algorithm for elasticity imaging. *Physics in Medicine and Biology*, 49(13):2955–2974, 2004.

[38] A. A. Oberai, N. H. Gokhale, and G. R. Feijoo. Solution of inverse problems in elasticity imaging using the adjoint method. *Inverse Problems*, 19(2):297–313, 2003.

[39] O. Scherzer. A convergence analysis of a method of steepest descent and a two-step algorithm for nonlinear ill-posed problems. *Numerical Functional Analysis and Optimization*, 17(1-2):197–214, 1996.

[40] F. Schöpfer, A. K. Louis, and T. Schuster. Nonlinear iterative methods for linear ill-posed problems in Banach spaces. *Inverse Problems*, 22(1):311–329, 2006.

[41] T. Schuster, B. Kaltenbacher, B. Hofmann, and K. S. Kazimierski. *Regularization Methods in Banach Spaces*. Radon series on computational and applied mathematics. De Gruyter, 2012.

[42] T. Valent. *Boundary Value Problems of Finite Elasticity: Local Theorems on Existence, Uniqueness, and Analytic Dependence on Data*. Springer Tracts in Natural Philosophy. Springer New York, 2013.

[43] T. Widlak and O. Scherzer. Stability in the linearized problem of quantitative elastography. *Inverse Problems*, 31(3):035005, 2015.